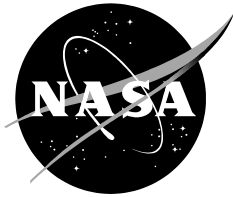


NASA/TP–20205011353



# Mars Rodwell Experiment Final Report

*Stephen J. Hoffman, Ph.D.*  
*The Aerospace Corporation, Houston, TX*  
*Johnson Space Center, Houston, Texas*

*James H. Lever, Ph.D.*  
*U.S. Army Corps of Engineers Cold Regions Research and Engineering Laboratory,*  
*Hanover, New Hampshire*

*Alida D. Andrews*  
*The Aerospace Corporation, Houston, TX*  
*Johnson Space Center, Houston, Texas*

*Kevin D. Watts*  
*Johnson Space Center, Houston, Texas*

National Aeronautics and  
Space Administration

*Johnson Space Center*  
*Houston, TX 77058*

---

**October 2020**

## NASA STI Program Report Series

The NASA STI Program collects, organizes, provides for archiving, and disseminates NASA's STI. The NASA STI program provides access to the NTRS Registered and its public interface, the NASA Technical Reports Server, thus providing one of the largest collections of aeronautical and space science STI in the world. Results are published in both non-NASA channels and by NASA in the NASA STI Report Series, which includes the following report types:

- **TECHNICAL PUBLICATION.** Reports of completed research or a major significant phase of research that present the results of NASA Programs and include extensive data or theoretical analysis. Includes compilations of significant scientific and technical data and information deemed to be of continuing reference value. NASA counterpart of peer-reviewed formal professional papers but has less stringent limitations on manuscript length and extent of graphic presentations.
- **TECHNICAL MEMORANDUM.** Scientific and technical findings that are preliminary or of specialized interest, e.g., quick release reports, working papers, and bibliographies that contain minimal annotation. Does not contain extensive analysis.
- **CONTRACTOR REPORT.** Scientific and technical findings by NASA-sponsored contractors and grantees.
- **CONFERENCE PUBLICATION.** Collected papers from scientific and technical conferences, symposia, seminars, or other meetings sponsored or co-sponsored by NASA.
- **SPECIAL PUBLICATION.** Scientific, technical, or historical information from NASA programs, projects, and missions, often concerned with subjects having substantial public interest.
- **TECHNICAL TRANSLATION.** English-language translations of foreign scientific and technical material pertinent to NASA's mission.

Specialized services also include organizing and publishing research results, distributing specialized research announcements and feeds, providing information desk and personal search support, and enabling data exchange services.

For more information about the NASA STI program, see the following:

- Access the NASA STI program home page at <http://www.sti.nasa.gov>
- Help desk contact information:

<https://www.sti.nasa.gov/sti-contact-form/>

and select the "General" help request type.

## Acknowledgments

The authors would like to acknowledge several people who made important contributions to the completion of this experiment and the research behind it.

**Maria Garcia-Robles** – an intern at the time of this work and now working as a contractor at the Johnson Space Center – who designed and had 3-D printed the custom parts we needed for the experiment apparatus.

**German Noria** – the NASA Johnson Space Center Energy Systems Test area (ESTA) technician who helped assemble our test equipment and then sat through the hours of testing to gather data we needed. German also helped fine tune the procedures and some of the equipment based on what he was seeing during early tests.

**Robert Fulmer** and **David Fanelli** – two more ESTA techs that helped select the right test equipment and sensors for our test (Fulmer) and wrote the software to control parts of the test equipment as well as gathering the data (Fanelli) – and **Mike Reddington**, for helping get all of the ESTA resources we needed to complete this experiment

**Lisa Erickson** – the thermal engineer who ran the early thermal modeling to help us understand how to make the bell jar test chamber do what we needed to do. Lisa also helped us get thermal blankets made for the bell jar based on the results from her modeling work.

**Kent Joosten** who estimated the water usage for the “water rich” scenario that became a benchmark for all our analysis.

**Doug Archer** and **Paul Niles** who helped with the early stages of the experiment design and then reviewed our work along the way to make sure it was sound.

\*\*\*\*



## TABLE OF CONTENTS

PARAGRAPH	PAGE
1.0 INTRODUCTION.....	2
1.1 BACKGROUND AND MOTIVATION.....	2
1.2 REPORT OUTLINE.....	3
2.0 HUMAN MARS MISSION PLANNING .....	4
2.1 GENERAL APPROACH.....	4
2.2 WATER USAGE ESTIMATES .....	4
3.0 MARS WATER RESOURCES .....	9
3.1 GENERAL WATER SOURCES ON MARS .....	9
3.2 NO LIQUID WATER AQUIFERS .....	9
3.3 TERRAIN FEATURES INDICATING BURIED ICE .....	11
4.0 RODRIGUEZ WELL HISTORY .....	16
4.1 EARLY USAGE.....	16
4.2 CURRENT USAGE .....	23
4.3 APPLICABILITY TO MARS.....	25
5.0 CRREL COMPUTER SIMULATION.....	28
5.1 CHANGES NEEDED FOR MARS APPLICATIONS .....	29
6.0 BELL JAR EXPERIMENT .....	31
6.1 EXPERIMENT DESIGN/DESCRIPTION.....	31
6.2 EQUIPMENT DESIGN/DESCRIPTION .....	36
6.3 PROCEDURE .....	41
7.0 EXPERIMENT RESULTS .....	43
7.1 DATA REDUCTION PROCESS.....	43
7.2 COMPARISON WITH OTHER EXPERIMENTAL RESULTS.....	46
8.0 SUMMARY AND RECOMMENDATIONS.....	51
9.0 REFERENCES.....	54
<b>APPENDICES</b>	
APPENDIX A DETAILS OF WATER USAGE ESTIMATES.....	58
APPENDIX B EXPERIMENT EQUIPMENT DETAILS.....	65
APPENDIX C FORTRAN CODE WITH COMMENTS AND DEFINITIONS/EXPLANATIONS OF TERMS .....	83

APPENDIX D RAW OR PROCESSED DATA FROM BELL JAR EXPERIMENTS .....	101
--	-----

## TABLES

Table 2.1. Surface Excursion Characteristics .....	7
Table 2.2. Products and Required Feedstock (per Mission).....	8
Table 2.3. Commodity Extraction and Production Martian Water Rates.....	8
Table 4.1. Rodwell Key Characteristics .....	27
Table 6.1. Target operating conditions and Rayleigh numbers for the model tests .....	35
Table 7.1. Test Data Summary .....	44
Table 7.2. Parameters $C$ and $n$ for correlation $Sh = C Ra^n$ .....	48
Table 7.3. Model-based predictions for water-cavity heat-transfer coefficients, $h_{w-a}$ , for Mars Rodwells based on pool diameter, $W$ . .....	50
Table A-1. Life Support Water Supply Requirement (4 Crew for 500 Days).....	60
Table A-2. Surface Excursion Characteristics .....	63
Table A-3. Products and Required Feedstock (per Mission) .....	63
Table A-4. Commodity Production and Martian Water Extraction Rates .....	64

## FIGURES

Figure 2.1. Mars Ascent Vehicle Conceptual Design.....	6
Figure 3.1. Athabasca Valles, Images Courtesy NASA/JPL/Malin Space Science Systems.....	10
Figure 3.2. Recurring Slope Lineae [16]. Image credit NASA/JPL/University of Arizona.....	10
Figure 3.3. Ice Excavated by Phoenix Lander, Image NASA/JPL/University of Arizona, Texas A&M University .....	11
Figure 3.4. LDA, LVF and CCF Martian Glaciation Features (MRO Context Camera).....	12
Figure 3.5. Global Distribution of LDA, LVF and CCF Features [26] .....	12
Figure 3.6. Impact Crater Ice Excavation and Sublimation [22] .....	13
Figure 3.7. Examples of recently discovery exposed ice scarps on Mars [4].....	13
Figure 3.8. Visual comparison for scale of exposed ice scarps on Mars with systems likely to be used for these Mars missions [4] .....	14
Figure 3.9. Location of ice scarps identified by Dundas et al [4].....	15
Figure 3.10. Hypothesized profile through Mars ice scarps identified by Dundas et al. [4].....	15
Figure 4.1 Location of Greenland Ice-Cap Stations near Thule Air Base [30] .....	17
Figure 4.2 Schematic sketch of water well and equipment [30]......	17
Figure 4.3. Second Rodriguez Well at Camp Century after two years of operation [9].....	20
Figure 4.4. Plan of Camp Tuto Ice Tunnel and Constructed Facilities [31].....	21
Figure 4.5. Camp Tuto water well development during 15 week test period. The majority of the water from this well was produced between 17 April and 7 June 1962. ....	22

Figure 4.6. Experimental Rodriguez Well evolution at the Amundsen-Scott South Pole Station [9].	23
Figure 4.7. The IceCube Neutrino Observatory configuration, located at the South Pole.	25
Figure 5.1. Schematic of Rodwell showing heat flows to the environment	28
Figure 6.1. Rodwell prototype (left) and small-scale model (right) showing key parameters and conceptual test layout (sketches not to scale)	32
Figure 6.2. Dimensionless mass-transport, $Sh$ , versus dimensionless flow parameters, $Ra$ , for evaporative mass loss from a water pool driven by natural convection above the pool. Predicted $Sh(Ra)$ values for Mars and our small-scale tests use the Bower and Saylor correlation (Equation 6.19), with the slight separation resulting from different values of $Sc$ .	36
Figure 6.3. Bell jar test facility at the NASA Johnson Space Center.	37
Figure 6.4. Test equipment used inside the bell jar to gather heat transfer data relevant to Rodwell operations.	38
Figure 6.5. Test equipment used inside the bell jar as seen from the internal camera.	39
Figure 6.6. View of test equipment inside bell jar during at test conditions (6 mbar pressure, -40°C temperature. This view shows the ice shelf that formed just above the water pool.	40
Figure 6.7. An expanded view of experiment equipment as assembled in the test volume.	41
Figure 7.1. Full-test data from Test 5 (upper) and Test 11 (lower): Atmospheric pressure (Pa), load cell mass (M), load cell temperature (T <sub>LC</sub> ), atmospheric temperature (T <sub>a</sub> ), and water temperature (T <sub>w</sub> ). The steady state periods were 25000 – 37000 s for Test 5 and 30000 – 35000 s for Test 11.	45
Figure 7.2. Sherwood-Rayleigh correlation, $Sh(Ra)$ , for test data and selected published correlations. Test 5 has little influence on the best-fit line through the large-dewar tests. The dashed lines show extensions of correlations from Bower & Saylor, Ingersoll, and Hecht below their stated ranges of $Ra$ validity to overlap with our data [43, 42, 10]	47
Figure 7.3. Nusselt number correlation with Rayleigh number for convective, $Nu_c$ , and total, $Nu_t$ , heat transfer. Unlike Holman's correlations for horizontal circular plates, the model-test $Nu$ values are nearly independent of $Ra$ .	49
Figure A-1. Assumed Resource Production Process	58
Figure A-2. Mars Ascent Vehicle Conceptual Design	59
Figure A-3. GCR Water Shielding Effectiveness	62
Figure A-4. Methane Oxygen Fuel Cell Chemistry	62
Figure B.1. Foil Heat Flux Sensor	65
Figure B-2. Load Cell	66
Figure B.3. Stir Bar	67
Figure B.4. Insulated Dewar (3-inch I.D.)	68
Figure B.5. Insulated Dewar (6-inch I.D.)	69
Figure B.6. Magnetic Induction Stirrer	70
Figure B.7 Submersible Thermistor	71

Figure B.8. Air Circulation Fan .....	72
Figure B.9. Portable Bell Jar System 996 .....	73
Figure B.10. Temperature Control Shroud.....	74
Figure B.11. Laboratory Support Stand .....	75
Figure B.12. Support Stand Steel Rods .....	76
Figure B.13. Lab Clamp Holders.....	77
Figure B.14. 3D Printed “Bowl” .....	78
Figure B.15. 3D Printed “Support Ring” .....	79
Figure B.16. 3D Printed “Base” .....	80
Figure B.17. Resistance Temperature Detectors (RTDs) .....	81
Figure B.18. Recirculating Chiller .....	82
Figure D.1. Test 5 – 9/30/2019 .....	101
Figure D.2. Test 7 – 10/16/2019 .....	102
Figure D.3. Test 8 – 10/23/2019 .....	103
Figure D.4. Test 9 – 9/30/2019 .....	104
Figure D.5. Test 10 – 10/07/2019 .....	105
Figure D.6. Test 11 – 10/16/2019 .....	106
Figure D.7. Test 12 – 10/24/2019 .....	107



# **Mars Rodwell Experiment Final Report**

## **EXECUTIVE SUMMARY**

Developed by Army engineer Raul Rodriguez at Camp Century in Greenland during the early 1960s, a Rodriguez Well uses heat exchangers and a submersible pump to create a cavity deep under a glacier's surface and cycle the heated water up an ice shaft, siphoning a portion of the flow for consumption before sending the rest back down to the well. To evaluate the performance of a Rodriguez Well as one of multiple approaches for extracting water from massive ice deposits on Mars, a series of tests were performed at the Johnson Space Center (JSC) Energy Systems Test Area (ESTA) Facility under Martian equivalent environmental factors such as atmospheric and water surface pressure and density. These values were then used to create an energy balance model for a Martian Rodriguez Well, replacing the terrestrial environmental factors with the found Martian equivalents in a computer model published by the Cold Regions Research and Engineering Laboratory (CRREL). This report documents the test results and the subsequent findings from running the modified code.

## 1.0 INTRODUCTION

This report describes the results of an experiment designed to provide data with which to improve computer analysis tools used to predict the performance of a Rodriguez Well on the surface of Mars. The Rodriguez Well was developed by Raul Rodriguez and others from the U.S. Army Corps of Engineers (USACE) Cold Regions Research and Engineering Laboratory (CRREL) in the early 1960s to supply potable water to soldiers stationed on the Greenland Ice Sheet. Massive deposits of ice have also been found on Mars, making the relatively simple technique of the Rodriguez Well an attractive option for supporting future human missions on that planet if it can be shown to be effective under Mars environmental conditions. Computer analysis tools developed by CRREL, properly modified, are an integral part of assessing the technology required (e.g. mass, power, and operational complexity) to determine the effectiveness of this approach.

### 1.1 BACKGROUND AND MOTIVATION

For many years, NASA has investigated alternative human Mars missions, examining different mission objectives, trajectories, vehicles, and technologies. At the highest levels, decisions regarding the timing of and objectives for a human mission to Mars continue to evolve, while at more specialized levels, relevant technologies and discoveries about Mars continue to advance. All of these factors – high-level goals and objectives, technological advancements, and discoveries about the nature of Mars – can have impacts, ranging from benign to profound, on the implementation details of human Mars missions.

To assist those charged with deciding overall objectives, timing, and technologies for eventual human Mars missions in understanding the implications of all of these factors, an on-going series of reference missions or architecture options have been built. In addition, more narrowly focused assessments of technologies and discoveries have been carried out to provide meaningful insights.

One area of continuing interest among these decision-makers is the innovative leveraging of technological advances that take advantage of accessible Martian in-situ resources to make human missions more affordable and sustainable. One of the most useful among these Martian resources is water.

Data returned by recent Mars robotic missions have provided a strong basis for scientists to assert that large quantities of liquid water flowed on the surface of Mars for a substantial period of time [1]. If this water were still available, it would substantially change the approach to human missions on the surface. However, Mars' geologic record clearly shows that the planet lost its surface water a very long time ago, and there is certainly none present today. There are, however, large amounts of water ice currently located in the polar regions and many presume that water is present in the deep subsurface. Both of these reservoirs of water are, for all practical purposes, inaccessible for use by human crews. But there is growing evidence that Mars may be more "water rich" than previously suspected, based on data indicating that substantial quantities of water are mixed with surface regolith, bound in minerals located at or near the surface, and buried in large glacier-like forms [2, 3, 4]. All of these potential sources of water are in areas and in forms that are likely accessible by human crews.

Recent studies, carried out as part of NASA's ongoing examination of human Mars missions, considered the impacts of an abundant supply of in-situ, accessible water on these mission scenarios [2, 5, 6, 7, 8]. For these assessments, the elements of a human Mars mission that would most benefit from the largely unconstrained availability of water were identified and quantities of water likely to be used by crews in this "water rich" scenario were estimated.

Sources of feedstock material from which water could be extracted were then identified based on the most recent available data for the surface of Mars. These feedstock materials tended to fall into two broad categories: regolith/minerals and ices. Assessments have been carried out for each of these feedstock types. Examples of assessments that use regolith/minerals as a feedstock can be found in the report by Abbud-Madrid, et al. [5] and the paper by Kleinhenz and Paz [6]. The papers by Hoffman, et al. [7, 8] provide a similar assessment of accessing and withdrawing water from subsurface ice deposits, using a combination of vertical drilling and a well-established terrestrial technique known as a Rodriguez Well [9]. Both approaches were found to be technically feasible. However, the scope and scale of the infrastructure needed to produce useful quantities of water in either approach was heavily dependent on assumptions regarding feedstock material characteristics and performance of the systems used to extract the water.

One recognized shortcoming of the Hoffman et al. assessment was the use of analysis tools – in particular, an engineering analysis tool designed to evaluate the performance of a Rodriguez Well under terrestrial environmental conditions [9] – that were not properly configured to simulate the Martian environment. Although the analysis tools and approach used by Hoffman et al. were appropriate for this preliminary assessment, several empirical parameters necessary to properly characterize the Martian environment simply did not exist. The need to overcome this shortcoming and provide a more accurate assessment of accessing and using Martian water ice led to an experiment to determine the needed empirical parameters. Values for these empirical parameters were derived from experiments conducted under conditions similar to the Martian environment [10]. They were then incorporated into the analysis tool and the results reported [8]. This report documents the design, development, and results of the experiment from which these parameters were determined.

## **1.2 REPORT OUTLINE**

The remainder of this report documents details describing this experiment as well as the data generated and the resulting empirical parameters sought. The next section will describe the features of a human Mars mission, as envisioned at the time of this experiment, and the uses of water to support such a mission. The third section describes where water ice resources are currently thought to exist and the form these feedstock materials are thought to take. The fourth section reviews the history of the Rodriguez Well and its various uses here on Earth. Section 5 describes the computer simulation tool developed by the U.S. Army Corps of Engineers' (USACE) Cold Regions Research and Engineering Laboratory (CRREL) that was adapted to assess the utility of a Rodriguez Well on Mars. This section also identifies those empirical parameters that must be determined to properly reflect Martian environmental conditions. The sixth section describes the theoretical approach used to design the experiment conducted to gather data from which the needed empirical parameters can be derived. This theoretical basis is then used to describe the experimental hardware itself and the procedure used to gather the necessary data. The seventh section will describe the data reduction process and resulting empirical parameters. The empirical parameters developed from this experiment will be compared with results from other similar and relevant experiments. The final section will summarize this report and will make recommendations for further work in this area.

**2.0 HUMAN MARS MISSION PLANNING** Planning for future human missions to Mars and the likely water needs of those crews sets the performance requirements for a Rodwell system. This section describes how human mission planning leads to the water quantity and production rates that a Rodwell simulation tool would be used to analyze.

## **2.1 GENERAL APPROACH**

Over the past several years, NASA study managers established several ground-rules and assumptions to provide some level of consistency across the many studies and assessments associated with potential human Mars missions. Principal among these ground-rules and assumptions relevant to this report was a decision to concentrate all surface assets needed to support human exploration of Mars at a single location and then send future crews to this site for subsequent missions. This contrasts with the scenario considered in the 2009 Design Reference Architecture 5.0 (DRA 5.0) in which a campaign of three missions sends crews to different locations on Mars [11].

One outcome of the choice to concentrate all surface assets at a single location is the concept of an Exploration Zone (EZ) that describes the features of a surface location where the activities of the human crews will take place [12]. An EZ is a collection of Regions of Interest (ROIs) that are located within approximately 100 kilometers of a centralized landing site. ROIs are areas that are relevant for scientific investigation and/or development/maturation of capabilities and resources necessary for a sustainable human presence – such as water sources. The EZ also contains multiple landing sites as well as a habitation area that will be used by multiple human crews during missions to explore and utilize the ROIs within the EZ. As NASA identifies candidate locations that exhibit the potential to be viable EZs, existing and future robotic spacecraft will be tasked to gather data from specific Mars surface sites within the candidate EZs to support further EMC studies and to assist in the process of selecting what is likely the first EZ to be explored. An advantage of repeated visits to a single surface site is that it makes investment in more extensive or elaborate infrastructure, such as a Rodriguez Well, easier to justify.

## **2.2 WATER USAGE ESTIMATES**

Many past studies of human Mars missions assumed a complete lack of water derivable from local sources, accepting an increased level of sophistication for systems like life support, and forgoing the opportunity to reduce the launch mass needed for consumables like propellants. However, in recognition of growing evidence for large quantities of accessible water in various forms, studies carried out as part of NASA's Evolvable Mars Campaign effort [13] examined the impacts of a "water rich" human Mars mission scenario [7]. In such a scenario, the human crews were assumed to have access to an essentially unlimited supply of water that could be applied to a variety of needs, including those previously assumed useful but not essential for mission success. Mission costs, such as additional equipment, time to collect and process, and site selection constraints, were estimated so these costs could be compared to (presumed) mission benefits, such as reduced payload mass (e.g., off-loaded propellant for the Mars ascent vehicle) sent to Mars, reduced system complexity (e.g., a simpler life support system), and other enhancements (e.g., enhanced radiation protection, crop growth, etc.).

Decision makers can use results from this sort of comparison to decide on the scope and scale of infrastructure that will be included with these human missions. This particular comparison can have a significant impact on several different aspects of a human Mars mission, making an accurate assessment of the mission "costs" of particular importance and thus placing a premium on an accurate simulation of water access and production.

To quantify the water demand of a “typical” crewed Mars surface mission in a “water rich” scenario, the NASA “Evolvable Mars Campaign” (EMC) characteristics previously mentioned were used in one representative assessment of these impacts [7]. In the EMC, each surface mission consists of a crew of four on the Martian surface for about 500 days, utilizing a central habitation module for crew living/working activities, spacesuits and pressurized rovers for remote exploration, and a single ascent vehicle for return to an orbiting interplanetary vehicle. Some of the other enhancements mentioned, such as crop growth, would be part of the research objectives investigated by the crew but not a primary element on which the crew will rely for mission success.

For each of these functional elements – habitation elements, spacesuits and pressurized rovers, and the ascent vehicle – the maximum use of Martian resources, including water, to reduce the amount of supplies required to be transported from Earth was investigated. Conceptual designs of the processing equipment and associated power systems was not performed in this assessment; instead, likely processing chemistry was used to estimate the water required in order to inform resource requirements. Appendix A describes these processes in more detail to provide a basis for estimating the quantities of water that these functional elements could use, as described in the following paragraphs.

Extensive design studies of the Mars Ascent Vehicle (MAV) – the vehicle used to return the crew from the surface to a waiting interplanetary transit vehicle –were performed as part of EMC analyses [14]. Typically, to maximize the benefit of in-situ produced propellant, the transportation architecture will be biased toward the highest Mars orbit practical for the MAV-to-interplanetary vehicle rendezvous. Such a vehicle concept is depicted in Figure 2.1 [15]. The total propellant load of oxygen and methane required for this MAV is 38,500 kg at an oxidizer-to-fuel (OF) ratio of 3.4. Given the water-to-product mass ratios from a water electrolysis plus Sabatier process (see Appendix A for details), this propellant load will require 19,700 kg (~5,210 gallons) of Martian water (and 24,100 kg of Martian CO<sub>2</sub>). Since the Sabatier/water electrolysis process produces oxygen and methane in a 4:1 ratio, approximately 5,200 kg of excess oxygen will be produced.

Traditional Mars surface habitation systems assume closed-loop (recyclable) water and oxygen systems for crew life support. Closed loop systems greatly reduce the mass requirements for these commodities if brought from Earth, but they are complex and, as experience on the International Space Station has indicated, prone to frequent repair and maintenance. In addition, the power and mass of these systems limit water usage to rather basic levels (e.g., no showers, no laundry, etc.).

With the availability of Martian water, the strategy for life support could change in several ways (this is not an exhaustive list, but some of the larger uses of water).

1. It could be advantageous to reduce the water and oxygen recycling levels to increase reliability or reduce system development costs, using in situ Martian water to make up the differences.
2. Systems could “temporarily” rely on Martian water to allow for repair and maintenance of closed-loop systems.
3. Life support could rely completely on Martian water for life support water and oxygen, thereby eliminating both development cost and mass of closed-loop systems.



Subsystem	Mass (kg)	
	MDM Payload	Mars Liftoff
<b>Crew Cabin</b>	<b>3,427</b>	<b>4,122</b>
Structures	881	881
Power	377	377
Avionics	407	407
Thermal	542	542
ECLS	502	502
Cargo	422	1,117
Non-Prop. Fluids	295	295
<b>1<sup>st</sup> Stage</b>	<b>9,913</b>	<b>31,432</b>
Dry Mass	3,605	3,605
LO <sub>2</sub>	0	21,519
LCH <sub>4</sub>	6,308	6,308
<b>2<sup>nd</sup> Stage</b>	<b>5,006</b>	<b>13,246</b>
Dry Mass	2,566	2,566
LO <sub>2</sub>	0	8,239
LCH <sub>4</sub>	2,440	2,440
<b>TOTALS</b>	<b>18,345</b>	<b>48,799</b>

**Figure 2.1. Mars Ascent Vehicle Conceptual Design**

Water resupply requirements for three levels of water usage scenarios – closed-loop, “restrained” open-loop, and “robust” open-loop – for a four-crew 500-day surface mission were estimated [16]; details can be found in Appendix A. This assessment found that the “restrained” open-loop case requirement is about 9,520 kg (~2,520 gallons), or about half of that required for propellant production. The addition of the laundry (the primary difference between the “restrained” case and the “robust” case) more than doubles that amount to about 24,380 kg (~6,550 gallons). In the latter case, the magnitude of life-support water needs are “in kind” with those of the MAV.

Outside of the Earth’s magnetosphere, there are generally two types of radiation that can impact crews’ health – Solar Particle Events (SPEs) and Galactic Cosmic Radiation (GCR). On the Martian surface, the SPEs are greatly attenuated (approximately an order of magnitude) [18] by the atmosphere. GCR is also somewhat attenuated. However, interaction between GCR ions and the atmospheric molecules result in a pion and electromagnetic cascade (“ $\pi$ /EM cascade”). In addition, collision between GCR ions and the Martian soil creates a neutron field (“albedo neutrons”). Both of these GCR effects contribute to the total exposure experienced by a crewmember on the Martian surface [18].

In spite of these attenuating effects, SPE and GCR exposure is still considered a health risk for the crew on these Mars missions. Consequently, the additional effectiveness of using Martian water as a shield was of interest, given the availability of water in this “water rich” scenario.

Consequently, this analysis assumed 20 g/cm<sup>2</sup> of water shielding – equivalent to a 20 cm thick water shell – around a Mars surface habitat. (Appendix A explains the rationale for selecting this water shell thickness.) Such a shell would provide about 15% effective dose reduction. Assuming the habitat is a vertically-oriented cylinder 7 m diameter and 6.5 m tall (typical of conceptual habitat designs considered in EMC assessments), this shell would be the equivalent

of 43,000 kg (~11,400 gallons) of water. Such a water shell could be combined with the water quantities previously calculated for a robust open-loop life support scenario. The radiation shield could represent a life-support water “buffer” or storage supply for such an open loop system. If configured correctly, this buffer would provide the additional benefit of (albeit limited) radiation shielding.

Pressurized rovers capable of carrying at least two crew for extended duration surface traverses are often envisioned for Mars missions. Power sources for these concepts are always problematic, however, especially in multi-day traverse scenarios. Hydrogen-oxygen fuel cells have been proposed as a power source [17], but the volumetric and cryogenic challenges of liquid hydrogen, along with the regeneration challenges of liquid hydrogen, have made this choice unattractive. However, Martian water combined with methane reformer technology may offer a better answer.

To characterize water requirements for this option (details are discussed in Appendix A.), rover and surface excursion parameters were postulated [19] and are shown in Table 2.1 (Note: 1 sol = 1 Martian day, 24.65 hrs.). As can be seen, the fuel cells produce 621 kg (~164 gallons) of water in excess of that required by the methane reformer, more than enough to supply the crew's potable water requirement during this postulated excursion (estimated at 100 kg for a crew of two). To estimate the total need over the duration of a 500-day surface mission, every excursion was assumed to use two rovers exploring in tandem to maintain mutual rescue capability in case of malfunction, and to be performed once every 28 sols, resulting in 18 excursions per 500 sol surface mission. This equates to a total requirement of 9,936 kg of methane and 30,276 kg of oxygen. Again, assuming Sabatier/electrolysis methane-oxygen production, this will require 22,400 kg (~5,900 gallons) of Martian water – similar in magnitude to the MAV propellant requirement.

**Table 2.1. Surface Excursion Characteristics**

<b>TRIP DURATION</b>	14 sols
<b>NO. OF DAYS DRIVING</b>	9 sols
<b>CREW</b>	2
<b>ROVER DRIVE TIME/SOL</b>	9 hours
<b>TOTAL ENERGY NEEDED</b>	1,564 kW-hrs
<b>TOTAL O<sub>2</sub> NEEDED</b>	841 kg
<b>TOTAL CH<sub>4</sub> NEEDED</b>	276 kg
<b>EXCESS H<sub>2</sub>O PRODUCED</b>	621 kg (~164 gallons)

By totaling the MAV, “robust” open-loop life-support and mobility requirements, the total “per mission” water extraction requirement can be estimated, shown in Table 2.2, assuming Martian water (and carbon dioxide) are the sole feedstock for the products.



**Table 2.2. Products and Required Feedstock (per Mission)**

	<b>O<sub>2</sub></b>	<b>CH<sub>4</sub></b>	<b>H<sub>2</sub>O</b>	<b>MARTIAN H<sub>2</sub>O REQUIRED</b>
<b>MAV</b>	29,758 kg	8,748 kg	N/A	19,683 kg
<b>LIFE SUPPORT</b>	N/A	N/A	24,379 kg	24,379 kg
<b>MOBILITY</b>	30,276 kg	9,936 kg	N/A	22,936 kg
<b>TOTAL</b>	<b>60,034 kg</b> <b>(~15,891</b> <b>gallons)</b>	<b>18,684 kg</b> <b>(~4,946</b> <b>gallons)</b>	<b>24,379 kg</b> <b>(~6,453 gallons)</b>	<b>66,998 kg</b> <b>(~17,735 gallons)</b>

Assuming a continuing series of human excursions to the Martian surface, the cadence of these missions will dictate the necessary commodity production rates and hence the water extraction rates. The EMC was predicated on a Mars surface mission on alternating Earth-Mars synodic periods, implying a mission every 50 months. Combined with the per-mission requirements of Table 2.2, this implies the steady-state water extraction and production rates shown in Table 2.3. If this mission cadence were to increase to one mission every Earth-Mars synodic period – an assumption made in Mars mission planning prior to the EMC – these values would double.

**Table 2.3. Commodity Extraction and Production Martian Water Rates**

<b>O<sub>2</sub> PRODUCTION</b>	14,141 kg/yr
<b>CH<sub>4</sub> PRODUCTION</b>	4,486 kg/yr
<b>H<sub>2</sub>O PRODUCTION</b>	5,853 kg/yr
<b>MARTIAN H<sub>2</sub>O REQUIRED</b>	<b>16,086 kg/yr</b> <b>(~4,258 gallons/yr)</b>

These tables provide an indication of the scope and scale of water extraction and processing concepts and the associated power requirements. If access to these quantities of water becomes a desired or required feature for human Mars exploration missions, one of the primary site selection criteria will be a location where at least 67 tons of water can be extracted for each crew visiting the site. Current planning calls for three or more crews to visit such a site, making the magnitude of required ice reserves at least several hundred tons. A technological solution that can reasonably access and process these quantities of ice into water will also be needed. The following sections will discuss these factors in more detail.



### 3.0 MARS WATER RESOURCES

As robotic missions continue to explore Mars from orbit and from the surface, the understanding of past and current sources of water is evolving. For utilization during human surface missions, the desire would be for water (or water ice) to be relatively concentrated, relatively accessible and in regions consistent with human mission/exploration objectives. In this context, “accessible” is defined by several key features, including a location that is at a latitude and altitude likely to be visited by human crews as well as close enough to the surface that drilling equipment can penetrate the overburden. For all of these factors, there is no single value that demarcates “accessible” from “inaccessible”; each must be evaluated in the context of all mission goals and constraints.

The potential “inventory” of Mars water can be divided into roughly six categories [20]. Each of these sources, and its relevance to human Mars missions, is described below.

#### 3.1 GENERAL WATER SOURCES ON MARS

**Polar Surface Water Ice:** Both the north and south Martian poles have permanent caps of water ice at latitudes greater than 80°. Both of these caps are covered by CO<sub>2</sub> ice during their respective winters. The CO<sub>2</sub> fully sublimates at the North Pole during northern summer, revealing a permanent cap of 90-100% pure H<sub>2</sub>O that is 100 km in diameter and 3 km thick. The south pole CO<sub>2</sub> deposits never fully sublime, leaving approximately 8 m of CO<sub>2</sub> ice covering most of the permanent cap of water ice, the size of which is not well known.

These regions are, however, not generally considered favorable for long duration human exploration due to long periods of seasonal darkness during local winter and the dynamic, low visibility conditions due to subliming CO<sub>2</sub> in local summer.

**Atmospheric Water Vapor:** The average water content of the Martian atmosphere is quite low at around 300 ppm, equating to 1 kg of water per 170,000 cubic meters of atmosphere. However, because the atmosphere is so thin, relative humidity can be quite high, reaching near saturation levels. Although direct collection does not appear attractive (e.g., through condensation) for use on a human mission, Martian water vapor may contribute to other water sources, as described below.

**Water Sequestered in Minerals:** The Mars Reconnaissance Orbiter’s (MRO) Compact Reconnaissance Imaging Spectrometer for Mars (CRISM) and Mars Express’ Infrared Mineralogical Mapping Spectrometer (OMEGA) have detected minerals that presumably formed in ancient Martian aqueous environments [21]. These hydrous mineral deposits are typically compact in size (around 3% of the Martian surface) but are distributed widely across the surface of Mars, consisting mostly of phyllosilicates (clay minerals), chlorites, and sulfates. Where they are found, the water content of these minerals may vary considerably, from around 2% to 9% by weight. Soil excavation and transport would be necessary to harvest the water bound in these minerals, and engineering studies have been performed [5] to determine the scope and scale of the operations needed to produce this water.

#### 3.2 NO LIQUID WATER AQUIFERS

“Recent” (<10 million years ago) presence of Martian groundwater has been inferred by outflow channel formations observed from orbit (Figure 3.1). It had been assumed that subsurface liquid water, in the form of aquifers, was located below a thin cryosphere and had “burst through” occasionally to form these features.

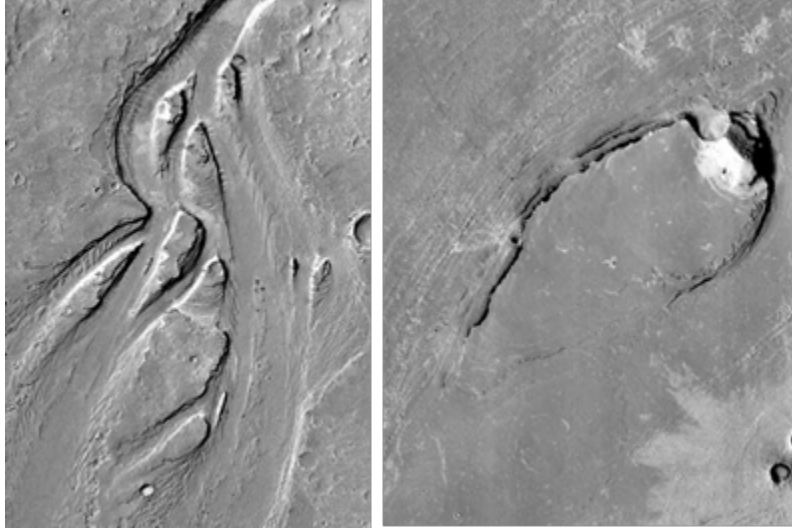


**Figure 3.1. Athabasca Valles, Images Courtesy NASA/JPL/Malin Space Science Systems**

Much more recently, dark, narrow (0.5 to 5.0 m) markings have been observed on steep ( $25^\circ$  to  $45^\circ$ ) slopes. MRO High Resolution Imaging Science Experiment (HiRISE) images show incremental growth during warm seasons and fading during cold seasons [22]. These “Recurring Slope Lineae” (RSL, Figure 3.2) have been interpreted as intermittent flows of briny liquid water and this was confirmed by the MRO CRISM spectrometer in 2015 [22]. However, the water source was unclear, and some interpreted this as more evidence of aquifers exposed by these slopes.

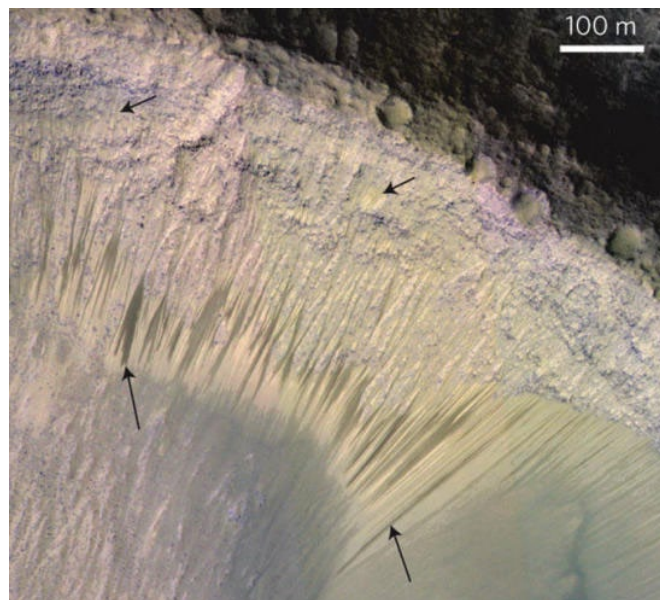


**Figure 3.2. Recurring Slope Lineae [16]. Image credit NASA/JPL/University of Arizona**

Other recent work [23] has cast doubt that any water is involved with these features, with any mass movement caused by “dry” phenomenon, driven by a variety of factors such as diurnal and seasonal temperature changes.

The Mars Express Mars Advanced Radar for Subsurface and Ionospheric Sounding (MARSIS) and the MRO Shallow Subsurface Radar (SHARAD) instruments were designed specifically to

detect such subsurface liquid water. However, to date MARSIS and SHARAD have failed to detect any indication of liquid water within 200-300 meters of the surface anywhere on Mars [24]. It may be that the formations depicted in Figure 3.1 are older than initially thought, and the groundwater is gone or is locked up in the subsurface cryosphere; alternatively, the flooding may have been caused by infrequent localized crustal heating and cryosphere melting. As for the RSL, atmospheric water vapor may be the “feedstock” for absorption by salty minerals (perchlorates and other hygroscopic salts), resulting in temporary muddy flows. In any event, the prospects of easily accessible subsurface liquid water appear unlikely anywhere on the planet.

The Mars Odyssey gamma ray/neutron spectrometer has confirmed previous predictions of extensive ground ice within one meter of the Martian surface poleward of 50° north and south latitude with a concentration of 20-90% [25] and an estimated thickness of 5-15 kilometers [24]. These measurements and predictions were confirmed by the Phoenix lander (landing site 68° N latitude) that excavated 99% pure ice only 2-6 centimeters from the surface (Figure 3.3).



**Figure 3.3. Ice Excavated by Phoenix Lander, Image NASA/JPL/University of Arizona, Texas A&M University**

Human missions are unlikely to select a landing site that is poleward of the Martian equivalent of the Arctic and Antarctic circles (65° north and south latitude) to avoid spending an entire surface mission in the total darkness of a local winter – transfer trajectories to Mars can arrive at any time of the Martian year depending on the opportunity. This leaves a band between about 50° and 65° latitude that could support a human landing site with a source of indigenous water. But the form of this water is still uncertain.

### **3.3 TERRAIN FEATURES INDICATING BURIED ICE**

Certain Martian terrain features suggest large-scale mid-latitude glaciation, potentially driven by changes in the obliquity of Mars’ rotation axis. These Lobate Debris Aprons (LDAs), Lineated Valley Fills (LVFs) and Concentric Crater Fills (CCFs) [26] all bear similarity to terrestrial glaciation features (Figure 3.4) and are widely distributed in the Martian mid-latitudes (Figure 3.5).



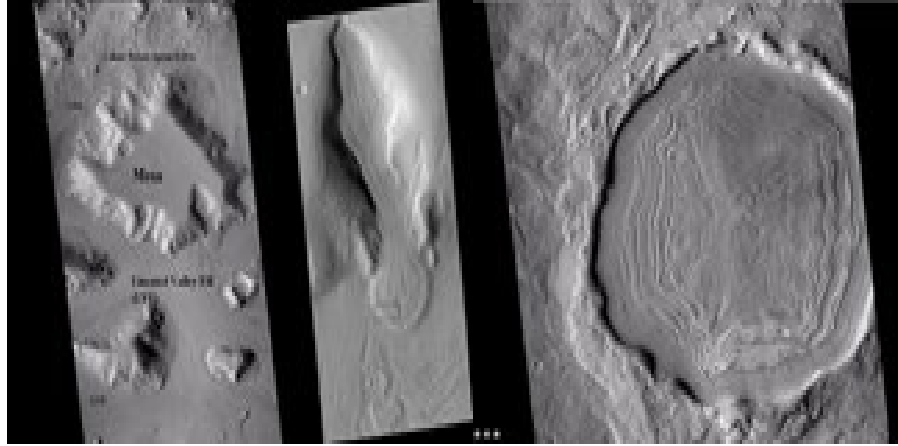


Figure 3.4. LDA, LVF and CCF Martian Glaciation Features (MRO Context Camera)

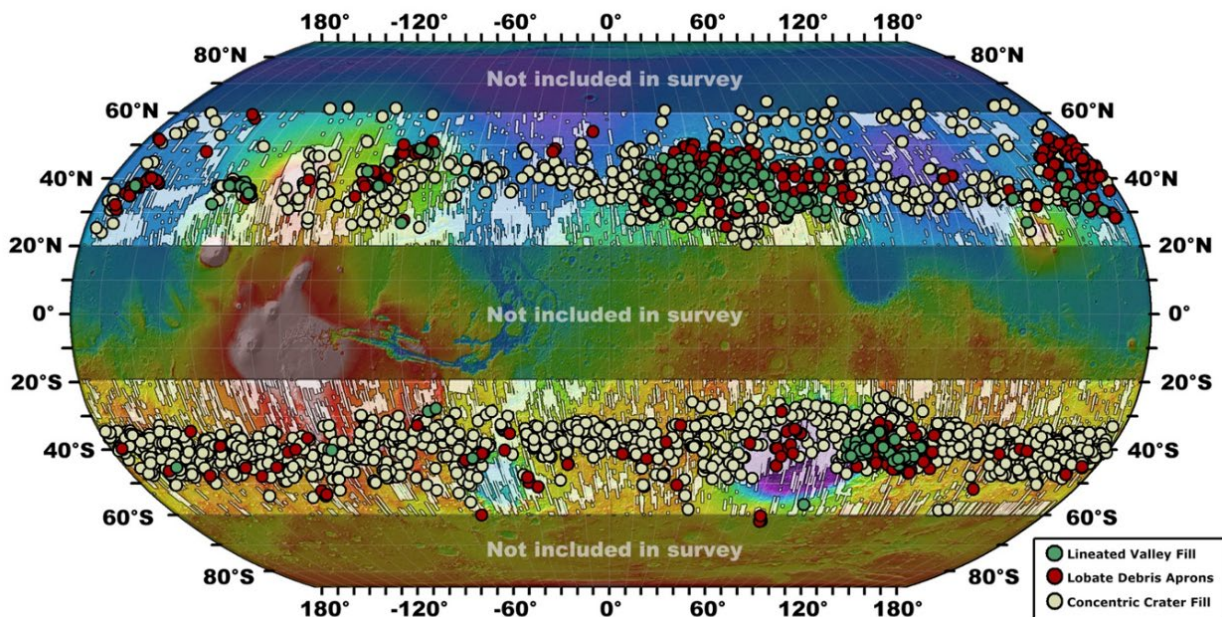
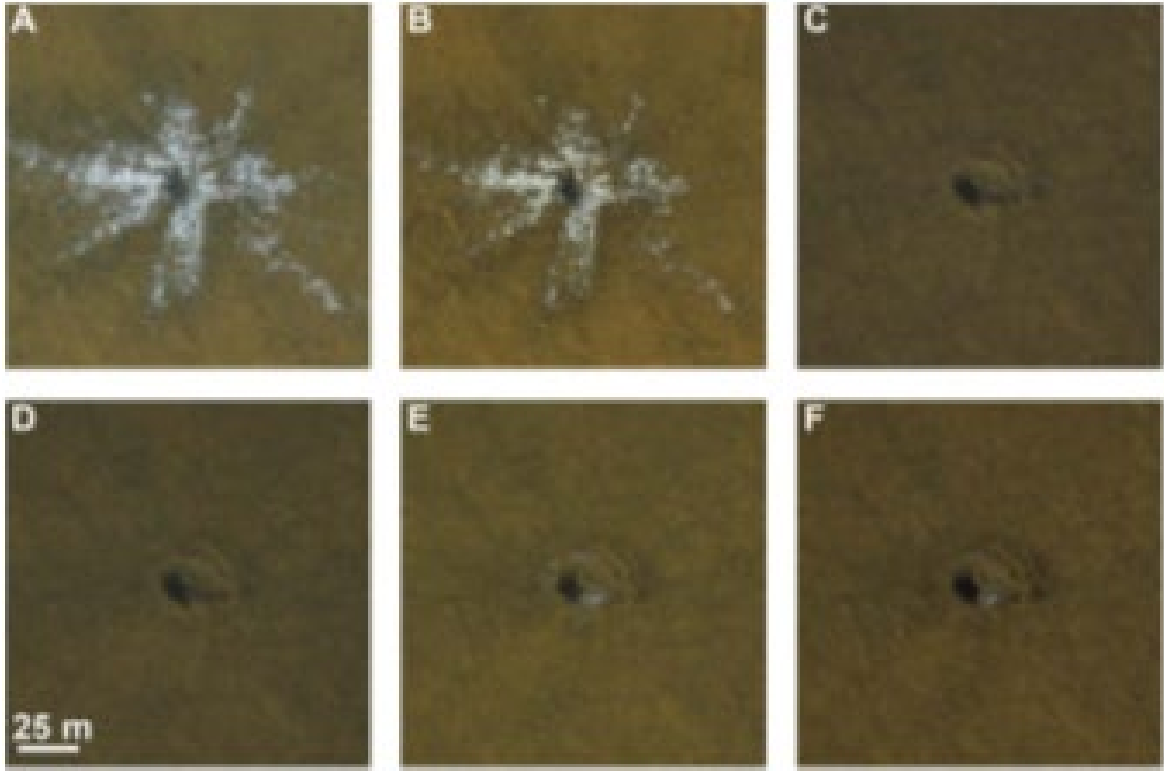


Figure 3.5. Global Distribution of LDA, LVF and CCF Features [26]

Fresh impact craters in these suspected glacial regions detected by the MRO HiRISE imager [28] actually show excavated, clean ice – verified by the CRISM spectrometer (<1% regolith content). The excavated material has been observed to sublime away over several months' time in subsequent images (Figure 3.6). The excavation depths are estimated to be less than two meters.



**Figure 3.6. Impact Crater Ice Excavation and Sublimation [22]**

As an additional line of evidence, the MRO SHARAD radar took soundings of LDAs in both the northern and southern mid-latitudes and obtained results completely consistent with massive layers (100s of meters thick) of relatively pure (>90%) water ice covered by a relatively thin (0.5 to 10 m) debris layer [27].

Recent discoveries reinforce these indications regarding the location and form of buried ice sheets. In January 2018, Dundas et al. [4] published visual evidence of the ice sheets thought to be buried within these terrain features. Several examples of exposed ice scarps are shown in Figure 3.7. Spectral data, gathered by the MRO CRISM instrument, have shown that these exposed features are almost pure water ice.

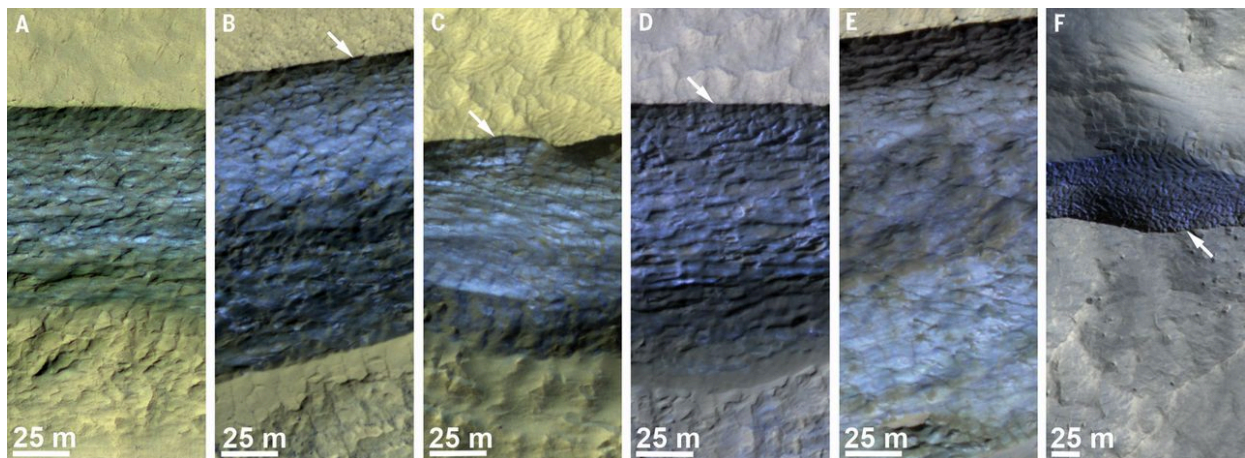


**Figure 3.7. Examples of recently discovery exposed ice scarps on Mars [4]**



To provide a sense of scale, Figure 3.8 shows one of these exposed ice scarps with an SLS (cargo) launch vehicle at the same scale. In addition, the previously mentioned 68 metric tons of water that could be used by a single crew of four during a 500 sol Mars surface mission (see section 2) is also shown to scale. These exposed sections of buried ice sheets are a relatively small portion of the entire body of ice with which they are associated. This visual comparison indicates that the quantities of ice available for making water vastly out-scale the need for at least these early surface missions.

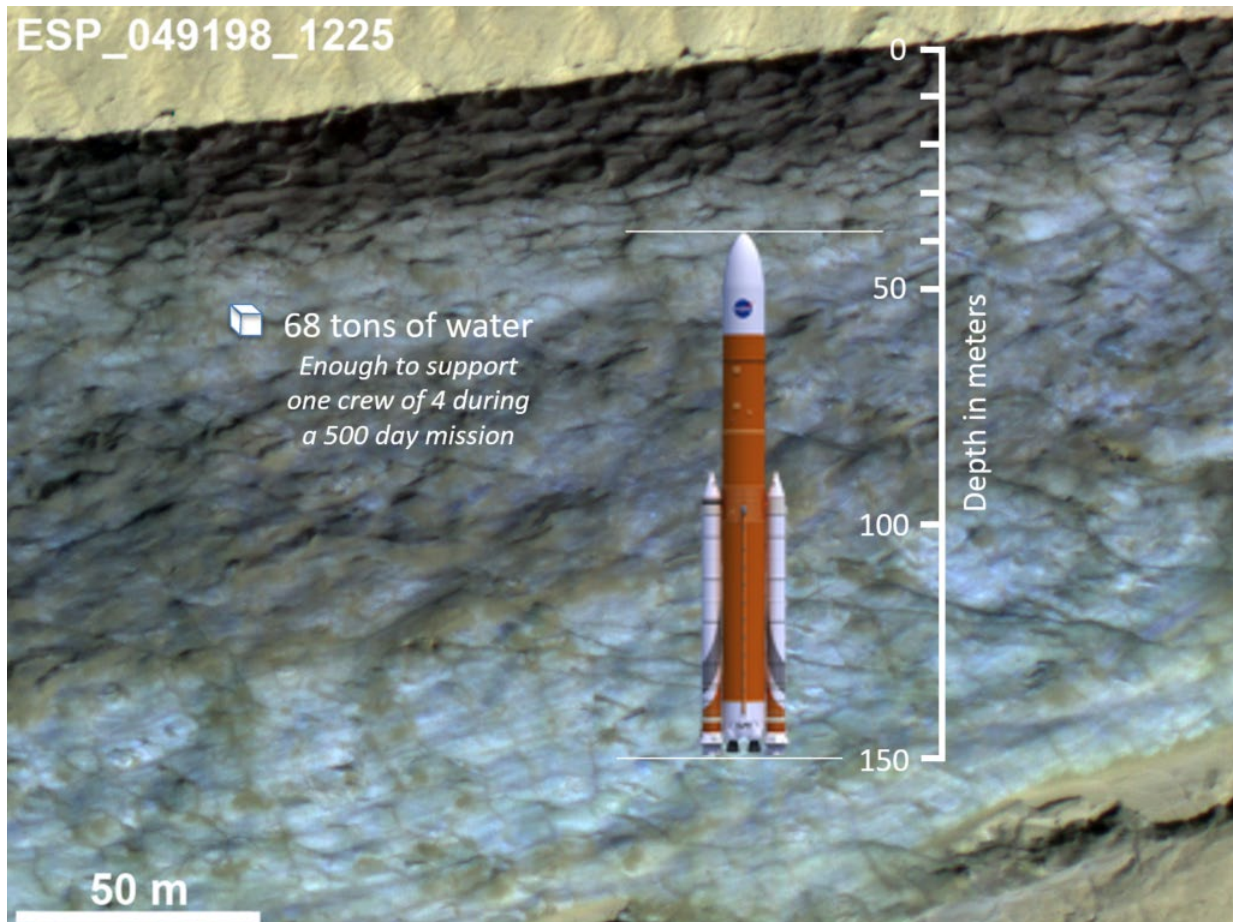


**Figure 3.8. Visual comparison for scale of exposed ice scarps on Mars with systems likely to be used for these Mars missions [4]**

The Dundas et al. group has been able to locate eight examples of exposed ice scarps, each measuring tens of meters in height. The location of these scarps, shown in Figure 3.9, are located well north and south of the equator, but still within the range of sites considered reasonable for future human missions [12]. Even though the number of examples are relatively few and their locations are at relatively high latitudes, their significance for future human missions rests in the fact that we now have a clearer picture of what lies buried at the dozens of other similar terrain features located in a wide swath in both the northern and southern hemispheres (Figure 3.9).

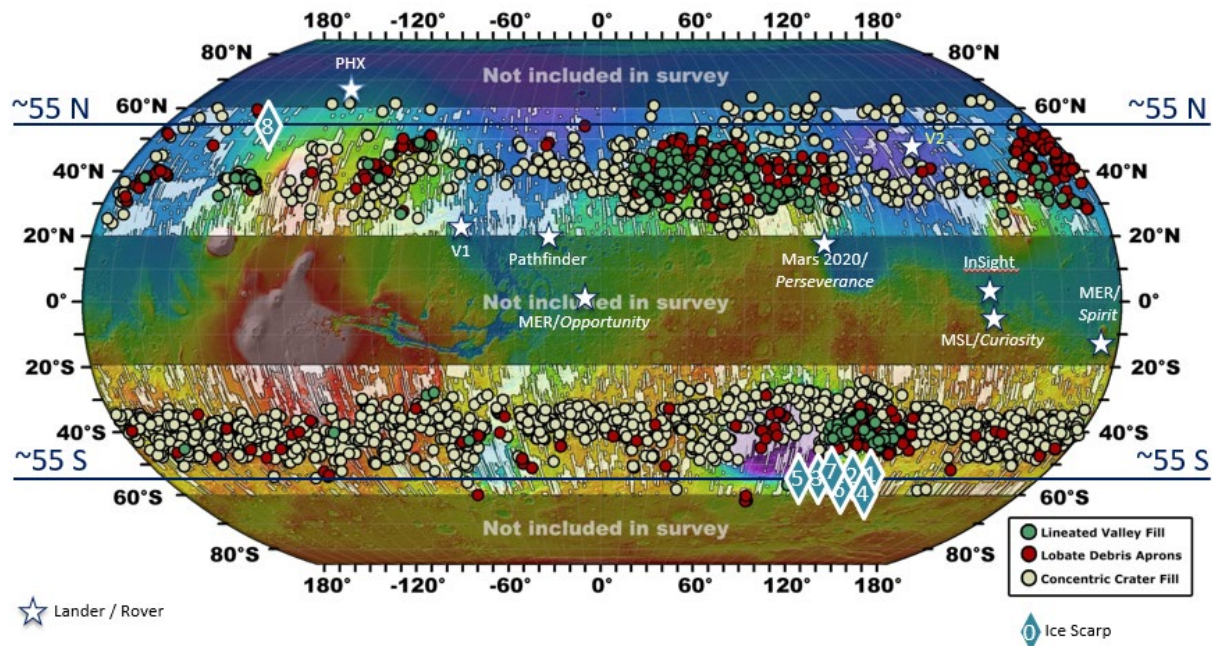


Figure 3.9. Location of ice scarps identified by Dundas et al [4]

Unfortunately, the radars mentioned above were designed to look deep under the surface, and consequently cannot resolve near-surface features with much resolution. Dundas et al. [4] were able to use visual data they gathered along with other sources to postulate a vertical profile of these ice sheets. This profile, shown in Figure 3.10, indicates that the overlying debris layer is likely to be just a few meters thick at the latitudes where they have located these scarps. The same theory that predicted the icy soils at high latitudes suggests that this debris layer will likely get thicker for terrain features that are closer to the equator [24]. But these estimated depths are not so great that drilling through the debris layer would be considered unreasonable for the latitude band shown in Figure 3.9.

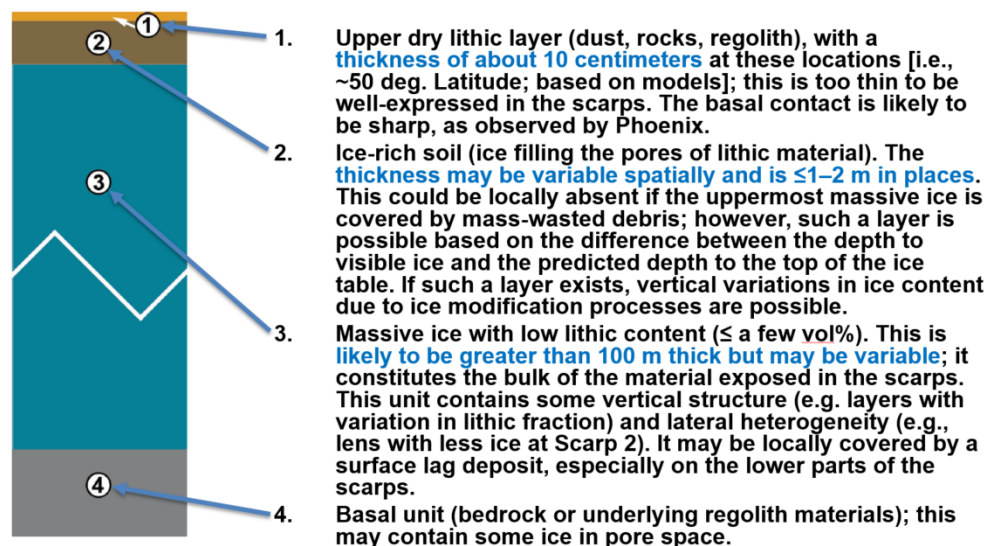


Figure 3.10. Hypothesized profile through Mars ice scarps identified by Dundas et al. [4]

## 4.0 RODRIGUEZ WELL HISTORY

The years following World War II were a period of growing tension between the United States and the Soviet Union and their respective allies. The United States and Canada began building a series of military outposts in the polar regions of Alaska and northern Canada to guard against attacks by bombers and missiles from the Soviet Union. These outposts included early warning radar stations, such as the Distant Early Warning (DEW) line, as well as interceptor control stations such as aircraft control and warning (AC&W) radar stations. Both types of stations were eventually built on Greenland (a territory of Denmark) to expand the coverage range.

Many of the AC&W stations were built during early 1950's; the DEW line construction began in December 1954. As many as 25,000 people were involved in the rapid buildup of the DEW line, constructing all manner of physical facilities, such as buildings, roads, tanks, towers, antennas, airfields, and hangars.

In 1953, in anticipation of this extensive construction program, the U.S. Army initiated a research and development program to facilitate sustained military operations in the far north. This included a Greenland Research and Development Program, the purpose of which was to identify solutions to "engineering and associated problems" required to develop, maintain, and supply camps on the Greenland ice cap. During the summer of 1953, a team of Army scientists visited Greenland to consider the specific problem of constructing camps on the ice cap. Their considerations included the use of snow as a construction material, foundations on snow, the control of snow, and issues of habitation including power, water supply, and wastewater [29].

The Greenland Research and Development Program led directly to many of the construction and camp infrastructure techniques still in use today. In particular, this program led directly to the development of the Rodriguez Well. Not long after this technique was field tested, it was put into operation during the 1960's supporting Camp Century and Camp Tuto's "Under-Ice Camp" on Greenland. During the 1970's, a Rodriguez Well was tested at the Amundsen-Scott South Pole Station, in the hope that it would also prove to be a useful piece of station infrastructure, in spite of ice temperatures and some structural properties that differed from those found in Greenland. Although not put into immediate use at South Pole Station, it did become part of the operational infrastructure when the new South Pole Station facility was constructed in the 1990's. The Rodriguez Well remains the primary source of water for the South Pole Station to this day.

Providing potable water is not the only use for the Rodriguez Well technique. The South Pole Station Rodriguez Well has also been leveraged for scientific purposes. It has been periodically "mined" for micrometeorites that have fallen on the Antarctic ice sheet, been sequestered in the ice, and then "released" as the ice is melted for use as potable water [32]. In addition, a Rodriguez Well was started, operated, and shut down each austral summer season between 2004 and 2011 to support construction of the IceCube Neutrino Observatory at the South Pole.

The following sections will discuss this progression of development and usage in more detail.

### 4.1 EARLY USAGE

Camp Fistclench. Following a visit to the Greenland Ice Cap by a group of their scientists in 1953, the U.S. Army decided to establish a camp there during the summer of 1954, at which construction techniques and infrastructure support approaches could be researched and tested. This camp – Camp Fistclench – was co-located with the existing Ice Cap Air Station (station designator: G-34, aka "B-site" or "Site II"), an AC&W station located approximately 220 miles (354 kilometers) ENE of Thule Air Base, taking advantage of the established infrastructure and logistical support for this station (Figure 4.1).



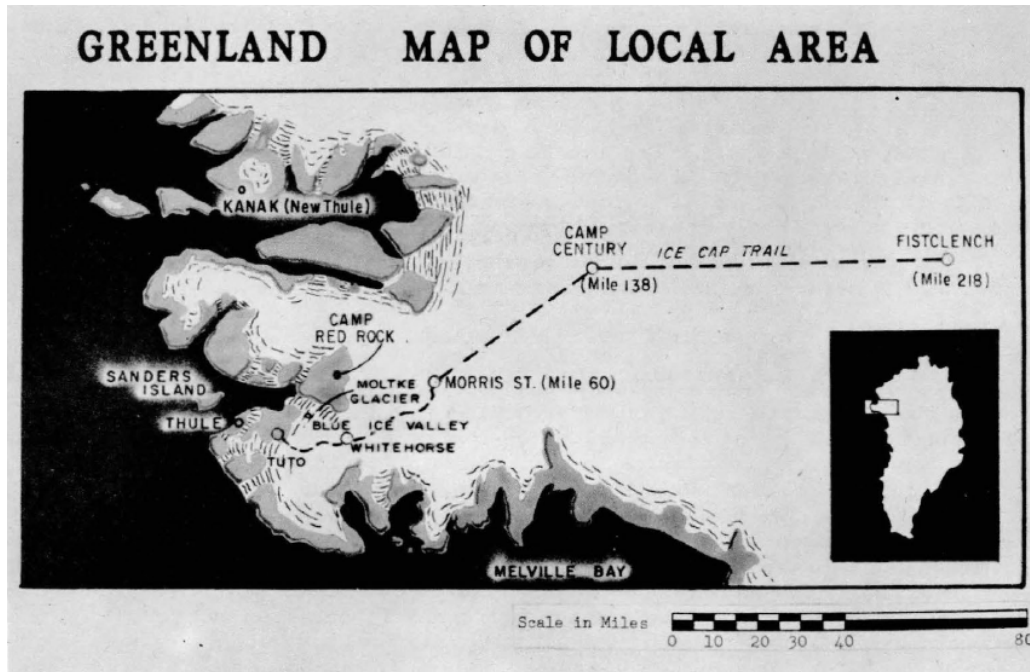


**Figure 4.1 Location of Greenland Ice-Cap Stations near Thule Air Base [30]**

In 1955 Dr. Henri Bader, Chief Scientist of the U.S. Army Snow, Ice and Permafrost Research Establishment (USA SIPRE, now redesignated the U.S. Army Cold Regions Research and Engineering Laboratory [USA CRREL]), began advocating water production for ice-cap camps by melting a shaft into the ice to a depth of approximately 100 feet [30.5 meters], where the snow has a density of about  $0.70 \text{ g/cm}^3$  and is impermeable to water. Then, with the use of steam jets, a pool of water sufficiently large to satisfy camp requirements could be melted and maintained. The water could be pumped into storage tanks by means of a deep well pump [30]. This concept is shown in Figure 4.2.

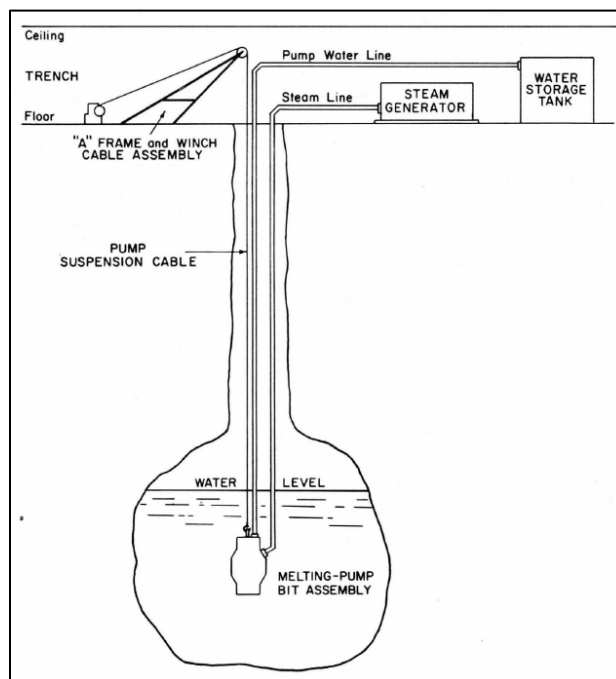


**Figure 4.2 Schematic sketch of water well and equipment [30].**

Bader's concept was based upon his observations of the sewage disposal system at Site II, where water-borne sewage, which was dumped into a pit, rapidly melted its way down to a depth of about 100 feet. It then ponded and created a pool of ever increasing size that remained in a liquid state as long as the heat input was continued.<sup>1</sup>

Prior to this proposed approach, potable water for ice-cap stations was provided from snow melting systems. Clean snow would be loaded into large containers, by hand or using large machines such as front end loaders, and melted using dedicated heaters or scavenging waste heat from electrical generators, both of which use liquid fuels that must be supplied to the ice-cap station. The advantages of Bader's concept over the conventional snow melter were obvious. Not only would less manpower be required in the production of water, but an abundance of water could be produced at less cost per gallon.

In 1958, a task was assigned to the U.S. Army Engineer Research and Development Laboratory (USAERDL) to test the ice-cap well concept. In 1959, Mr. Raul Rodriguez, a USAERDL employee, assembled the-necessary equipment (steam generator, flexible steam pipes, steam nozzles, deep well pumps, storage tanks, winch, etc.) and conducted a field test at Camp Fistclench. The equipment consisted mostly of modified commercial items. His tests led to a water supply system that is now known as the "Rodriguez Well" [30]. (USAERDL Technical Report No. 1737 documents the success of this test.) Being only a test of the concept, this well was not used to support the potable water needs of Camp Fistclench, but the concept was considered sufficiently proven to be included in the design of Camp Century.

Camp Century. Early in 1958 plans for a modular-type, semi-portable nuclear reactor power plant (the PM-2A Nuclear Power Plant) to be installed on the ice cap had been completed, approved, and funds for its construction had been programmed and promised by the Department of the Army, but the site for its installation had not been selected. One option was to locate the reactor at the existing Camp Fistclench. However, the austere prototype undersnow camp at Camp Fistclench had not been designed to accommodate such a plant. Furthermore, Camp Fistclench was located approximately 220 miles from Camp Tuto, the staging location for over-the-ice resupply convoys supporting Ice Cap Air Station and Camp Fistclench (see Figure 4.1). Selection of that location would have imposed an unnecessary logistical burden in terms of surface transportation, since all of the research and development to be conducted there could also be accomplished nearer to the ice cap edge and much closer to Camp Tuto. In addition, from the research point of view, construction of a new camp, incorporating all of the methods and techniques that had been developed during the preceding four years, seemed highly desirable. Based on these considerations, a decision was made to construct a new camp – Camp Century – that would incorporate all of the previously developed ice cap construction methods and techniques [30].

Detailed design plans and specifications for Camp Century were accomplished during the latter part of 1958 and early 1959. This camp was intended from the outset to be a large-scale, continuously occupied facility with a design life of 10 years. The plans specifically called out the use of a water well as the source for potable water and for other uses. Among the other users of water was the PM-2A Nuclear Power Plant that would provide electrical power for the camp. Actual construction of the camp was started in June of 1959 and completed in October 1960.

---

<sup>1</sup> Dr. Bader documented several recommendations for ice camp operations in a series of SPIRE reports following the 1953 Greenland visit by a group of U.S. Army scientists. Sewage disposal and thoughts on water wells were documented in Bader, Henri and Small, F. A. (1955) Sewage disposal at ice cap installations, U. S. Army Snow, Ice and Permafrost Research Establishment, SIPRE Report 21.

The Rodriguez Well was installed during the summer of 1960, less than a year after the successful field trials at Camp Fistclench.

The major items of equipment used for Camp Century's Rodriguez Well consisted of:

- A diesel-fired steam generator capable of producing 165 psi (1.14 MPa) of saturated steam at 373° F (190° C) and at a rate of about 800 pounds per hour (227 kW).<sup>2</sup>
- A melting-drill bit assembly for melting a well shaft into the ice.
- A melting-pump bit assembly for melting the glacial ice and pumping the melt to the surface.

The submersible pump had a capacity of 1700 gal/hr (6435 liters/hr) pumping from 200 ft (60 m) depth, and 1020 gal/hr (3860 liters/hr) from 150-m (500-ft) depth [9].

- A gasoline engine-powered cable winch for raising and lowering the bit assemblies.
- An A-frame and two wanigans.<sup>3</sup>
- A 5,000-gallon (18,900 liter) insulated and heated water storage tank.
- A rubber hose to convey the steam from the generator to the bit assemblies, and to convey the melt from the pool to the storage tank.

Figure 4.2 illustrates how these items were assembled for use at the Rodriguez Well and Figure 4.3 shows how the second of the two Camp Century wells evolved over two years of use.

Performance of Camp Century's Rodriguez well, as reported by Lt. Col. Elmer Clark (ret.) [30] was as follows:

This equipment functioned efficiently and easily produced sufficient water to satisfy all camp requirements, including those of the PM-2A Nuclear Power Plant. Owing to the fact that the well had reached a depth of over 500 feet (150 meters), which was nearing the maximum head for the type of deep well pump in use, the well was relocated in May 1962 after approximately 3,500,000 gallons (13,200,000 liters or 13,200 tons) of water had been produced. More than 5,000,000 gallons (18,900,000 liters or 18,900 tons) had been pumped from the new well as of September 1964 [the camp operated for one more year, closing in the summer of 1965].

The quality of the water obtained from the well was excellent and suitable for drinking without filtration or chlorination. Raul Rodriguez, during his installation and testing of the well equipment, obtained several water samples that he shipped to the Sanitary Engineering Branch at USAERDL for analysis. The results of these analyses indicated that the ice melt was better in quality than water obtained by triple distillation in glass.<sup>4</sup>

---

<sup>2</sup> This diesel-fired steam generator was installed as a standby heat source. The primary source of heat for the Rodriguez Well was the 106 Btu/hr (approximately 300 kW thermal) produced by the PM-2A Nuclear Power Plant.

<sup>3</sup> Wanigans were small shelters – typically mounted on skis or cargo sleds – used primarily as workshops and for storage of tools and equipment, but could also be used for warming personnel or even sleeping if necessary.

<sup>4</sup> Lt. Col. Elmer Clark indicated that these water quality results were documented in detail in a separate report: Rodriguez, Raul (1963) Development of glacial subsurface water supply and sewage systems, U.S. Army Engineer Research and Development Laboratory, Technical Report 1737-TR.

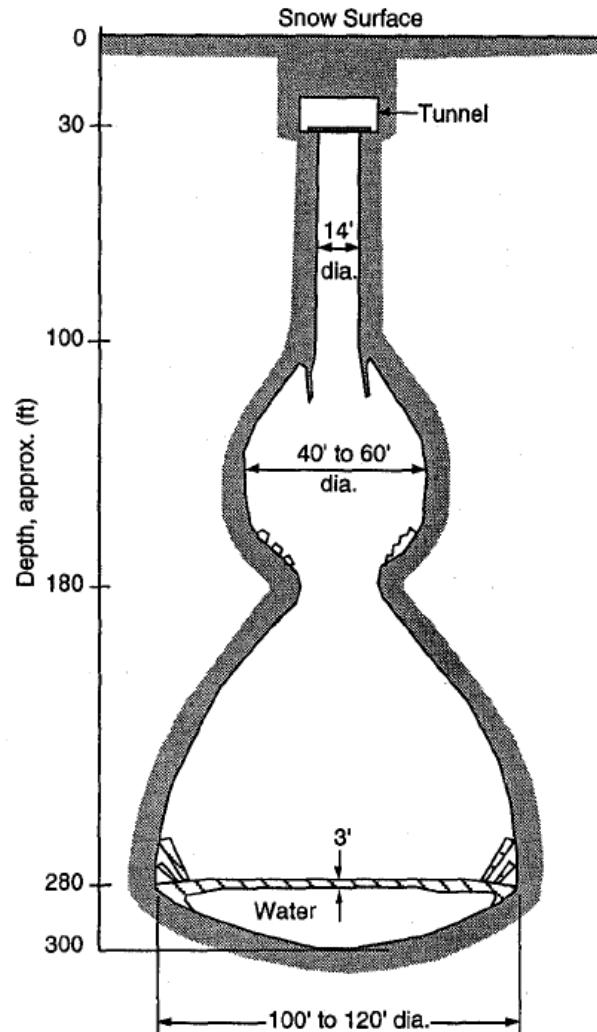


**Figure 4.3. Second Rodriguez Well at Camp Century after two years of operation [9].**

Camp Tuto Under-Ice Camp. The establishment of a growing number of seasonal and permanent military installations on the Greenland ice sheet came with the need for periodic resupply of these installations with equipment and logistics. Resupply by air was feasible but at a significant cost. The U.S. Army Transportation Corps began operating resupply convoys across the ice for large quantities of bulk items (e.g., food, fuel, etc.) and large or heavy items using heavy equipment (e.g., large caterpillar tractors) and cargo sleds. These items were typically delivered by cargo ship to coastal facilities and then reorganized for movement by land and ice to the inland stations and camps.

The North Star Bay harbor facilities were built to supply Thule Air Base and nearby installations. The transition between the Greenland ice sheet and ice-free coastal land is typically jumbled terrain with steep slopes. A ramp was constructed some 14 miles (22.5 kilometers) inland from Thule Air Base at this transition to facilitate heavy equipment and cargo sleds in moving on to the ice sheet. Camp Tuto (a foreshortening of "Thule Take Off") was the name given to the staging area at the base of this ramp where equipment and cargo was prepared for convoys to ice camps and other operations on the ice. A variety of other support functions and research activities occurred year-round at the camp, with the on-site population growing and shrinking based on these activities.

One of the research activities involved the use of mechanized continuous coal mining equipment to create a tunnel system in a vertical ice cliff adjacent to Camp Tuto. An under-ice camp was constructed in this tunnel system to study the interior of the ice sheet but also to test techniques for living and working in such an environment (see Figure 4.3). These studies complemented those being conducted at Camp Fistclench.

**Figure 4.4. Plan of Camp Tuto Ice Tunnel and Constructed Facilities [31]**

Camp infrastructure included all of the typical features of a larger camp, including living quarters, a kitchen and dining area, and a latrine with showers. Electricity was generated by two D-13000 Caterpillar diesel engines driving a 75 kW generator, located in one of the ice tunnel sections. Hot and cold running water was supplied for cooking, hygiene, and general heating from a Rodriguez Well under a different section of the ice tunnel. The energy to create and sustain this water reservoir was supplied from a heat exchanger tied to the cooling system of one of the two diesel engines.

Data collected from the operation of the under-ice camp included detailed measurements of the waste heat produced by the diesel engines and the production of water in the Rodriguez Well (see [31] for detailed data). Figure 4.4 shows the growth of the Rodriguez Well during the roughly 15 week test period. By the end of the test, the excess heat from one diesel engine generated more water than was needed to supply the domestic water needs of the camp's 25-person population. Total water usage during the test period was approximately 60,400 gallons



(228,000 liters or 228 tons). At the completion of the test approximately 106,400 gallons (403,000 liters or 403 tons) remained in the well.

“Old” Amundsen-Scott South Pole Station. An experimental well similar in purpose to that developed at the Camp Fistclench was developed during the austral summer of 1972-73 at the “old” Amundsen-Scott South Pole Station. The significant difference between wells developed at these two sites was the temperature of the firm and ice through which the well penetrated: ambient firm temperature of -51°C (-60°F) at the South Pole site, compared to a firm temperature of -28.9°C (-20°F) at Greenland sites. Despite the temperature difference, the water well functioned well without significant problems.

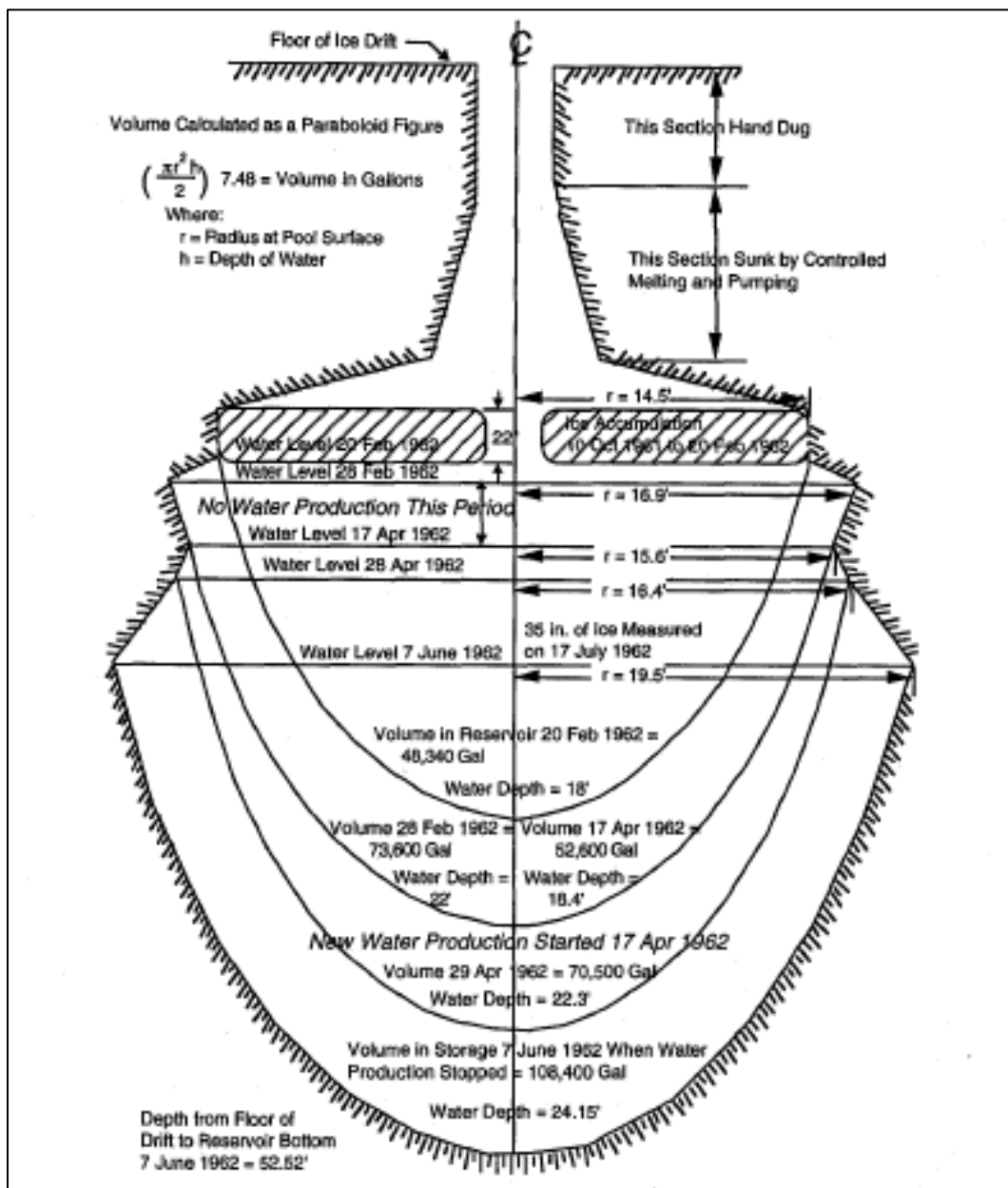
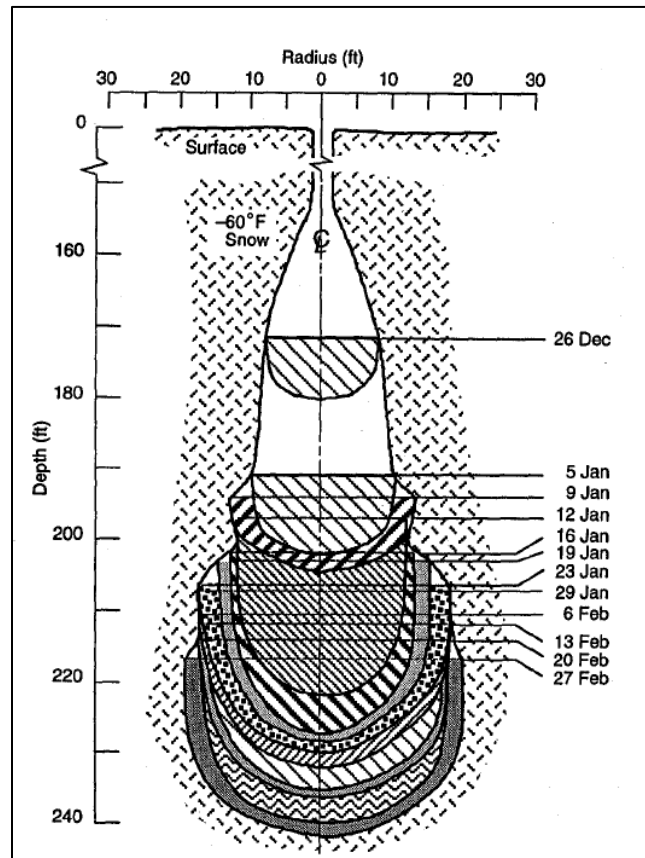


Figure 4.5. Camp Tuto water well development during 15 week test period. The majority of the water from this well was produced between 17 April and 7 June 1962. [31]

This well was started on 16 December 1972 and was halted (due to a failure of the steam generator used for melting ice) on 3 March 1973. The well was shut down and abandoned after supplying about 416,400 liters (416 tons or 110,000 gallons) of potable water. The evolution of this well is shown in Figure 4.6.



**Figure 4.6. Experimental Rodriguez Well evolution at the Amundsen-Scott South Pole Station [9].**

## 4.2 CURRENT USAGE

“New” Amundsen-Scott South Pole Station. Following the successful demonstration of a Rodriguez Well at the South Pole, a decision was made to use this technique as the potable water source in the design of the “new” Amundsen-Scott South Pole Station that was being constructed in the 1990s.

The South Pole Water Well (SPWW) began construction on the first well during the 1992-1993 austral summer season. The SPWW was certified as a source of potable water in early 1994. On 26 February 1994, the pool was about 16 m (52.5 ft) deep and 22 m (72.0 ft) in diameter, and the well bottom was 101 m (301 ft) below the well house floor. However, before the well was placed into operational use, an electrical fire in the pump cable on 1 March 1994 forced a 9-month shutdown. During the shutdown, a 4-m-thick (13 ft) ice layer formed on the pool surface and 6–11 m (20–36 ft) of freeze back occurred on the walls and bottom. The well was restarted in December 1994 by drilling through the ice layer and recirculating warm water as before. By March 1995, the well had melted below the pre-fire level [32].

The SPWW has supplied potable water to the Amundsen-Scott South Pole Station since January 1995. Once this well reached a depth of approximately 150 m (500 ft), the submersible

pump could no longer reasonably lift water to the surface. As the first well was approaching this depth in the early 2000s, a second well was started during the 2001-2002 austral summer season. The second well lasted until the early 2010's, when a third well was started. The South Pole Station is currently drawing water from this third well. Approximately 530,000 gal/yr (approximately 2,005,000 liters/yr or 2,005 tons/yr) are withdrawn on average to support the Station [35].

An additional benefit from these wells is the opportunity to “mine” them for micrometeorites that rained on to the Antarctic ice sheet over the previous millennia. Micrometeorites have been collected for many years from a variety of sources, including ice cores, sediments, desert sands and collectors flown on U-2 aircraft. A group of researchers began collecting micrometeorites from the SPWW during the 1995-1996 austral summer season [32]. They had originally planned to gather the micrometeorites at the bottom of the well annually, when the well's pumps and hoses were removed for maintenance. However, to avoid interfering with, or being interfered by, the maintenance activities, a second access hole – about 2 m (6.5 ft) from the central hole – was drilled for collection [32]. Since this first collection the collecting of micrometeorites has occurred periodically in all three of the Rodwells. Because of the volume of ice melted during normal operations, the SPWW has become the largest single source of micrometeorites. Results from investigations using these collected meteorites have been published in several articles [36, 37, 38, 39, 44].

IceCube Neutrino Observatory. The IceCube Neutrino Observatory is the world's largest neutrino detector. It occupies approximately one cubic kilometer of volume in the clear, dark ice below the Amundsen-Scott South Pole Station (see Figure 4.7). Eighty-six strings of 60 highly sensitive optical sensors, each string measuring 1000 meters in length, make up the observatory's primary detector. Each string of sensors is mounted in its own vertical shaft in the ice, starting at a depth of 1450 meters below the surface and extending to just above the local bedrock, at a depth of 2450 meters.

To create this observatory, a very large hot water drill was used to rapidly drill each of the 60 cm (23.6 in) diameter shafts [33]. Even with this large drill, the 86 shafts required seven field seasons (approximately 21 months total time) to create. As each string of detectors was put into position, the shaft was backfilled with water to freeze the sensor string in place. Water was captured from drilling each shaft to use for this backfill process.

However, some of this water was lost during the drilling process. In theory, ~57,000 liters [~57 tons or ~15,000 gallons] of make-up water was required for each IceCube hole, but in practice 95,000 liters [95 tons or ~25,000 gallons] per hole was required due to percolation loss into the lower firn layers at the top of the hole and water spent during the beginning and completion phases of each hole [33].

To create this make-up water, a Rodriguez Well was created each summer season. With an average of 12 shafts being drilled each season, the Rodriguez Well needed to create at least 1,140,000 liters (1,140 tons or 300,000 gallons) of water. Each well was shut down at the end of the season and a new well created the next season, usually in a different location to keep it close to the drilling operation.

Given the relatively short duration of the summer season at the South Pole, the drilling team became quite adept at rapidly creating and then maintaining the Rodriguez Well needed for their operations. Their seven Rodriguez Wells were used to create almost 8,000,000 liters (almost 8,000 tons or almost 2,500,000 gallons) of water to complete the IceCube Neutrino Observatory.



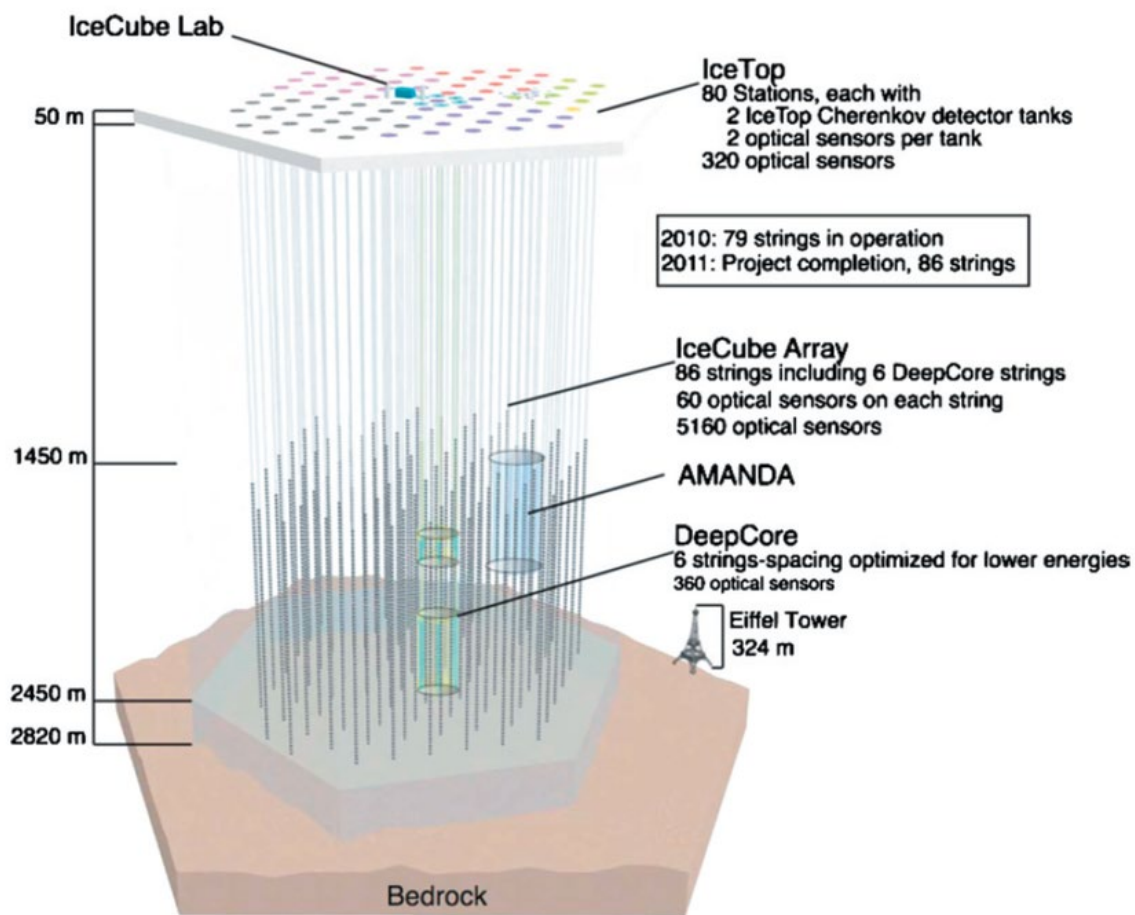


Figure 4.7. The IceCube Neutrino Observatory configuration, located at the South Pole.<sup>5</sup>

### 4.3 APPLICABILITY TO MARS

These examples provide a number of observations and lessons that are pertinent to the use of the Rodriguez Well technique on future human missions to Mars. Table 4.1 summarizes some of the key relevant characteristics of the examples described above. As a reminder, the water quantity usage estimated in Section 2 for future human Mars mission was approximately 67 tons (approximately 18,000 gallons) to support crew of four during a 500-day mission and including other propellant and construction uses.

As seen in these examples, the Rodriguez Well technique has been in use for over 60 years. During that time, the technique has advanced from a concept to operational use in which a large number of people rely on these wells for potable water – for almost five years at Camp Century and going on 25 years at the Amundsen-Scott South Pole Station. As such, the Rodriguez Well can be considered a mature technology that is routinely used in an operationally hostile environment. In the NASA parlance, these hostile environments would be considered a relevant

<sup>5</sup> Image credit: Nasa-verve - IceCube Science Team - Francis Halzen, Department of Physics, University of Wisconsin, CC BY 3.0, <https://commons.wikimedia.org/w/index.php?curid=26350372>

testing environment, but not an actual flight test when considered for Mars mission applications. As such, the Rodriguez Well would be considered to have achieved a Technology Readiness Level (TRL) of 6 (definition: a fully functional prototype or representational model at the system or subsystem level operating in a relevant environment – ground or space). Some of the subsystems – for example, the submersible water circulation and pumping equipment – should operate on Mars without modification (except perhaps weight reduction). Surface equipment modifications, or use of alternative technologies, will depend on the specific implementation designed. Experiments described in subsequent chapters are among the first steps necessary to advance this technology to a TRL of 7.

These examples also illustrate the use of the Rodriguez Well beyond the production of potable water for crew uses. The IceCube Neutrino Observatory used water from multiple Rodriguez Wells as a construction material, and it is a simple extrapolation to envision water use for radiation shielding surrounding human habitats on Mars, and for the production of propellants for both surface transportation and to orbit. These wells have also found complementary uses, achieving multiple infrastructure requirements – such as cooling for power production systems while generating potable water – or supporting scientific investigations as a byproduct of providing water, and in so doing accomplishing infrastructure support more efficiently.

In addition, all of these examples illustrate that the Rodriguez Well can be successfully used intermittently. Both Camp Century and South Pole have stopped water production, allowed the water pool to freeze, and then remelted the water pool at a later time. IceCube annually started or restarted wells for seven years. Thus, dormancy of the well could be a feature of a Mars surface station or facility that is not continuously occupied by crew, but periodically visited over many years. Although all of these examples illustrate potentially beneficial applications for future human missions, the Rodriguez Well should not be considered a “one size fits all applications” solution. Even the generous water use estimated for future human Mars missions in Section 2 is at the small end of the range of wells described in these examples. The Rodriguez Well has been shown to be quite effective for generating significant quantities of water and for being sustainable over long periods of time. But even in terrestrial applications, it is not universally advantageous – an assessment of alternative means for producing water at the relatively small Summit Station on Greenland found that the Rodriguez Well was not the best among them [\[35\]](#). With the ice deposits found there, the Rodriguez Well is a very useful approach to generating water in the Martian environment, but it is only one tool in a toolbox of technologies that should be considered.

**Table 4.1. Rodwell Key Characteristics**

Location	Years of Operation	Number of Personnel	Production Rate	Total Production	Notes
Camp Fistclench (Greenland)	1959 [30]	N/A (experimental well)	No Data	No Data	Experimental well
Camp Century (Greenland)	Camp: 1959 - 1967 Well #1: Oct 1960 - May 1962 Well #2: May 1962 - 1965	85-200 [34]	Avg. 230,000 gal/month [30]	Well #1: 3,500,000 gal [30] Well #2: over 5,000,000 gal [30]	Well #2 production is through Sep 1964. The well operated for approximately one more year
Camp Tuto (Under Ice Camp) (Greenland)	Feb - Jun 1962 [31]	25 [31]	(Various)	167,000 gal [31]	Camp used for 15 week test period
South Pole Station (Antarctica)	Dec 1972 - Mar 1973 [9]	N/A (experimental well)	(Various)	106,000 gal (400 tons) [9]	Experimental well
South Pole Station (Antarctica)	1993 - present	28 Winter, 140 Summer [35]	530,000 gal/yr (2,005 tons/yr) [35]	Ongoing	Currently using 3rd Rodwell
IceCube Neutrino Observatory (Antarctica)	2004 - 2010 [33]	N/A	25,100 gal/hole (94.8 tons/hole) [33]	2,160,000 gal (8,200 tons)	86 holes [33]

## 5.0 CRREL COMPUTER SIMULATION

CRREL developed its Rodwell computer simulation to design water wells for research stations on terrestrial ice caps, initially for South Pole Station, Antarctica [9] and subsequently for Summit Station, Greenland [35]. The time-domain simulation mimics the principal mass and energy exchanges through the cycle of water production and consumption for a Rodwell: a supply line from the station injects warm water into the ice, which melts ice to form a subsurface pool; a pump submerged in the pool pumps a portion of the melt water through a return line to the station; the station consumes some of this water for drinking, cooking and washing; waste heat from the station's generators reheats the remaining water to re-inject into the pool to melt new ice and thereby maintain the well. During operation, the pool grows larger and descends slowly into the ice cap, leaving a large air cavity above it. An ice cover generally forms on the pool surface, which decreases the pool-surface heat losses to the cavity. Eventually, pumping requirements from the deepening pool increase to the point that it is more efficient to start a new well nearby than to continue using the original one.

A simple lumped-mass energy budget forms the core of the simulation's calculations. Input parameters include ice density and far-field temperature, atmospheric temperature, injected water temperature and flow rate, water withdrawal rate, and station water-consumption rate. The energy budget solves for the water-production (ice-melt) rate by determining the net energy available each time step after accounting for losses to the environment (see Fig. 5.1). The simulation allows the user to set startup conditions to establish the well (initial borehole size, low input heat, no water withdrawal). Once the well reaches the target pool size, the simulation switches to user-established water-injection, -withdrawal and -consumption parameters appropriate for summer (high) or winter (low) station populations. The available waste heat links injected water temperature and flow rate, which may be separately adjusted. Typically, the user seeks to ensure that a combination of water-injection, -withdrawal and -consumption rates provide a usable lifespan (typically 10 years). Through manual iteration, the user can seek to optimize the design to minimize power requirements or maximize life.

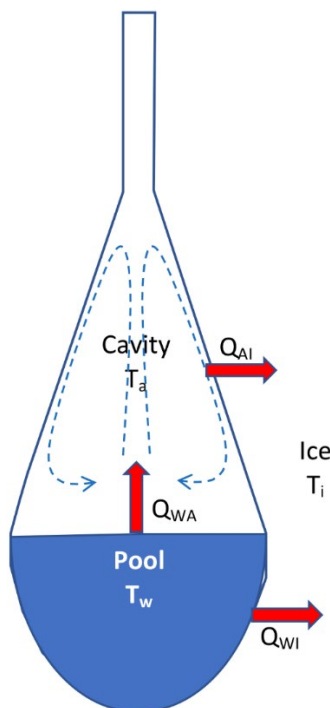


Figure 5.1. Schematic of Rodwell showing heat flows to the environment

In Figure 5.1,  $Q_{wi}$  from the water pool to the surrounding ice;  $Q_{wa}$  from the water surface into the air cavity;  $Q_{ai}$  from the cavity to the ice. The CRREL simulation solves for the environmental heat flows and the corresponding pool and cavity temperatures,  $T_w$  and  $T_a$ , respectively, for specified mass and heat flows of injected warm water from the station and extracted water pumped to the station. The injected warm water causes the pool to melt ice as it slowly descends and widens.

## 5.1 CHANGES NEEDED FOR MARS APPLICATIONS

We may cautiously adjust many of the parameters in the CRREL Rodwell simulation from terrestrial values to ones appropriate for Mars without violating physical principles upon which the simulation relies. Examples include the bulk or far-field ice temperature and density. The CRREL simulation uses measured density-depth and temperature-depth data from Antarctica or Greenland, including data that identify the depth at which water begins to pool rather than percolate through the firn. For preliminary analyses, we may assume that ancient water-ice deposits on Mars consist of fully compacted solid ice (density  $917 \text{ kg/m}^3$ ) without an overburden of porous snow or firn. Furthermore, the temperature of ice sheets a few meters below the surface approximates the local average-annual surface temperature. Surface-temperature measurements or model predictions are generally available for regions on Mars with ice deposits. Thermal conductivity, diffusivity and latent heat of solid water-ice, which the simulation also uses, remain unchanged.

However, the simulation's three heat-transfer coefficients that account for environmental heat losses (Fig. 5.1) warrant attention because the physical processes upon which they are based could be substantially different on Mars. We discuss each here briefly.

The water-to-ice heat-transfer coefficient,  $h_{wi}$  ( $\text{W/m}^2/\text{°C}$ ), establishes the heat delivered to the ice surface that bounds the water pool,  $Q_{wi}$  (W):

$$Q_{wi} = h_{wi} A_{wi} (T_w - T_m) \quad (5.1)$$

where  $A_{wi}$  is the surface area,  $T_w$  is the bulk pool water temperature and  $T_m$  is the melting temperature of ice,  $0^\circ\text{C}$ . Some of this heat conducts into the ice as an environmental heat loss and the remainder melts the ice to produce water. Lunardini and Rand employed an approximation to account for the heat loss that lumped it into an effective latent heat value [9, 41]. For the heat transfer coefficient, Lunardini and Rand (1995) [9] used a range of  $h_{wi} = 136 - 185 \text{ W/m}^2/\text{°C}$  based on published values for water flowing over ice at low velocities (laminar flow). We view this approach as reasonable for preliminary engineering calculations given that the water-ice interface should be similar for a Mars Rodwell. Numerical simulations can assess the sensitivity of predicted Rodwell performance on this parameter. Future detailed studies should investigate whether higher circulation velocities in smaller pools (just a few meters in diameter) could substantially increase  $h_{wi}$  for Mars applications. These detailed studies could also assess the validity of lumping heat-conduction losses into an effective latent-heat value.

The water-to-air heat-transfer coefficient,  $h_{wa}$  ( $\text{W/m}^2/\text{°C}$ ), determines the heat delivered to the cavity from the water-pool surface,  $Q_{wa}$  (W):

$$Q_{wa} = h_{wa} A_{wa} (T_w - T_a) \quad (5.2)$$

where  $A_{wa}$  is the pool surface area and  $T_a$  is bulk cavity (air) temperature. Natural convection, driven by warm, moist air rising from the pool and cooling as it descends along the cavity walls, governs this heat transfer. Lunardini and Rand used  $h_{wa} = 5.7 \text{ W/m}^2/\text{°C}$  [9]. Although they do not cite a source for this value, it falls within the range expected for turbulent, natural-convection heat transfer over a flat plate [40].

The conditions on Mars that affect this flow are substantially different from those on Earth: lower gravity to propel the buoyancy-driven flow; CO<sub>2</sub> rather than air as the principal gas; pressure close to the triple point of water, 6.1 mbar. The low pressure, in particular, will enhance evaporation from the pool into the cavity, potentially increasing the heat-transfer rate significantly. After an ice cover forms on the pool, sublimation of the ice owing to low pressure could increase heat transfer compared with comparable conditions on Earth. We chose to investigate these sources of potentially higher heat losses through small-scale tests described in this report.

The air-to-ice heat-transfer coefficient,  $h_{ai}$  (W/m<sup>2</sup>/°C), determines the heat removed from the cavity along the cavity walls,  $Q_{AI}$  (W):

$$Q_{AI} = h_{ai}A_{ai}(T_a - T_s) \quad (5.3)$$

where  $A_{ai}$  is the cavity surface area and  $T_s$  is temperature of the ice along the cavity walls. As with the pool temperature, Lunardini and Rand (1995) modeled the cavity air and wall temperatures as bulk values (i.e., the values could change in time but had no spatial distribution). They modeled the heat conduction from the cavity walls into the surrounding ice based on an approximation by Lunardini (1986), and they set  $h_{ai} = 5.7$  W/m<sup>2</sup>/°C, again without referencing it. Again, this value falls within the range expected for turbulent, natural-convection heat transfer over a flat plate [\[40\]](#).

As noted, the natural-convection flow in the cavity could differ substantially on Mars. If evaporation from the pool is greater than in terrestrial Rodwells, condensation and freezing of water vapor along the walls could increase heat transfer rates and hence heat losses to the surrounding ice. To assess this possibility, at least preliminarily, we included measurements of heat flux along the chamber walls as part of the small-scale tests described in this report.

## **6.0 BELL JAR EXPERIMENT**

### **6.1 EXPERIMENT DESIGN/DESCRIPTION**

We sought to apply CRREL's model to design water wells for use on Mars and thereby assess the benefits and costs of this source of water for human stations. Many model parameters are straightforward to adjust. For example, basic fluid properties (e.g., viscosity, conductivity, diffusivity, etc.) are available from handbooks. Similarly, far-field ice and air temperatures are simple input parameters. Bulk ice temperatures a few meters below the surface will equal the local average-annual surface temperatures at the sites of interest, say  $-60^{\circ}\text{C}$  to  $-80^{\circ}\text{C}$  on Mars. This range is somewhat colder than Polar ice caps on Earth, but that difference alone does not change heat-transfer regimes.

Mars' atmosphere, however, consists of  $\text{CO}_2$  at pressures close to the triple point of water (6.11 mbar,  $0.01^{\circ}\text{C}$ ). We were thus concerned that evaporative heat losses from the pool surface would be significantly greater than those for terrestrial water wells and could dominate heat losses until the pool skimmed over with ice. We therefore sought to update the pool-to-cavity heat losses for a range of conditions slightly above the triple point, 8 – 10 mbar, assuming that the well would be created at an elevation where the ambient pressure would be at least this high or that it would be possible to pressurize the cavity slightly. To a lesser degree, we also wanted preliminarily to assess whether boiling would be difficult to control. The pool-surface temperature would need to remain below  $2^{\circ}\text{C}$  to avoid boiling at 8 mbar. We chose small-scale physical tests to obtain the desired information.

Note that we judged the water-to-ice heat transfer processes (melting of, and heat conduction into, the ice walls) to be similar on Earth and Mars, assuming that the massive ice deposits on Mars are essentially water ice. We also judged that the heat loss from the water surface to the cavity would be the rate-limiting process governing cavity temperature. The associated heat loss from the cavity to the ice walls should be much faster, owing to condensation/freezing of the transported water vapor onto the walls. Nevertheless, we designed the small-scale tests to measure the cavity-to-wall heat transfer rates to compare with CRREL-model default values.

#### **Theoretical Foundation – Scaling Analysis**

Use of small-scale model tests under laboratory conditions to predict system behavior at full-scale or "prototype" conditions generally involves scaling analysis. The input variables that govern the key physical process are linked to the desired output variables through groups of dimensionless parameters. The appropriate dimensionless groups can derive from the governing equations, if these are well established, or from dimensional analysis if the equations are poorly known or complex. Provided the same physical processes govern both the model and prototype systems, the test-derived empirical relationships between the input and output dimensionless variables should hold true across all ranges of physical parameters, including fluid type, temperature and pressure ranges, gravity differences, etc.

The water-surface heat flux into the cavity consists of two main components: evaporation and convection. Evaporation heat flux derives from the mass flux of water vapor into the cavity owing to the vapor-concentration gradient and the latent heat needed to support that mass flux. Convection heat flux derives from the temperature gradient and flow over the pool surface. Natural convection within the enclosed cavity drives the flow field that governs both heat fluxes: warm, moist  $\text{CO}_2$  rises from the pool surface and then cools and condenses/freezes water vapor onto the cavity ice walls as it descends.

Ingersoll [42] and Hecht [10] derived expressions for evaporation-driven heat flux from water surfaces on Mars based on analogies with published correlations of natural convection-driven heat flux from flat plates. The two expressions differ slightly, but both include the dimensionless Grashof number to characterize the strength of the buoyancy-driven flow field.

Bower and Saylor [43] conducted an experimental investigation into the evaporative mass flux generated by natural convection over a water surface and compared their results with the few previous experimental studies on the topic. They formulated their study to seek the correlation between dimensionless flow-field input parameters and dimensionless mass flux. This same correlation should, in principle, apply to Mars, and we used it to guide our experiment design. In Section 7, we compare our results with Bower and Saylor's correlation and those of other published studies, including Ingersoll and Hecht [42, 10].

Figure 6.1 shows a schematic identifying the layout and variables relevant to the prototype and model water-well systems. In the scaling analysis presented, we include the SI units for each physical parameter.

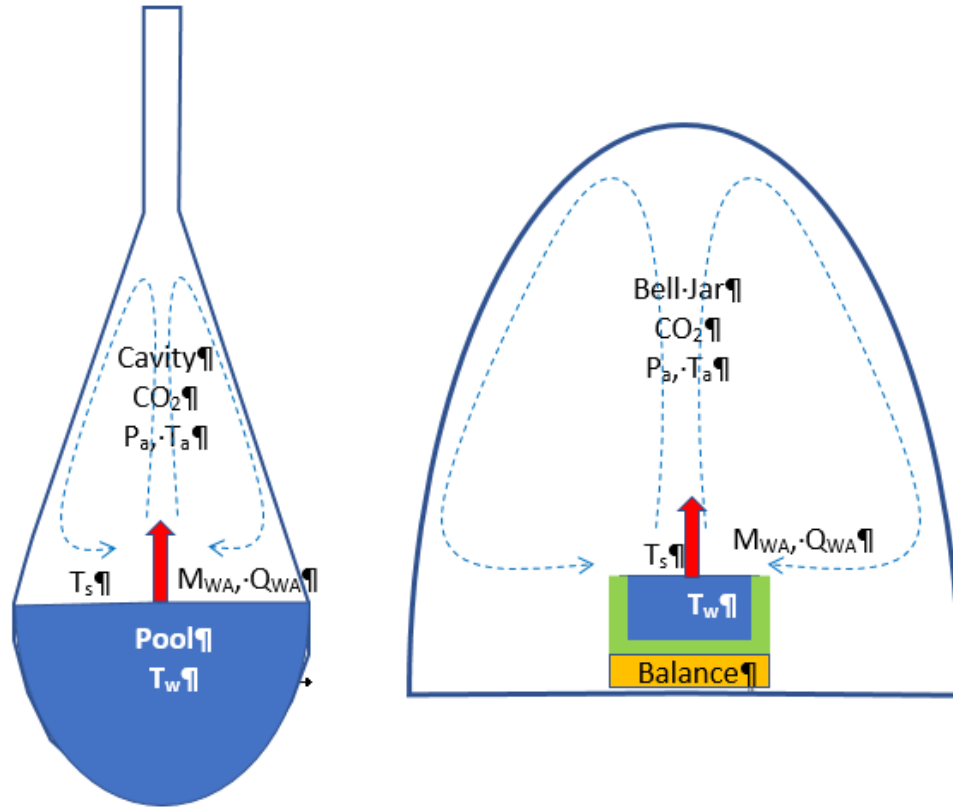


**Figure 6.1. Rodwell prototype (left) and small-scale model (right) showing key parameters and conceptual test layout (sketches not to scale)**

In Figure 6.1,  $M_{WA}$  and  $Q_{WA}$  are the mass and heat flows, respectively, from the water surface into the cavity or bell jar.  $T_w$ ,  $T_s$  and  $T_a$  are the pool-bulk, water-surface and far-field atmospheric temperatures, respectively, and  $P_a$  is the atmospheric pressure. The dashed lines show the general direction of natural-convection atmospheric flow. Scaling analysis indicated that  $CO_2$  was an acceptable working fluid for the tests.

Bower and Saylor sought to determine the coefficients in a dimensionless relationship of the form



$$Sh = BSc^{1/3}Ra^n \quad (6.1)$$

where the empirical coefficients  $B$  and  $n$  are determined from laboratory measurements and are assumed to apply across similarly configured prototype systems [43].

The dimensionless mass-transfer coefficient (Sherwood number) is defined as

$$Sh \equiv \frac{h_m W}{D} \quad (6.2)$$

where  $W$  (m) is the pool diameter and  $D$  (m<sup>2</sup>/s) is the diffusion coefficient (here, water vapor into CO<sub>2</sub>)

The evaporative mass flux,  $\dot{m}$  (kg/m<sup>2</sup>s), relates to the mass-transfer coefficient,  $h_m$  (m/s), via

$$\dot{m} = h_m \Delta \rho_{wv} \quad (6.3)$$

where water-vapor density difference between the surface and the ambient (cavity) is

$$\Delta \rho_{wv} = \rho_{wv,s} - \gamma \rho_{wv,a} \quad (6.4)$$

$\rho_{wv,s}$  and  $\rho_{wv,a}$  are the saturated vapor densities (kg/m<sup>3</sup>) at surface temperature  $T_s$  and ambient temperature  $T_a$ , and  $\gamma$  is the relative humidity in the ambient.

The Schmidt number,  $Sc$ , relates the velocity and concentration fields

$$Sc \equiv \frac{\nu}{D} \quad (6.5)$$

where  $\nu$  (m<sup>2</sup>/s) is kinematic viscosity of the ambient fluid (here CO<sub>2</sub>)

$$\nu = \frac{\mu}{\rho} \quad (6.6)$$

Absolute viscosity,  $\mu$ , (Pa•s or kg/ms) of CO<sub>2</sub> depends only on temperature for moderate pressures, and CO<sub>2</sub> density varies with both temperature and pressure according to the ideal-gas law. Because temperature varies throughout the flow field, it is customary to evaluate temperature-dependent fluid properties at the “film temperature” or average temperature,  $(T_s + T_a)/2$ , between the water surface and the far-field atmosphere.

The Rayleigh number,  $Ra$ , establishes the buoyancy-driven flow field:

$$Ra \equiv \frac{g \Delta \rho W^3}{\bar{\rho} \nu \alpha} \quad (6.7)$$

where  $g$  (m/s<sup>2</sup>) is gravitational acceleration and  $\alpha$  (m<sup>2</sup>/s) is thermal diffusivity

$$\alpha = \frac{k}{\rho c_p} \quad (6.8)$$

and  $k$  (W/mK) and  $c_p$  (J/kgK) are the thermal conductivity and specific heat of the fluid (CO<sub>2</sub>).

The density difference  $\Delta \rho$  (kg/m<sup>3</sup>) is

$$\Delta \rho = \rho_a - \rho_s \quad (6.9)$$

where  $\rho_a$  and  $\rho_s$  are the gas/vapor mixture densities at the ambient and surface conditions, respectively, and  $\bar{\rho}$  is the average of these mixture densities.

The Rayleigh number can also be written as  $Ra = GrPr$ , where the Grashof number contains the buoyancy terms

$$Gr \equiv \frac{g \Delta \rho W^3}{\bar{\rho} \nu^2} \quad (6.10)$$

and the Prandtl number captures the relationship between the momentum and energy boundary layers

$$Pr \equiv \frac{\nu}{\alpha} \quad (6.11)$$

The terms in Equation (6.9) must be evaluated to determine the buoyancy forces that drive the flow field. The gas/vapor mixture density in the ambient is

$$\rho_a = \rho_{CO_2,a} + \gamma \rho_{wv,a} \quad (6.12)$$

Because ambient temperatures on Mars and in the test are very low ( $-20^\circ\text{C}$  –  $-80^\circ\text{C}$ ), the saturated density of water vapor in the ambient,  $\rho_{wv,a}$ , is negligible, and  $\rho_a$  is essentially the density of  $\text{CO}_2$  at ambient  $T_a$ ,  $P_a$ .

However, the gas/vapor mixture density at the pool surface includes both components:

$$\rho_s = \rho_{CO_2,s} + \rho_{wv,s} \quad (6.13)$$

where again  $\rho_{wv,s}$  is the saturated density of water vapor at  $T_s$ . The  $\text{CO}_2$  density at the surface is evaluated at  $T_s$  and the partial pressure

$$P_{CO_2,s} = P_a - P_{wv,s} \quad (6.14)$$

and  $P_{wv,s} = P_{wv,sat}(T_s)$  is the saturation pressure of water vapor at  $T_s$ .

Using ideal-gas law, the densities for  $\text{CO}_2$  and water vapor may be written as

$$\rho_{CO_2}(T, P) = \frac{P}{189T} \quad (6.15)$$

$$\rho_{wv}(T, P) = \frac{P}{462T} \quad (6.16)$$

in units  $\rho$  ( $\text{kg/m}^3$ ) for  $P$  (Pa) and  $T$  (K).

The diffusion coefficient of water vapor into  $\text{CO}_2$  at the pool surface may be determined from standard conditions (Boynton and Brattain, 1929) [44]:

$$D(T, P) = 1.387 \times 10^{-5} \left( \frac{T_s}{273} \right)^2 \left( \frac{1013}{P_a} \right) \quad (6.17)$$

in units  $D$  ( $\text{m}^2/\text{s}$ ) for  $P_a$  (mbar) and  $T_s$  (K).

Lastly, the evaporative heat loss,  $Q_e$  (W), equals the evaporative mass loss,  $dM/dt$  (kg/s), times the enthalpy of evaporation near  $0^\circ\text{C}$ ,  $h_e = 2.5 \times 10^6$  J/kg, where

$$\frac{dM}{dt} = A \dot{m} \quad (6.18)$$

and  $A$  ( $\text{m}^2$ ) is the pool surface area. Evaporative mass flux  $\dot{m}$  is given by Equation (6.3).

### Test-Parameter Selection

We used the foregoing scaling analysis to guide the experiment design. We selected ranges for the input parameters that would characterize Rodwells on Mars, calculated the Sherwood numbers expected for the input Rayleigh numbers, selected physical properties for the model tests to overlap with those Rayleigh numbers, and then forecast the range of mass and heat-transfer rates expected in the model to select instrumentation (see Appendix B) to make the necessary measurements. We then compared the measured dimensionless mass-loss and heat-transfer rates with those of the Bower and Saylor correlation to assess whether it applies across the broader  $Ra$  range on Mars and to assess any distortion in results caused by the configuration differences between model and prototype.

Bower and Saylor found that  $B = 0.230$  and  $n = 0.321$  for  $9.6 \times 10^5 < Ra < 5.7 \times 10^8$  for lab tests on water evaporating into air, with the water pool unconfined by the walls of the test chamber [43]. Under these conditions, Equation (6.1) becomes

$$Sh = 0.230Sc^{1/3}Ra^{0.321} \quad (6.19)$$

Note that a potentially important model-to-prototype configuration difference pertains to the confining effect on the flow field by the cavity walls above the pool. The Bower and Saylor test configuration, and ours, minimized wall confinement, whereas the cavity walls above a Rodwell pool abut the water surface and geometrically confine the flow. Bower and Saylor noted that wall confinement can reduce the strength of dependence of  $Sh$  on  $Ra$  (i.e., reduce  $n$ ). We chose to delay investigating the role of wall confinement to follow-on tests that would more closely mimic a Rodwell configuration.

We set the range of parameters for Rodwells on Mars as  $-60^\circ\text{C} - -80^\circ\text{C}$ , 8 – 10 mbar, pool diameter 0.1 – 4.9 m, with the small diameter corresponding to well startup. This provided a range  $4.7 \times 10^3 < Ra < 5.7 \times 10^8$ , again with the low end corresponding to startup. Note that the range of  $Ra$  for Mars Rodwells overlaps the range of validity of Equation (6.19) for pool diameters larger than 0.5 m.

Table 6.1 summarizes the target values for the 12 model-test points. The available bell jar was 0.5-m-dia., and the internal cooling shroud could reliably achieve  $-40^\circ\text{C}$ . Working within these constraints, we were able to overlap most of the  $Ra$  range of interest using  $\text{CO}_2$  as the atmosphere, a pressure range 8 – 1000 mbar, and pool sizes of 0.08 m and 0.14 m (based on commercially available dewars of 3 and 6 inches, respectively). The actual operating conditions of the tests varied slightly from these target values but still overlapped the  $Ra$  range of interest.

**Table 6.1. Target operating conditions and Rayleigh numbers for the model tests**

Test Number	Dewar Size (inches)	Air Temp (deg C)	Air Pressure (mbar)	Rayleigh Number
1	3	-40	8	4.6E+03
2	3	-40	240	1.0E+06
3	3	-40	1000	1.7E+07
4	3	-20	8	2.5E+03
5	3	-20	370	1.0E+06
6	3	-20	1000	7.0E+06
7	6	-40	8	2.5E+04
8	6	-40	95	9.9E+05
9	6	-40	1000	9.1E+07
10	6	-20	8	1.3E+04
11	6	-20	250	2.6E+06
12	6	-20	1000	3.8E+07

*The green and red values of  $Ra$  fell within and outside, respectively, of the valid range for Equation (6.19).*

Figure 6.2 shows predicted Sherwood number versus Rayleigh number,  $Sh(Ra)$ , based on Equation (6.19), for Mars- and model-Rodwell conditions. It also shows Bower and Saylor's correlation. Note that the slight offsets of the test points and curves result from the small influence of Schmidt number,  $Sc$ , in Equation (6.19) for the atmospheric gasses ( $CO_2$  for Mars and model, air for Bower and Saylor) at the respective temperatures and pressures. The low-pressure test conditions provided a check on whether Equation (6.19) may be validly extended for  $Ra < 10^6$ .

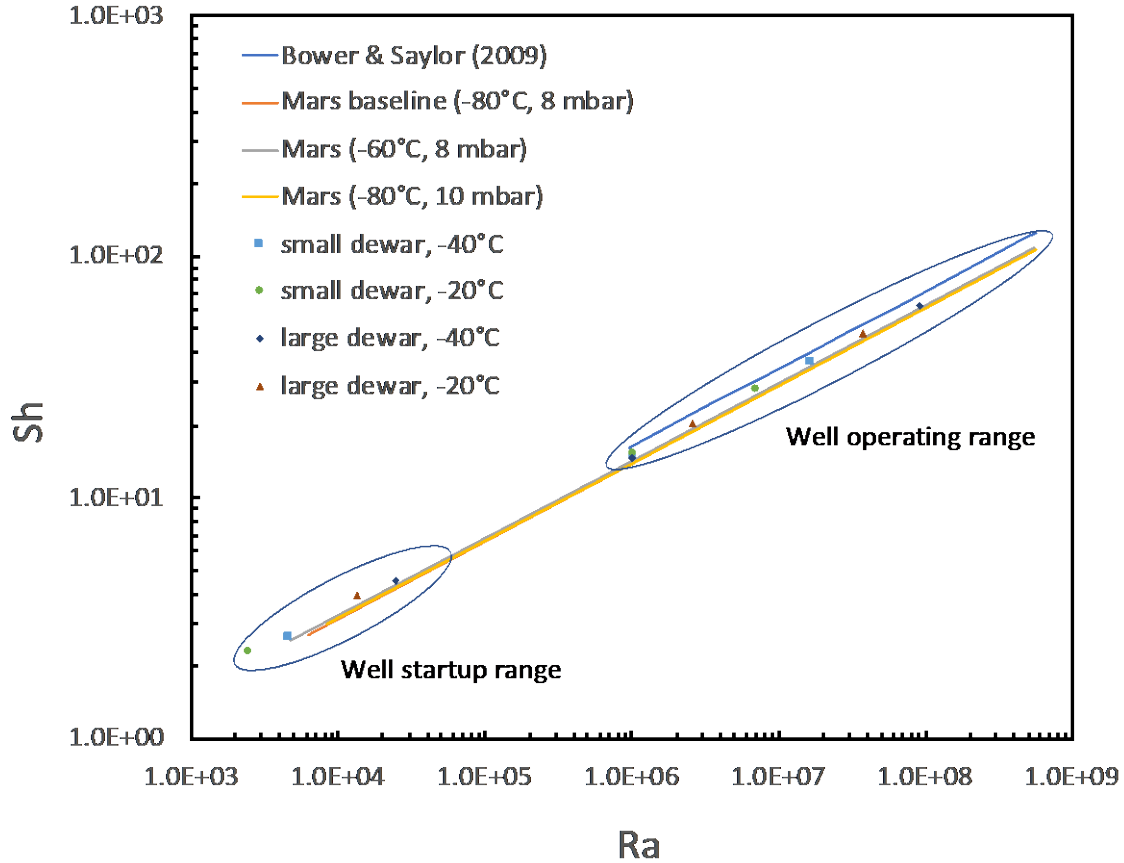


**Figure 6.2. Dimensionless mass-transport,  $Sh$ , versus dimensionless flow parameters,  $Ra$ , for evaporative mass loss from a water pool driven by natural convection above the pool. Predicted  $Sh(Ra)$  values for Mars and our small-scale tests use the Bower and Saylor correlation (Equation 6.19), with the slight separation resulting from different values of  $Sc$ .**

## 6.2 EQUIPMENT DESIGN/DESCRIPTION

Based on the rationale described in the previous section for conducting a small scale tests to obtain the data we need, a small, instrumented bell jar (officially, the Portable Bell Jar System 996) was identified at the NASA Johnson Space Center (see Figure 6.2-1) in which a suitable Martian environment could be created. Additional details for this bell jar and other equipment used for this experiment can be found in Appendix B.

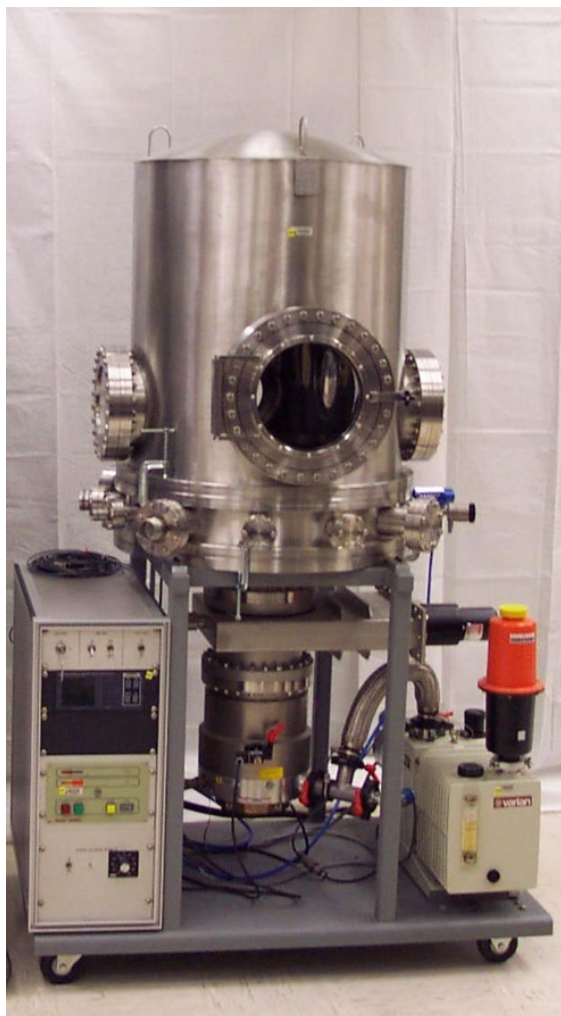


**Figure 6.3. Bell jar test facility at the NASA Johnson Space Center.**

The usable test volume in this bell jar measured approximately 2 feet in diameter and 2 feet tall (approximately 60 cm diameter by 60 cm tall). Pressure in this chamber could be held at levels typically observed on Mars. A separate thermal shroud was available, as part of the bell jar's optional equipment (see Appendix B). Although this shroud is capable of using liquid nitrogen as a coolant (and thus attaining that temperature in the bell jar), a glycol-based coolant was used to reach and maintain the low temperatures needed for this test. As seen in Figure 6.3, numerous pass-throughs of different sizes were available around the circumference of the bell jar. Automated systems were also available to lower or raise the test volume pressure at a defined rate or to hold pressure at a specified level.

Figure 6.4 shows a schematic of the test equipment used in this experiment and its general arrangement in the bell jar. The simulated Rodwell water pool was contained in a commercially available, hemispherical cryogenic dewar. This type of dewar was selected to minimize heat loss through the container itself and thus limiting the measurable heat loss to that of the water pool surface. The recirculating hot water typical of full-scale Rodwell operations was simulated with a submersible electric heater and a magnetic stirring bar.

Two key measurements for this experiment included the heat lost from the water pool and the water mass loss due to evaporation. Use of a cryogenic dewar allowed the heat loss from the water pool to be measured by equating it to the amount of power needed by the heater to maintain a constant pool temperature. Evaporative mass loss from the water pool was measured by a load cell mounted under the dewar.

Redundant resistance temperature detectors (RTDs) were mounted in the water pool to provide the feedback necessary to control power to the immersion heater. Three RTDs were mounted in the gas volume of the bell jar: one just above the surface of the water, one just below the top of the cooling shroud, and the third midway between these other two RTDs. Heat flux sensors were attached to the cooling shroud wall at the same height as the three RTDs in the gas volume. A relative humidity sensor and pressure sensor were mounted with the mid-point RTD sensor. (For the actual tests, a separate pressure sensor was not used, instead relying on the pressure sensors built into the bell jar facility.)

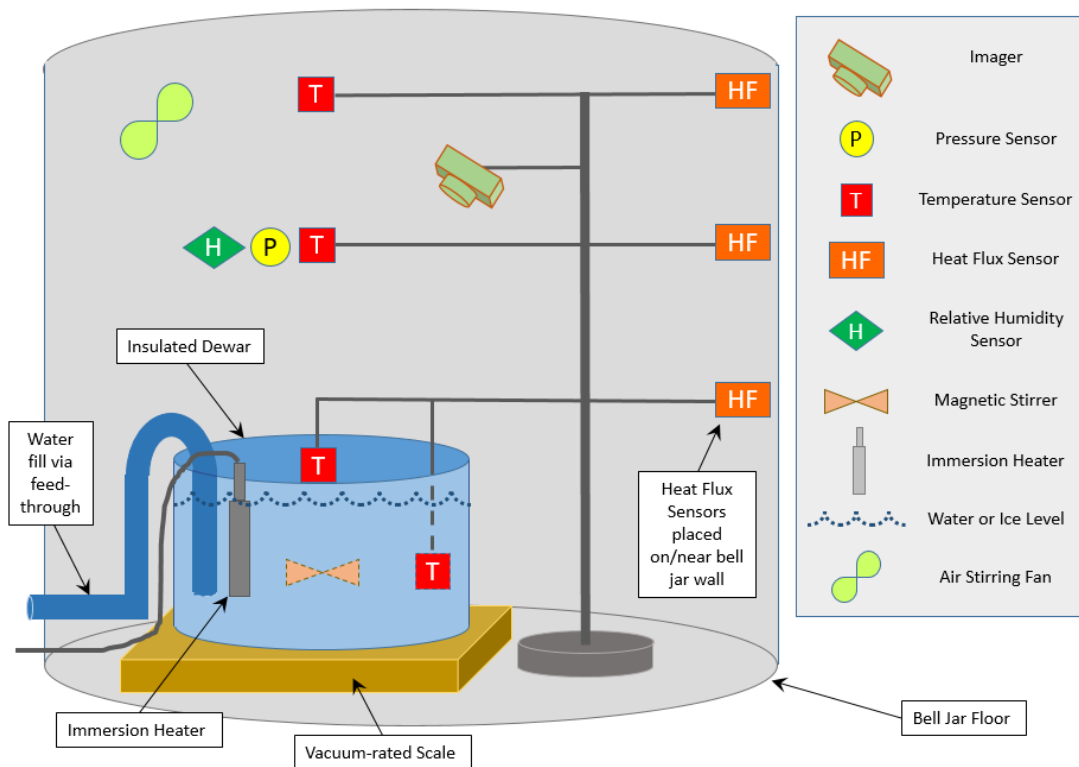


**Figure 6.4. Test equipment used inside the bell jar to gather heat transfer data relevant to Rodwell operations.**

A small stirring fan was mounted in the gas volume. This fan was used during the gas cool-down phase to enhance mixing and thus shorten the time to cool down to the temperature test point. Once the desired gas temperature had been achieved, this fan was turned off and any circulation in the gas volume was achieved by natural convection.

A small camera was placed near the top of the test chamber so that the evolution of the test could be observed. A single LED light was placed near this camera for illumination. An LED light was used to limit the heat input from this source.

When initially sealed, the bell jar is filled with 14.7 psi air at room temperature. The chamber is drawn down to vacuum and backfilled with CO<sub>2</sub> to 1000 mbar. The chamber is drawn down to vacuum a second time and backfilled with CO<sub>2</sub> to 1000 mbar. This was considered sufficient to remove non-CO<sub>2</sub> gas from the chamber. The dewar was then filled with deionized water to the desired level from an external source. (A feed-through for water was used to prevent the purge cycle from interfering with the water state/phase prior to the beginning of the test.) The remainder of the test then proceeded, beginning with the gas cool down.

All of these sensors, the camera, the stirring fan, water feed-through, and the immersion heater were mounted to a support structure independent of the dewar so that their mass and anticipated ice buildup would not be measured by the load cell.

Figure 6.5 shows all of this equipment inside the bell jar as seen from the camera. Conditions inside the bell jar were near room temperature and pressure when this image was captured.



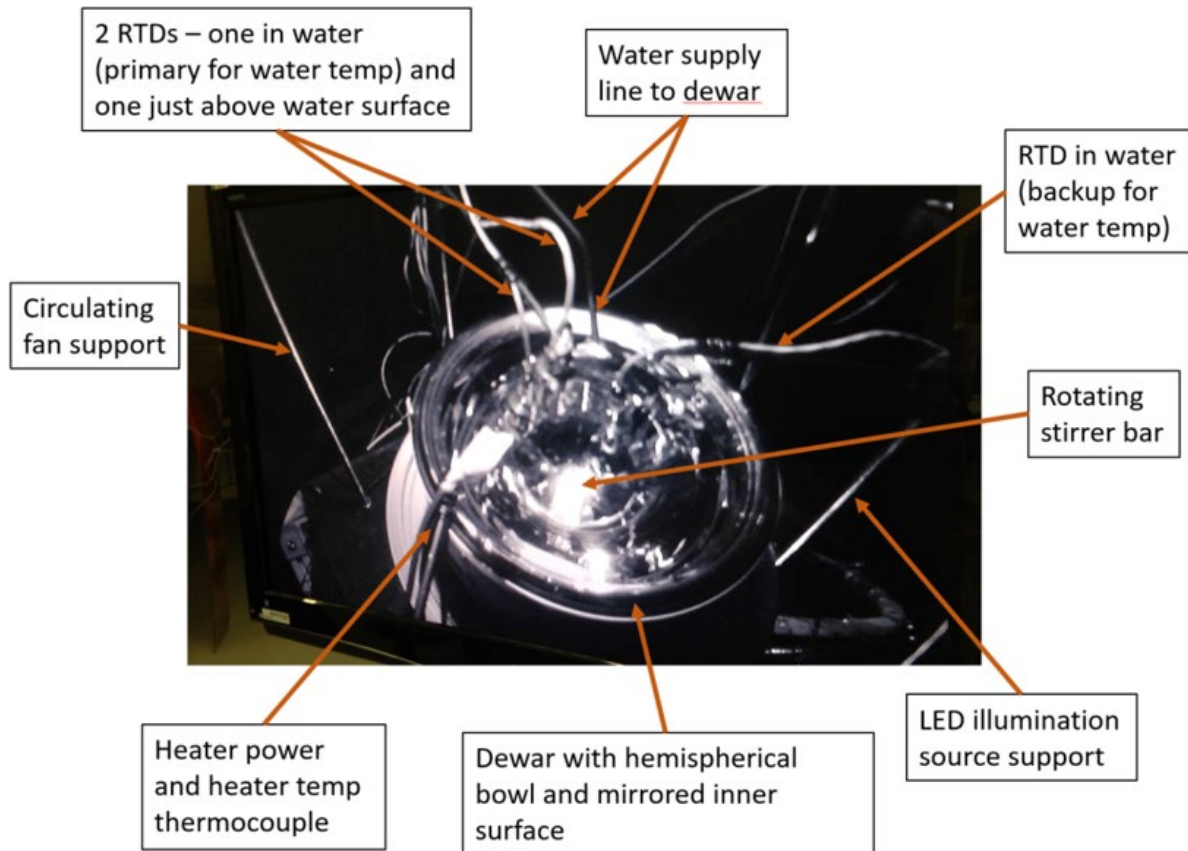


**Figure 6.5. Test equipment used inside the bell jar as seen from the internal camera.**

[Note: Although not intended to be one of the experimental investigations, the camera did provide several unexpected benefits. First, it documented that an ice shelf formed just above the water pool when operating at all of the test conditions. The CRREL engineers regularly see an ice shelf of this type in large Rodwells, but it was unclear how quickly it would form under the test conditions (see Figure 6.6). Assuming that the ice shelf significantly reduces mass and heat transfer from the pool surface, a reduction in the exposed water pool area was applied when determining the results of the tests (a 30% diameter reduction to account for the ice grown around the dewar rim at the pool surface). Second, the camera showed that water evaporating from the pool quickly froze on structures suspended above the pool and very little if any froze on the thermal shroud. This observation is problematic for those water extraction concepts that assume ice can be melted below the surface and the water vapor extracted from the cavity, so that condensation methods can be used to capture the water above the surface. These observations indicate that the water vapor will quickly freeze to the subsurface cavity wall or any suspended equipment hanging in the cavity.]

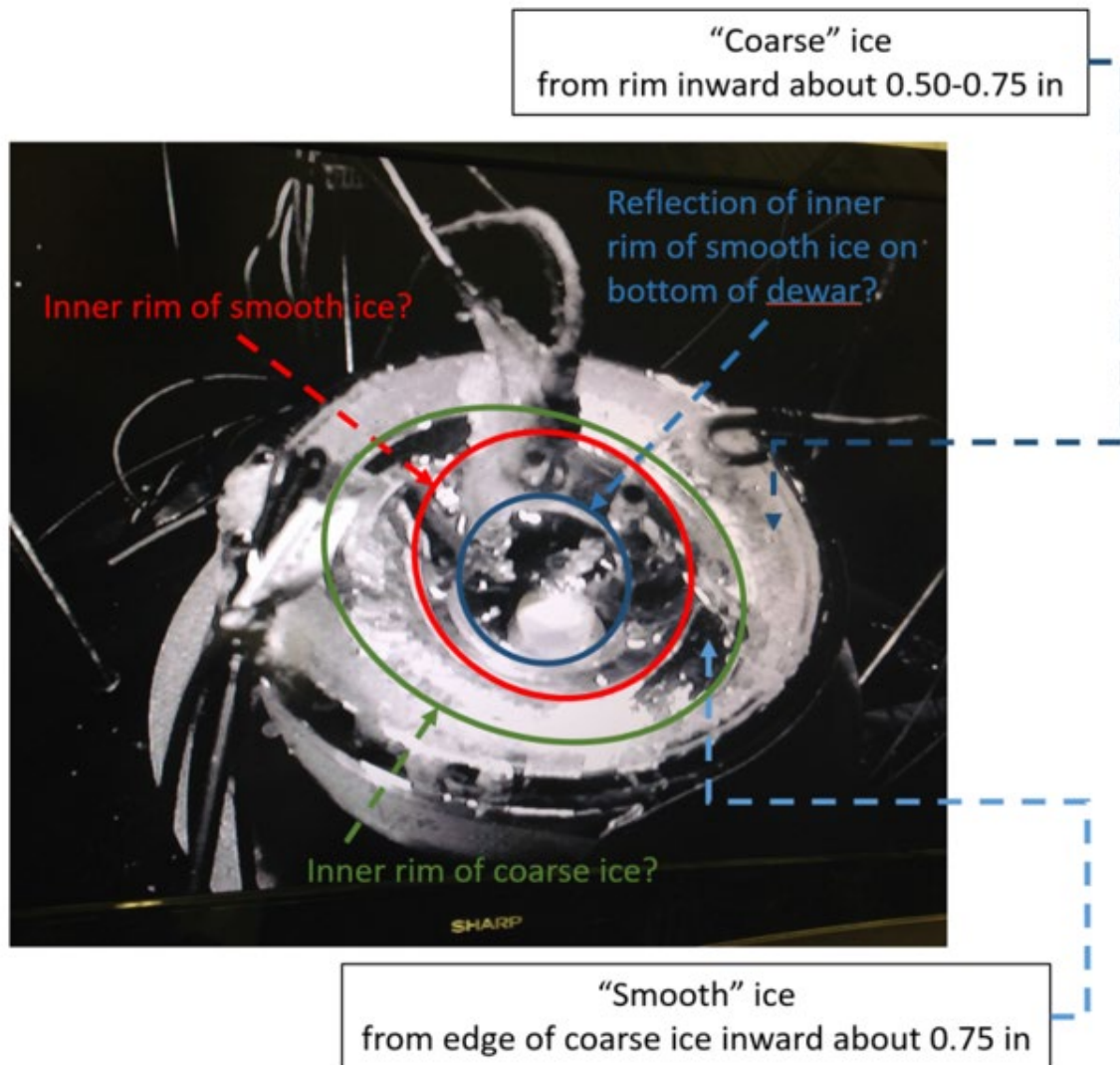


**Figure 6.6. View of test equipment inside bell jar during at test conditions (6 mbar pressure, -40°C temperature. This view shows the ice shelf that formed just above the water pool.**

Finally, the average cooling-shroud wall temperature (the average of the three heat flux sensor outputs) was used for the far-field atmospheric temperature,  $T_a$  (the “Air Temp” target value in table 6.1), because the temperature difference between the wall and the pool drove the natural-convection flow.

Figure 6.7 shows a more detailed view of how the central hardware items of this experiment are assembled inside of the test volume.



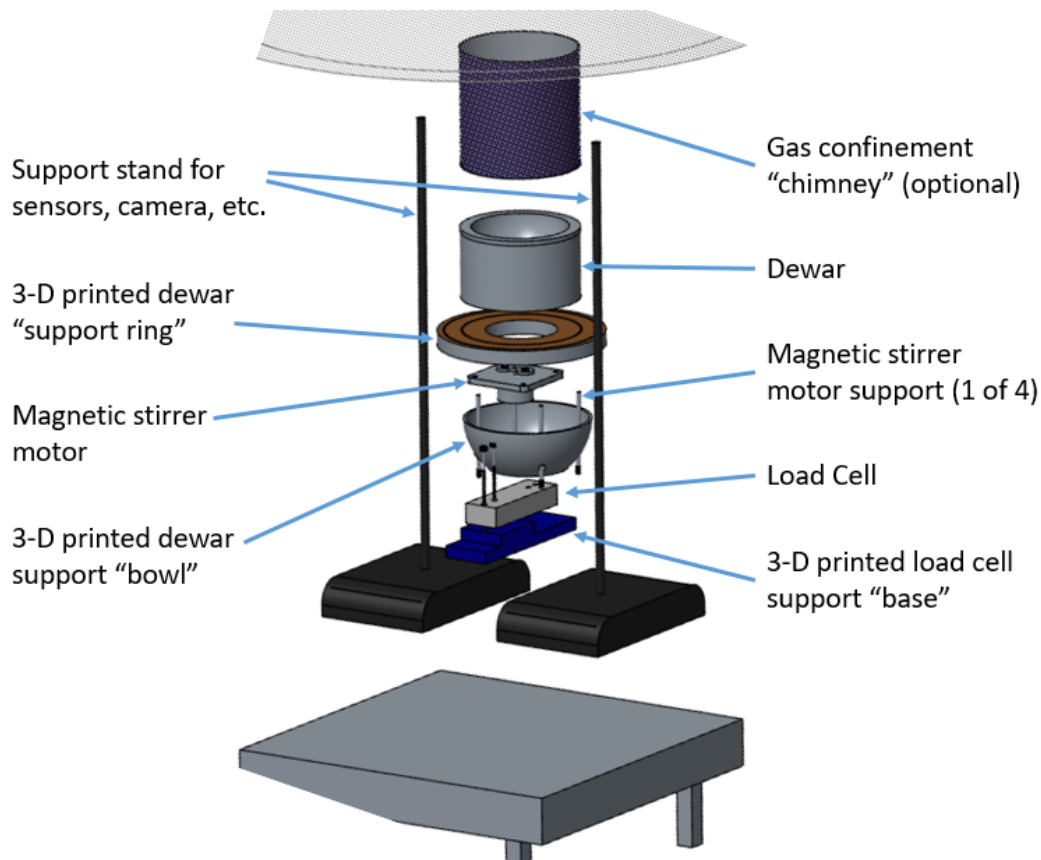


**Figure 6.7. An expanded view of experiment equipment as assembled in the test volume.**

A custom-designed set of three structural elements (the “base,” the “bowl,” and the “support ring”) were used to hold the load cell and dewar in position. These three elements were 3-D printed using ULTEM® material in an “open” / porous form to reduce both weight and cool down time (by providing pathways for gas to circulate through the structure). The “bowl” portion of this structure was introduced as a space into which the stirrer motor could be placed in close proximity to the dewar. However, this stirrer motor was held in position with four vertical supports not physically connected to the base/bowl/support ring structure. This arrangement helped minimize the introduction of any vibrations into the load cell signal.

A “gas confinement chimney” was designed to more closely simulate the effect of wall confinement on natural-convection flow above the pool, as found in terrestrial Rodwells and thought to be likely in the Mars Rodwells. Use of this chimney would have been part of an additional series of tests for comparison with the data obtained from an “open” configuration. There was insufficient time for these additional “confined” tests in the results reported here, but they remain a desired component of future tests.

### 6.3 PROCEDURE

These tests were carried out in the Energy Systems Test Area (ESTA) at the NASA Johnson Space Center. Standard ESTA processes were followed to develop and document test procedures for this experiment. These processes resulted in the following applicable documents:

ESTA-T-8I048	Test Procedure: Rodwell Subsurface Water Extraction for Mars ISRU Test
ESTA-TP-8I048	Test Plan: Rodwell Subsurface Water Extraction for Mars ISRU Test
ESTA-HA-8I048	Test Hazard Analysis: Rodwell Subsurface Water Extraction for Mars ISRU Test
ESTA-OP-361-01501	Operating Procedure for Portable Bell Jar System 996
ESTA-HA-361-01502	Hazard Analysis of Portable Bell Jar System 996
EP-WI-004	ESTA General Operating Procedures Manual
ESTA-IHA-353-01186	Integrated HA for Resource Conversion Test Facility

A Test Readiness Review (TRR) was held in July 2019 followed by tests in September and October of 2019.

Detailed bench procedures for startup, test operations, and shut down can be found in ESTA-T-8I048 "Test Procedure: Rodwell Subsurface Water Extraction for Mars ISRU Test." Because of the time typically required for cool down and establishing a stable environment in the bell jar, one test point was run in one day. A simplified bench procedure for this test is as follows:

- Before sealing bell jar, check operation of all sensors, load cell, stirrer motor, immersion heater, and water fill plumbing.
- Seal bell jar and start sensor data collection.
- Pump down bell jar to vacuum and backfill with CO<sub>2</sub> to 1000 mbar; repeat. (Note: gas at room temperature.)
- Fill dewar with deionized water from an external source using the pass through; note mass.
- Turn on gas stirring fan and begin lowering gas temperature.
- Lower gas pressure in stages (number of steps and magnitude of pressure drop is different for each test point) monitoring for out gassing or boiling.
- As water temperature in the dewar approaches freezing, turn on stirring bar and immersion heater; monitor water temperature as gas temperature drops below freezing to ensure water in the dewar holds at the desired level ( +1° or +2° C).
- When chamber pressure and temperature reach test point conditions, allow time for all components to reach a steady state conditions.
- Operate for a sufficient amount of time at these conditions for useful data to be gathered.
- Allow temperature and pressure to return to room temperature conditions before unsealing bell jar.

Test results based on this equipment and these procedures are described in the next section.

## 7.0 EXPERIMENT RESULTS

### 7.1 DATA REDUCTION PROCESS

We conducted 12 model tests during September – October 2019, with the sequence and target conditions listed in Table 6.1. Table 7.1 summarizes the test results. Note that the internal diameters of the 3-inch and 6-inch dewars measured 0.114 m and 0.149 m, respectively, and we applied a 30% diameter reduction to account for the ice grown around the dewar rim at the pool surface. Also, we used the average cooling-shroud wall temperature for the far-field atmospheric temperature,  $T_a$ , because the temperature difference between the wall and the pool drove the natural-convection flow.

Our planned test procedure was to cool the bell jar to the target temperature, pump down the CO<sub>2</sub> atmosphere to the target pressure, establish that conditions were steady, and then acquire the desired steady-state evaporative mass loss, heater power, and wall heat fluxes. Shakedown tests allowed us to correct several minor problems: we paused CO<sub>2</sub> pump-down when bubbles formed in the pool to allow time for dissolved gasses to out-gas; we adjusted the heater controller to apply power smoothly and thereby avoid the local boiling on the surface of the cartridge heater; we lengthened wait times at each test point to achieve steady state conditions more reliably; we tracked load-cell temperature to ensure that its readings were not drifting owing to changing temperature. Shakedown tests also allowed us to calibrate load-cell zero offset and scale factor as functions of temperature.

Unfortunately, we encountered several problems during the first six tests using the small dewar. First, we noted a significant, but apparently randomly occurring, problem with drift in the steady-state load-cell data (this was later traced to a faulty power supply). Subsequent quality checks revealed that the mass-loss measurements were physically unrealistic for three tests (mass gain measured or evaporative power greater than heater power). Furthermore, the chamber pressure stabilized below the triple point pressure (6.1 mbar) for two other tests; boiling resulted, so the data were unusable to determine evaporative mass losses. Only one small-dewar test (Test 5) passed our quality review, and its results may be unreliable because we did not fix the load-cell signal drift until after the small-dewar tests. We retained the Test 5 data but assessed the  $Sh(Ra)$  correlation with and without including it.

During the scheduled downtime to swap dewars, we were able to trace the drift in the load-cell data to a poorly functioning power supply and swapped it out. We also fine-tuned pump-down of the chamber for the low-pressure test points. Subsequently, all six large-dewar tests (Tests 7 – 12) passed our quality checks. We also slightly increased the stirring rate and temperature set-point of the pool water to limit ice formation on the inner rim of the dewar.

Figure 7.1 provides examples of full-test data for Test 5 and Test 11, which both passed quality review. We determined evaporative mass loss,  $dM/dt$ , from the best-fit slope through the load-cell mass measurements during the selected steady state periods. We estimate the uncertainty in  $dM/dt$  as  $\pm 20\%$ , which dominates uncertainty in the calculated  $Sh$  ( $\pm 20\%$ ).

**Table 7.1. Test Data Summary**

C

Test No.	1	2	3	4	5	6	7	8	9	10	11	12
Ta (°C)	-28.4	-28.1	-28.8	-43.5	-44.9	-50	-24.6	-27.1	-26.0	-40.9	-45.3	-45.8
Ts (°C)	0	0.96	0	0	0.74	0	2.09	2.04	1.90	2.00	2.06	1.54
Pa (mbar)	1005	340	3.2	999	213	2.9	1003	245	574	791	85.5	8.0
W (m)	0.080	0.080	0.080	0.080	0.080	0.080	0.104	0.104	0.104	0.104	0.104	0.104
Ra	1.1E+07	1.3E+06	2.0E+03	1.9E+07	9.7E+05	2.8E+03	2.1E+07	1.6E+06	7.6E+06	2.5E+07	4.1E+05	1.2E+04
Quality	poor	poor	poor	poor	good	poor	good	good	good	good	good	good
dM/dt (kg/s)					2.7E-07		1.8E-07	3.2E-07	8.8E-07	4.2E-07	8.2E-07	2.2E-06
Sh					1.3E+01		3.0E+01	1.3E+01	8.5E+01	5.2E+01	1.1E+01	2.9E+00
Sc					0.42		0.46	0.46	0.46	0.43	0.42	0.43
Qt (W)					4.95		7.02	6.52	7.53	10.23	9.77	13.72
Qe (W)					0.67		0.44	0.81	2.20	1.05	2.04	5.63
Qc (W)					4.28		6.57	5.71	5.33	9.17	7.73	8.10
Nu_c					1.0E+02		2.0E+02	1.6E+02	1.5E+02	1.8E+02	1.4E+02	1.4E+02
Nu_t					1.2E+02		2.1E+02	1.8E+02	2.2E+02	2.0E+02	1.7E+02	2.5E+02

Notes on data quality:

Tests 1 & 4 – Load-cell data showed mass increase during the established steady-state periods.

Tests 3 & 6 – Chamber pressure stabilized below the triple point of water (6.1 mbar).

Test 2 – Evaporative heat loss calculated from measured steady-state mass loss exceeded heater power input.

All other tests passed quality review

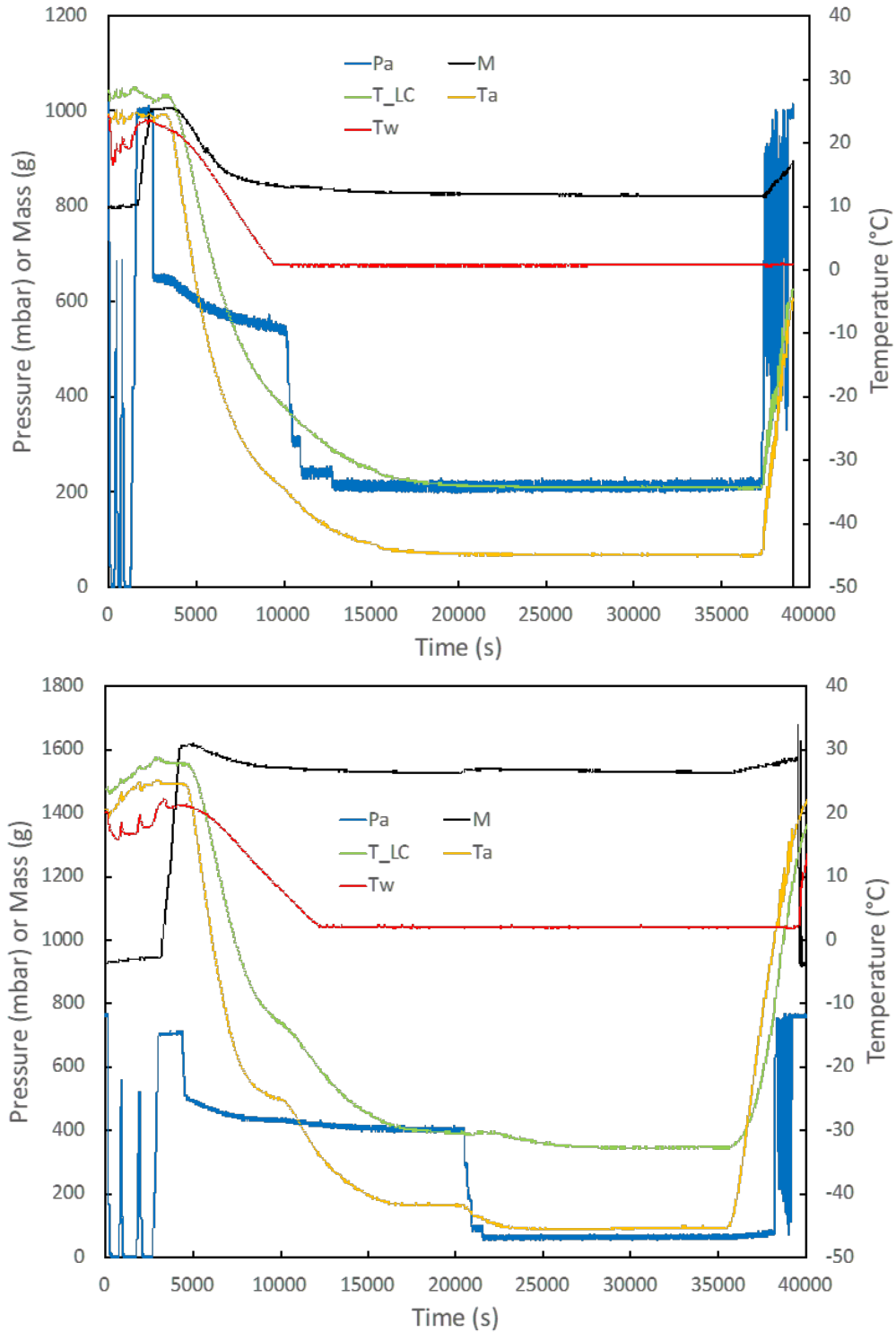


**Figure 7.1. Full-test data from Test 5 (upper) and Test 11 (lower): Atmospheric pressure (Pa), load cell mass (M), load cell temperature (T<sub>LC</sub>), atmospheric temperature (T<sub>a</sub>), and water temperature (Tw). The steady state periods were 25000 – 37000 s for Test 5 and 30000 – 35000 s for Test 11.**

## 7.2 COMPARISON WITH OTHER EXPERIMENTAL RESULTS

### Evaporative Mass Transport

Figure 7.2 shows the dimensionless evaporative mass transfer,  $Sh$ , versus  $Ra$  for all seven good-quality tests (Tests 5, 7 – 12). Test 5 has minimal influence on the correlation  $Sh(Ra)$  because it plots close to the best-fit line for the large-dewar tests (Tests 7 – 12). Test 9  $Sh(Ra)$  point plots high relative to the best-fit line in Figure 7.2. Nevertheless, the Test 9 data passed our quality review (stable pressure & temperature conditions, smooth rate of mass loss, heater power sufficient to produce the measured evaporative mass loss). It also plots well on the  $Nu(Ra)$  plot, Figure 7.3 (discussed below). We therefore included it on both plots, essentially having no justification to exclude it.

Also shown are several relevant published correlations, plotted across their valid ranges of  $Ra$ . Table 8.2 summarizes the coefficients in these power-law correlations of the form

$$Sh = C Ra^n \quad (7.1)$$

Note that we have reworked each published correlation to conform to Equation (7.1) to compare their predictions. The Bower and Saylor correlation is Equation (6.19) with the average test value of  $Sc$ , which varied little, used to collapse it to  $Sh(Ra)$  [43]. We similarly collapsed the correlations of Sharpley and Boelter from 1938 and Boelter from 1946, as modified by Bower and Saylor, for consistent parameter definitions [43, 45, 46].

Ingersoll and Hecht formulated evaporative mass-loss expressions based on analogies with published expressions for natural-convection heat transfer over flat plates [42, 10]:

$$\text{Ingersoll [42]} \quad Sh = 0.17 (Gr^*)^{1/3} \quad (7.2)$$

$$\text{Hecht [10]} \quad Sh = 0.15 (Gr^* Sc)^{1/3} \quad (7.3)$$

where  $Gr^*$  differs from Grashof number defined by Equation (6.10) through the use of the surface vapor- $CO_2$  mixture density,  $\rho_s$ , rather than the average mixture density,  $\bar{\rho}$ , in the denomination. That is,

$$Gr^* \equiv \frac{\bar{\rho}}{\rho_s} Gr \quad (7.4)$$

Cast in the form of  $Sh(Ra)$ , these expressions become:

$$\text{Ingersoll [42]} \quad Sh = 0.17 \left( \frac{\bar{\rho}}{\rho_s} \right)^{1/3} Pr^{-1/3} Ra^{1/3} \quad (7.5)$$

$$\text{Hecht [10]} \quad Sh = 0.15 \left( \frac{\bar{\rho}}{\rho_s} \right)^{1/3} Le^{1/3} Ra^{1/3} \quad (7.6)$$

where Lewis number relates thermal and molecular diffusion:

$$Le \equiv \frac{\alpha}{D} = Sc/Pr \quad (7.7)$$



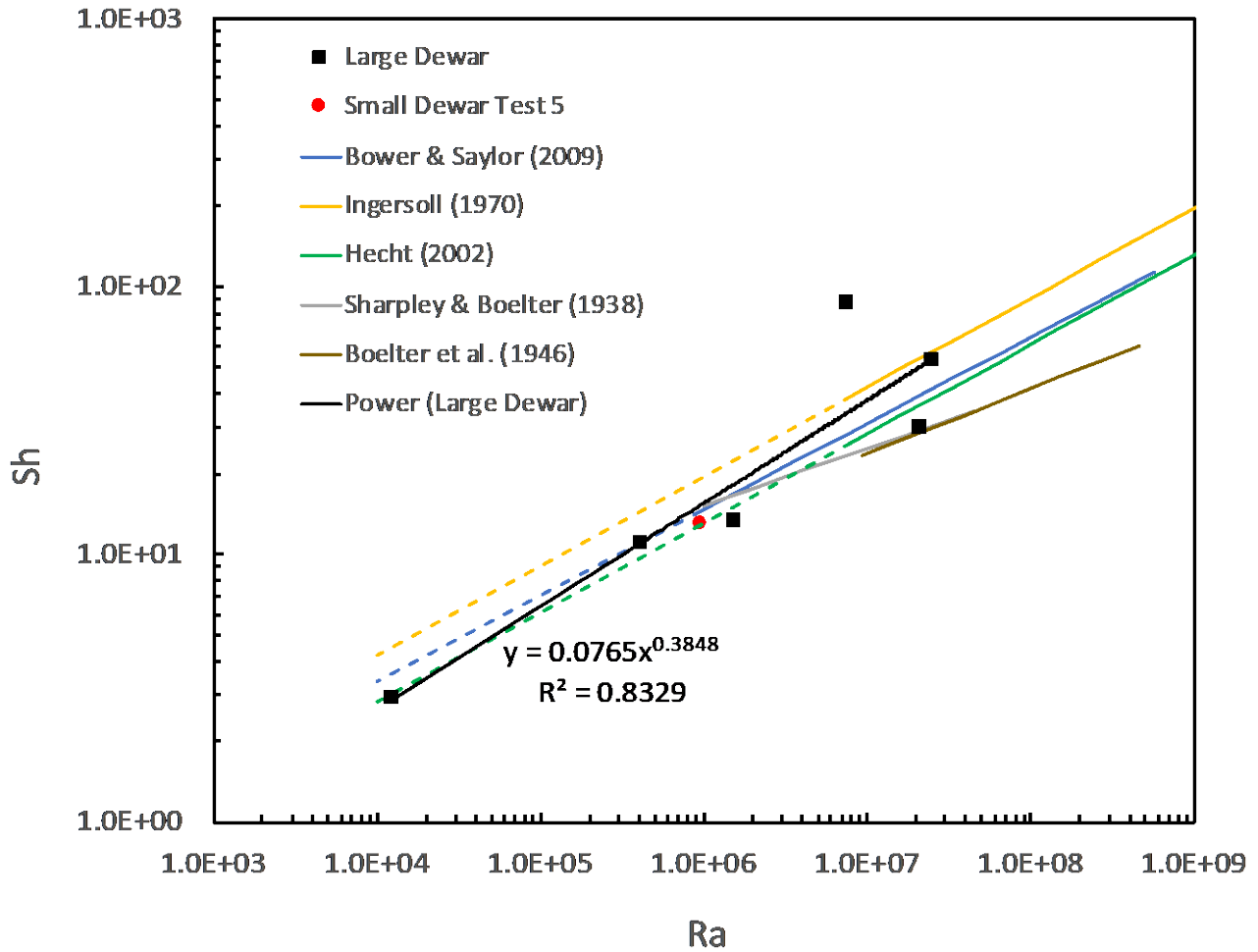


**Figure 7.2. Sherwood-Rayleigh correlation,  $Sh(Ra)$ , for test data and selected published correlations. Test 5 has little influence on the best-fit line through the large-dewar tests. The dashed lines show extensions of correlations from Bower & Saylor, Ingersoll, and Hecht below their stated ranges of  $Ra$  validity to overlap with our data [43, 42, 10]**

As seen in Figure 7.2, correlations from Bower and Saylor, Ingersoll, and Hecht, which all have  $Sh \sim Ra^{1/3}$ , all provide reasonable agreement with our test data when extended well below their stated ranges of  $Ra$  validity [43, 42, 10]. Note that the correlations of Ingersoll and Hecht derive from natural-convection heat-transfer valid in turbulent flow at much higher  $Ra$  values. The corresponding heat-transfer correlations for laminar flow have  $Ra^{1/4}$  dependence. Bower and Saylor also noted the similarity of their correlation with turbulent-flow heat-transfer despite important differences in boundary conditions and length scales [43]. Collectively, these results may suggest that natural-convection flow under combined mass and heat transfer remains turbulent at low  $Ra$  where heat transfer alone produces laminar flow. Given that well-startup conditions on Mars would occur at low  $Ra$ , we plan to investigate this regime in more detail through follow-up tests.

**Table 7.2. Parameters  $C$  and  $n$  for correlation  $Sh = C Ra^n$**

Source	$C$	$n$	Lower $Ra$	Upper $Ra$
Large dewar tests	0.0765	0.385	1.2E+04	2.5E+07
All 7 valid tests	0.0722	0.387	1.2E+04	2.5E+07
Bower & Saylor (2009)	0.175	0.321	9.6E+05	5.7E+08
Ingersoll (1970)	0.196	0.333	8.0E+06	1.0E+11
Hecht (2002)	0.131	0.333	8.0E+06	1.0E+11
Sharpley & Boelter (1938)	0.805	0.213	1.0E+06	4.5E+07
Boelter et al. (1946)	0.491	0.241	9.3E+06	4.6E+08

### Heat Loss

The total heat loss from the water surface into the cavity,  $Q_t$ , consists of two main components: evaporation,  $Q_e$ , and convection,  $Q_c$ . That is,

$$Q_t = Q_e + Q_c \quad (7.8)$$

where  $Q_e$  (W), equals the evaporative mass loss,  $dM/dt$  (kg/s), times the enthalpy of evaporation near  $0^\circ\text{C}$ ,  $h_e = 2.5 \times 10^6$  J/kg. Because heat loss through the dewar walls was likely negligible,  $Q_t$  for each test was the measured average heater power. We may thus calculate  $Q_c$  from Equation (7.8). The dimensionless parameter for convective heat flux is Nusselt number:

$$Nu_c \equiv \frac{h_c L}{k} \quad (7.9)$$

where  $h_c$  (W/m $^\circ\text{C}$ ) is the convective heat-transfer coefficient,

$$h_c = \frac{Q_c}{A (T_s - T_a)} \quad (7.10)$$

and  $L$  is a characteristic length,  $k$  is thermal conductivity of the fluid,  $A$  is the effective pool area and  $T_s - T_a$  is the driving temperature difference from the pool surface to the far-field atmosphere.

There are well-established correlations of  $Nu_c(Ra)$  for natural-convection heat transfer over heated surfaces, and we follow the formulation presented by Holman

$$Nu_c = c (Ra^*)^m \quad (7.11)$$

where  $c$  and  $m$  are empirical coefficients and  $Ra^*$  is defined as per Equation (6.7) for  $Ra$  except that Holman defines  $W^* = 0.9W = L$  as the characteristic length for a horizontal circular plate [40]. Thus  $Ra^* = (0.9)^3 Ra$ . As with the Bower and Saylor mass-transfer correlations, Holman's heat-transfer correlations use fluid properties evaluated at the film temperature [43]. Holman presents separate expressions for laminar and turbulent natural-convection regimes [40]:

$$\text{laminar} \quad Nu_c = 0.54 (Ra^*)^{1/4} \quad 2 \times 10^4 < Ra^* < 8 \times 10^6 \quad (7.12)$$

$$\text{turbulent} \quad Nu_c = 0.15 (Ra^*)^{1/3} \quad 8 \times 10^6 < Ra^* < 10^{11} \quad (7.12a)$$

Table 7.1 includes the measured values of  $Q_t$ ,  $Q_e$  and  $Q_c$  for the model tests and the resulting values of  $Nu_c$ . It also includes values for  $Nu_t$ , which uses the total heat loss rather than the just convective portion in Equations (7.9 – 7.10).

Figure 7.3 shows the resulting  $Nu(Ra)$  for convective and total heat losses from the pool measured during the model tests. It also shows Holman's correlations for horizontal circular plates (Equations 7.12). Two key differences are apparent: the model-based  $Nu$  values are considerably higher than those for horizontal plates, and they are nearly independent of  $Ra$ . As for  $Sh(Ra)$  test results, including the small-dewar Test 5 value does not appreciably change the best-fit  $Nu(Ra)$  correlations.

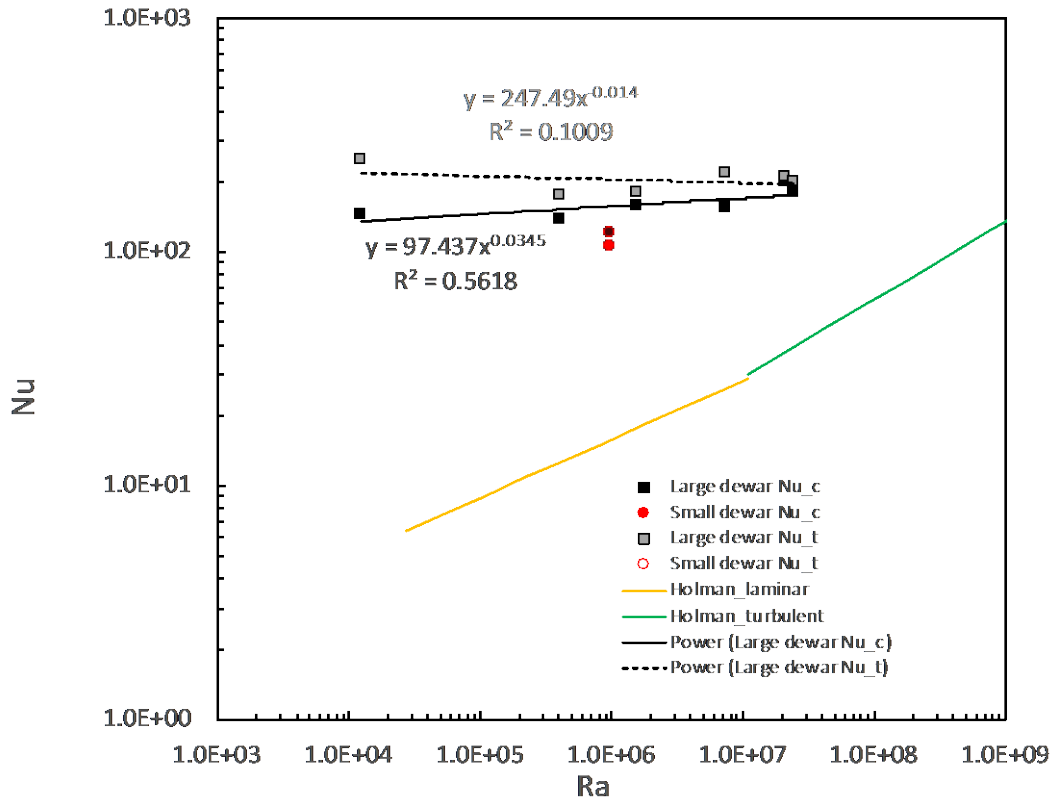


**Figure 7.3. Nusselt number correlation with Rayleigh number for convective,  $Nu_c$ , and total,  $Nu_t$ , heat transfer. Unlike Holman's correlations for horizontal circular plates, the model-test  $Nu$  values are nearly independent of  $Ra$ .**

These high heat-transfer results warrant more investigation. However, Bower and Saylor and Lunardini et al noted that mass transfer from phase change off a surface could increase mixing in the adjacent boundary layer and thereby increase the efficiency of natural-convection heat transfer [43, 47]. That may account for the high  $Nu(Ra)$  values obtained from the model tests, especially at low  $Ra$  where natural-convection flow is weak. We plan to conduct follow-on tests to confirm these higher heat-transfer rates.

### Recommended heat-transfer coefficients for Mars Rodwell simulations

The model tests yielded  $Nu_t \sim 2 \times 10^2$  independent of  $Ra$  (Figure 7.3). Assuming these results apply across the slightly greater range of interest for Mars Rodwells ( $Ra \sim 10^4 - 10^9$ ), the total heat transfer coefficient from the pool surface varies inversely with pool diameter, via Equation (7.9):

$$h_{c-t} \sim \frac{200 k}{0.9 W} \quad (7.13)$$

The thermal conductivity of CO<sub>2</sub> under Mars conditions of interest (-60°C – -80°C, 8 – 10 mbar) is nearly constant at  $k = 1.2 \times 10^{-2}$  W/mK. Table 7.3 shows the resulting predictions for the water-cavity heat transfer coefficient applicable to Mars Rodwells. The default value in the CRREL simulation model is a constant 5.7 W/m<sup>2</sup> °C. Our model-based results suggest that the simulation should vary the water-cavity heat transfer coefficient with pool size.

**Table 7.3. Model-based predictions for water-cavity heat-transfer coefficients,  $h_{w-a}$ , for Mars Rodwells based on pool diameter,  $W$ .**

<b><math>W</math> (m)</b>	0.1	0.3	0.5	1.0	3.0	5.0
<b><math>h_{w-a}</math> (W/m<sup>2</sup>°C)</b>	27	8.9	5.3	2.7	0.89	0.53

## 8.0 SUMMARY AND RECOMMENDATIONS

### Summary

Preliminary analyses indicate that a Rodwell could be an attractive option to produce water from massive ice deposits on Mars for use on future human bases. Even though these wells have been used successfully on terrestrial ice sheets for decades, the thermal design and operation of a Rodwell on Mars must contend with a low-pressure atmosphere that enhances evaporative mass loss, and hence heat loss, from the pool surface into the cavity above it. Guided by scaling analyses, we conducted small-scale tests to quantify the natural-convection mass- and heat-transfer rates from a water pool into a cavity under conditions of low CO<sub>2</sub> pressure and temperature applicable to Mars.

Instrumentation and procedural issues limited the usable data to one small-dewar and six large-dewar tests. With regard to evaporative mass transfer, the test data are consistent with dimensionless  $Sh(Ra)$  correlation developed by Bower and Saylor based on lab tests of water evaporating from a pool into a large air chamber [43]. They are also consistent with correlations derived by Ingersoll and Hecht based on natural-convection heat transfer [42, 10]. Each of these earlier correlations found  $Sh \sim Ra^{1/3}$ , with the 1/3<sup>rd</sup> power characteristic of large  $Ra$  where the boundary layer over the pool surface is turbulent. It is somewhat surprising that we found this power-law to extend into a range of  $Ra$  where laminar flow would be expected.

We found another surprising result with regard to heat transfer. Rather than follow established correlations for natural-convection heat transfer over flat plates (e.g., Holman), the dimensionless heat-transfer rates ( $Nu$ ) were much larger and approximately independent of  $Ra$  [40]. This suggests that mass transfer from the pool enhances convective heat transfer, possibly by enhanced mixing in the boundary layer. Although this possibility has been suggested in the literature, it could play an important role in a Rodwell on Mars where evaporative mass transfer is enhanced relative to terrestrial wells [43, 47].

### Recommendations

Water production on massive ice deposits could yield significant benefits for human missions to Mars. Consequently, additional investments to reduce uncertainty in Rodwell design and operation should pay large dividends through reduced risks and system optimization. Here, we recommend follow-on investigations under two broad classes: (1) fundamental heat-transfer processes, and (2) Mars Rodwell design and operation. These categories contain interlinked issues, because system parameters during startup and steady-state operation govern the size, shape and flow regime within the well. Importantly, results from small-scale tests on Earth require scaling analyses to predict full-scale performance on Mars. Those scaling analyses depend on understanding the processes that govern heat and mass transfer in the well.

Fundamental heat-transfer processes. A Rodwell presents a different system geometry than other mass- and heat-transfer studies: a circular water surface (warm) with confining walls (cold) in a dome-shaped cavity. Heat and mass transfer occur simultaneously at the boundaries, and mass transfer (ice melting, water evaporation, water-vapor condensation or crystallization) likely enhances local heat transfer. Potentially, this system is axisymmetric, although 3D instabilities (e.g., vortices) might occur within the cavity. This geometry warrants specific attention owing to the confining effect of the walls on the natural-convection flow and the enhanced heat transfer with simultaneous mass transfer.

A further complication is that water circulation within the pool, which conveys heat to the pool surface and to the melting ice walls, may be governed by natural convection or forced convection, depending upon water-injection rates and pool size. Inside the Rodwell at South Pole Station,

natural convection governs the flow field because the water-injection rate is small relative to the mass of water (Taylor et al.) [48]. This may not be true on Mars.

Lastly, high heat transfer at the pool surface in the South Pole Rodwell causes an ice cover to form on the surface. This will likely occur on Mars and should significantly reduce heat-transfer rates from the pool to the cavity. The CRREL simulation does not account for this change except through attempts to adjust overall heat-transfer coefficients to best-fit measured pool depths and diameters from past wells. The ice cover will significantly change the boundary conditions on the pool surface for momentum, mass and heat transfer for both the internal water circulation and the CO<sub>2</sub> circulation within the cavity.

Based on these concerns, we recommend the following study goals, with bulleted specific actions, to understand and quantify the fundamental heat-transfer processes governing Rodwell evolution on Mars:

1. Confirm that dimensionless natural-convection evaporation rates,  $Sh(Ra)$ , follow correlations developed by Bower and Saylor, Ingersoll and Hecht, with  $Sh \sim Ra^{1/3}$  despite low  $Ra$  where laminar flow normally prevails [43, 42, 10]. The regime  $Ra < 10^6$  has largely been unexplored in previous mass-transfer studies, yet it governs well-startup conditions on Mars.
  - Measure pool-mass changes using two low-temperature load cells in series to reduce measurement uncertainties and improve reliability.
  - Conduct all six small-dewar tests, duplicate them if possible, and duplicate all six large-dewar tests to strengthen the  $Sh(Ra)$  correlation and permit more accurate scaling to Mars conditions.
2. Confirm that dimensionless natural-convection heat-transfer rates,  $Nu(Ra)$ , from the pool surface and along the cavity walls are much higher with simultaneous mass transfer than from solid surfaces with no mass transfer, including at low  $Ra$  where laminar flow would otherwise be expected. Investigate the physics underlying this enhancement.
  - Measure total heat loss from the pool surface during evaporation tests (Series 1 above) and determine the convective and total dimensionless heat-transfer correlations.
  - Measure convective heat transfer from a horizontal plate (no mass transfer) into the same chamber across a similar range of  $Ra$ . Determine the enhancement of heat transfer with mass transfer as a function of  $Ra$ .
  - Measure cavity-wall heat transfer rates with and without mass transfer (pool and plate tests) using additional, closely spaced heat-flux sensors to map spatial variations.
  - Conduct flow-velocity mapping and flow-visualization imaging during these tests to document the overall flow field and conditions within the pool and wall boundary layers.
  - Assess whether condensation/crystallization enhances heat-transfer rate along the cavity walls. Determine the enhancement of heat transfer with mass transfer as a function of  $Ra$ .
3. Confirm that dimensionless natural-convection heat-transfer rates,  $Nu(Ra)$ , along the pool-ice walls are much higher with simultaneous melting than from a solid surface with no melting, including at low  $Ra$  where laminar flow would otherwise be expected. Investigate the physics underlying this enhancement.
  - Create a water pool within an ice block with a geometry similar to an available dewar. Place it in an environmental chamber at  $\sim 1^\circ\text{C}$  to cool the pool below  $4^\circ\text{C}$  (maximum density point for water).
  - Use a small, submerged electric heater to induce natural-convection circulation of the water, with water descending at the center and rising along the walls as it cools and



melts ice. Measure the total heat-transfer rate based on heater power, ice area and temperature difference.

- Vary parameters (pool size, heat input) to vary  $Ra$  and repeat the measurements. Establish  $Nu(Ra)$  correlation.
- Repeat tests with water inside dewars (no mass transfer) spanning a similar  $Ra$  range. Quantify heat-transfer enhancement with melting as a function of  $Ra$ .
- Conduct flow-velocity mapping and flow-visualization imaging to document the overall flow field and conditions along the ice-wall boundary layer.

Rodwell design and operation. The CRREL simulation provides an engineering tool to investigate how input parameters (injected water temperature and flow rate, water withdrawal and consumption rates) affect the shape of the well, its decent rate, pool volume and usable lifespan. The low-pressure atmosphere on Mars adds an important consideration: how to prevent boiling and loss of pool water during startup and steady-state operation. These control issues become more important on Mars owing to smaller pool sizes, higher heat-transfer rates, and more severe consequences of well failure.

Scale-model tests offer means to investigate control issues and test control strategies, provided the scaling laws that govern the heat- and mass-transfer processes are well established. Because reduced size distorts some physical processes, most studies use the largest feasible model for the facility available. They also tend to be more ambitiously instrumented to maximize the data obtained. Consequently, scale-model tests tend to be more expensive and fewer in number than fundamental-processes tests. For these reasons, we recommend an initial series of small-scale model tests followed by a more ambitious series of larger-scale tests that incorporate lessons learned. The available cold-capable vacuum chambers constrain the selection of scale factors.

We may estimate model-well dimensions by first estimating full-size (prototype) well dimensions on Mars. Note that an operational model must include the ice volume into which the well forms and evolves. Hoffman et al. conducted preliminary well analyses using the CRREL simulation to estimate thermal power requirements for baseline levels of water production [7]. For production rates ranging 120 – 400 l/day at thermal power 2 – 10 kW, final well diameters and depths ranged 5 – 10 m and 2.5 – 5 m, respectively, with cavities about equal in height to the well diameters. Lunardini and Rand approximated the radius into the ice that the pool's thermal disturbance penetrates as 4.5 times the pool radius [9]. These values suggest that a full-size (prototype) well would disturb an ice cylinder ranging 30 – 60 m diameter by 35 – 70 m deep. An initial test series could use the same bell jar as for the present tests, which would dictate scale factors (prototype/model dimensions) of 60 – 120. NASA JSC also has a 4.6-m-dia cold-capable vacuum chamber, which would permit operational model tests at scale factors of 10 - 20 for the more ambitious tests.

The major goal for model tests would be to determine whether and under what conditions a Rodwell on Mars could be initiated and operated stably and reliably. It could also serve to assess the need to pressurize the well to avoid boiling and instability. In addition, flow and heat-transfer measurements could resolve the nature of the flow regimes established in the pool and cavity and determine whether mass- and heat-transfer rates derived from fundamental tests adequately predict those inside the working model. This latter determination would increase confidence that the scaled-up model performance accurately reflects the performance of a well on Mars. Lastly, data and insight gained from the tests would guide revisions to the CRREL simulation, or guide development of a more sophisticated simulation, to conduct tradeoff studies for Rodwells matched to Mars mission scenarios.

## 9.0 REFERENCES

- 1 Di Achille, G., Hynek, B.M., "Ancient ocean on Mars supported by global distribution of deltas and valleys," 2010, *Nature Geoscience*. 3 (7): 459–463, DOI:10.1038/ngeo891.
- 2 Beaty, D.W., Mueller, R.P., Bussey, D.B., Davis, R.M., Hays, L.E., Hoffman, S.J., Zbinden, E., "Some Strategic Considerations Related to the Potential Use of Water Resource Deposits on Mars by Future Human Explorers," ASCE Earth and Space Conference, Orlando, FL, April 11-15, 2016.
- 3 Beaty, D.W., Hays, L.E., Davis, R.M., Bussey, D.B., Abbud-Madrid, A., Boucher, D., Gertsch, L., Kleinhenz, J., Mueller, R.P., van Susante, P., Whetsel, C., Zbinden, E., Zurek, R., Hoffman, S.J., "The Possible Strategic Significance of Mid-Latitude Ice Deposits to a Potential Future Human Mission to Mars (abs.)," LPI Contribution No. 1926, id.6059, Sixth International Conference on Mars Polar Science and Exploration. University of Iceland, Reykjavik, Iceland, September 5-9, 2016.
- 4 Dundas, C.M., Bramson, A.M., Ojha, L., Wray, J.J., Mellon, M.T., Byrne, S., McEwen, A.S., Putzig, N.E., Viola, D., Sutton, S., Clark, E., and Holt, J.W., "Exposed subsurface ice sheets in the Martian mid-latitudes," *Science* 359, 12 Jan 2018, pp. 199-201, DOI: 10.1126/science.aao1619.
- 5 Abbud-Madrid, A., Beaty, D.W., Boucher, D., Bussey, D.B., Davis, R., Gertsch, L., Hays, L.E., Kleinhenz, J., Meyer, M.A., Moats, M., Mueller, R.P., Paz, A., Suzuki, N., van Susante, P., Whetsel, and C., Zbinden, E.A., 2016, Report of the Mars Water In-Situ Resource Utilization (ISRU) Planning (M-WIP) Study; 90 p, posted April, 2016 at [http://mepag.nasa.gov/reports/Mars\\_Water\\_ISRU\\_Study.pptx](http://mepag.nasa.gov/reports/Mars_Water_ISRU_Study.pptx).
- 6 Kleinhenz, J.E. and Paz, A., "An ISRU Propellant Production System to Fully Fuel a Mars Ascent Vehicle," AIAA-2017-0423, American Institute for Aeronautics and Astronautics 2017 Science and Technology Forum and Exposition (AIAA SciTech Forum 2017), Grapevine, TX, January 9–13, 2017.
- 7 Hoffman, S.J., Andrews, A.D., Joosten, B.K., and Watts, K.D., "A Water Rich Mars Surface Mission Scenario," Paper 2422, IEEE Aerospace Conference 2017, Big Sky, MT, March 4-11, 2017.
- 8 Hoffman, S.J., Andrews, A.D., and Watts, K.D., "Simulated Water Well Performance on Mars," AIAA Space and Astronautics Forum and Exposition, Orlando, FL, September 17-19, 2018.
- 9 Lunardini, V.J. and Rand, J., "Thermal Design of an Antarctic Water Well," US Army Cold Regions Research and Engineering Laboratory, Special Report 95-10, 1995.
- 10 Hecht, M.H., "Metastability of Liquid Water on Mars," *Icarus*, Volume 156, pp. 373-386, 2002; DOI:10.1006/icar.2001.6794
- 11 Drake, B. G., (ed.), Human Exploration of Mars Design Reference Architecture 5.0, NASA-SP-2009-566, July 2009.

- 12 Bussey, D.B. and Hoffman, S.J., "Human Mars Landing Site and Impacts on Mars Surface Operations," IEEE-2016-2515, IEEE Conference, Big Sky, MT, March, 2016.
- 13 Craig, D.A., Troutman, P., and Herrmann, N.B., "Pioneering Space Through an Evolvable Mars Campaign," AIAA 2015-4409, AIAA 2015 Conference and Exposition, Pasadena, CA, Aug. 31 – Sept. 2, 2015.
- 14 Polsgrove, T., Chapman, J., Sutherlin, S., Taylor, B., Fabisinski, L., Collins, T., Ciancolo, A.D., Samareh, J., Robertson, E., Studak, W., Vitalpur, S., Lee, A.Y., and Rakow, G., "Human Mars Lander Design for NASA's Evolvable Mars Campaign," 37th IEEE Aerospace Conference, Big Sky, MT, March 5-12, 2016.
- 15 Polsgrove, T., NASA Marshall Space Flight Center, Private Communication, 2016.
- 16 Goodlyff, C., NASA Langley Research Center, Private Communication, 2016.
- 17 Eagle Engineering, Inc., "Lunar Surface Transportation Systems Conceptual Design," NASA Contract Number NAS9-17878, 1988.
- 18 Slaba, T.C., Mertins, C.J., and Blattnig, S.R., "Radiation Shielding Optimization on Mars," NASA Technical Publication 2013-217983, 2013.
- 19 Sanders, G., NASA Johnson Space Center, Private Communication, 2016.
- 20 Carr, M.H. and Head, J.W., "Martian Unbound Water Inventories: Changes with Time," Eighth International Conference on Mars, 2014.
- 21 Carter, J., Poulet, F., Bibring, J.P., Mangold, M., and Murchie, S., "Hydrous Minerals on Mars as seen by the CRISM and OMEGA Imaging Spectrometers: Updated Global View," *Journal of Geophysical Research: Planets* Vol. 118, 831-858, 2013.
- 22 McEwan, A.S., Dundas, C.M., Mattson, S.S., Toigo, A.D., Ojha, L., Wray, J.J., Chojnacki, M., Byrne, S., Murchie, S.L., and Thomas, N., "Recurring Slope Lineae in Equatorial Regions of Mars," *Nature Geoscience* 7, 53-58, 2014.
- 23 Dundas, C., McEwen, A., Chojnacki, M., Milazzo, M., Byrne, S., Mcelwaine, J., and Urso, A., "Granular Flows at Recurring Slope Lineae on Mars Indicate a Limited Role for Liquid Water," *Nature Geoscience*. 10, 10.1038/s41561-017-0012-5, 2017.
- 24 Clifford, S.M., Lasue, J., Heggy, E., Boisson, J., McGovern, P., and Max, M.D., "Depth of Martian Cryosphere: Revised Estimates and Implications for the Existence and Detection of Subpermafrost Groundwater," *Journal of Geophysical Research*, Vol. 115, 2010.
- 25 Feldman, W.C., Prettyman, T.H., Maurice, S., Plaut, J.J., Bish, D.L., Vaniman, D.T., Mellon, M.T., Metzger, A.E., Squyers, S.W., Karunatillake, S., Boynton, W.V., Elphic, R.C., Funsten, H.O., Lawrence, D.J., and Tokar, R.L., "The Global Distribution of Near-Surface Hydrogen on Mars," *Journal of Geophysical Research: Planets*, Vol. 109, 2004.

- 26 Dickson, J.L., Head, J.W., and Fassett, C.I., "Patterns of accumulation of ice in the mid-latitudes of Mars during the Amazonian," *Icarus* 219, 723-732, 2012.
- 27 Holt, J.W., Safaeinili, A., Plaut, J.J., Head, J.W., Phillips, R.S., Seu, R., Kempf, S.D., Choudhary, P., Young, D.A., Putzig, N.E., BiccaRi, D., and Gim, Y., "Radar Sounding Evidence for Buried Glaciers in the Southern Mid-Latitudes of Mars," *Science* 322, 1235-1238, 2008.
- 28 Dundas, C.M., Byrne, S., McEwan, A.S., Mellon, M.T., Megan, R.K., Daubar, I.J., and Saper, L., "HiRISE observations of new impact craters exposing Martian ground ice," *Journal of Geophysical Research: Planets*, 10.1002/2013JE004482, 2014.
- 29 "Camp Fistclench" acquired from [https://en.wikipedia.org/wiki/Camp\\_Fistclench](https://en.wikipedia.org/wiki/Camp_Fistclench). Copied on 2 September 2020.
- 30 Clark, Elmer F., "Camp Century; Evolution of Concept and History of Design, Construction and Performance," U.S. Army Corps of Engineers Cold Regions Research and Engineering Laboratory, Technical Report 174, October 1965.
- 31 Russell, F. L., Performance, "Water Production in a Polar Ice Cap by Utilization of Waste Engine Heat" U.S. Army Corps of Engineers Cold Regions Research and Engineering Laboratory, Technical Report 168, December 1965.
- 32 Taylor, S., Lever, J.H., Harvey, R.P., and Govoni, J., "Collecting Micrometeorites from the South Pole Water Well," U.S. Army Corps of Engineers Cold Regions Research and Engineering Laboratory, Report 97-1, May 1997.
- 33 Benson, T., Cherwinka, J., Duvernois, M., Elcheikh, A., Feyzi, F., Greenler, L., Haugen, J., Karle, A., Mulligan, M., and Paulos, R., "IceCube Enhanced Hot Water Drill functional description," *Annals of Glaciology*, 55(68), 2014.
- 34 Lufkin, L.E. and Tobiasson, W., "The 50-Man Winter Camp at Tuto, Greenland," U.S. Army Corps of Engineers Cold Regions Research and Engineering Laboratory, Technical Report 214, August 1969.
- 35 Haehnel, R.B. and Knuth, M.A., "Potable water supply feasibility study for Summit Station, Greenland," ERDC/CRREL TR-11-4. Hanover, NH: U.S. Army Engineer Research and Development Center, 2011.
- 36 Taylor S., Lever, J.H., and Harvey, R.P., "Numbers, types and compositions of an unbiased collection of cosmic spherules," *Meteoritics and Planetary Sciences*, 35, 651-666, 2000.
- 37 Taylor S., Herzog, G.F., and Delaney, J.S., "Crumbs from the crust of Vesta: Achondritic cosmic spherules from the South Pole water well," *Meteoritics and Planetary Sciences*, 42, 223-233, 2007.

- 38 Taylor S., Matrajt, G., and Guan, Y., "Fine-grained precursors dominate the micrometeorite flux," *Meteoritics and Planetary Sciences*, 47, 550-564, 2012.
- 39 Taylor S., Messenger, S., and Folco, L., "Cosmic Dust: finding a needle in a haystack," *Elements*, 12, 171-176.1, 2016.
- 40 Holman, J.P. "Heat Transfer," 4<sup>th</sup> Edition, McGraw-Hill, New York, 1976.
- 41 Lunardini, V.J., "Heat Transfer with Freezing and Thawing," Amsterdam, New York: Elsevier Scientific Publishing Co., p. 247, 1991.
- 42 Ingersoll, A.P., "Mars: Occurrence of liquid water," *Science* 169, 972 – 973, 1970.
- 43 Bower, S. and Saylor, J., "A study of the Sherwood-Rayleigh relation for water undergoing natural convection-driven evaporation," *International Journal of Heat and Mass Transfer* 52, 2009.
- 44 Boynton, W. P. and Brattain, W. H.: 1929, in *International Critical Tables* (ed. by E. W. Washburn), McGraw-Hill, New York.
- 45 Sharpley, B.F. and Boelter, L.M.K., "Evaporation of water into quiet air from a one-foot diameter surface," *Industrial and Engineering Chemistry*, 1125 – 1131, 1938.
- 46 Boelter, L.M.K, Gordon, H.S., and Sharpley, B.F., "Free evaporation into air of water from a free horizontal quiet surface," *Industrial and Engineering Chemistry* 38, 596 – 600, 1946.
- 47 Lunardini, V.J., "Condensing steam tunnel heat sinks," USA Cold Regions Research and Engineering Laboratory, Special Report 86-24, 1986.
- 48 Taylor, S., Lever, J.H., Harvey, R.P., "Accretion rate of cosmic spherules measured at the South Pole," *Nature*, Vol 392, pp. 899-903, 30 April, 1998.
- 49 Zubrin, Robert M., Baker, David A., Gwynne, Owen, "Mars Direct: A Simple, Robust, and Cost Effective Architecture for the Space Exploration Initiative", 29<sup>th</sup> AIAA Aerospace Sciences Meeting, Reno, NV, Jan. 7-10, 1991.

## APPENDIX A DETAILS OF WATER USAGE ESTIMATES

To estimate the water requirements for a “typical” crewed Mars surface mission [7], we use the characteristics of NASA’s recent “Evolvable Mars Campaign” studies [13]. In these, each surface mission consists of a crew of four on the Martian surface for about 500 days utilizing a central habitation module for crew living/working activities, spacesuits and pressurized rovers for remote exploration, and a single ascent vehicle for return to an orbiting interplanetary vehicle. For each of these functional elements, we investigate the maximum use of Martian resources, including water, to reduce the amount of supplies required to be transported from Earth. We do not attempt to perform conceptual designs of the processing equipment and associated power systems here; instead, we simply use likely processing chemistry to estimate the water required in order to inform resource requirements.

### Ascent Propellant

Many previous studies have examined the use of Martian resources for ascent vehicle propellant production [11, 49]. One of the most effective propellant combinations is methane and oxygen, but previous uncertainties in the availability of easily extractable Martian water has limited the concepts to production of oxygen only (extracted from the carbon dioxide in the Martian atmosphere) or, at best, the importation of terrestrial hydrogen for use in a combination of water electrolysis and Sabatier processes. Such a process, modified for the utilization of Martian water, is shown in Figure A-1, along with the water-to-product mass ratios. Note that only Martian resources are required for process feedstock.

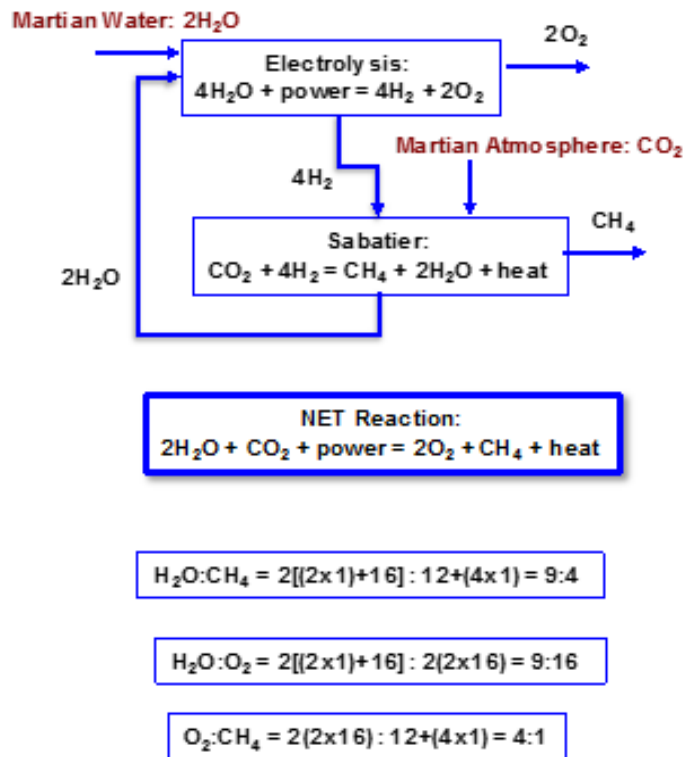


**Figure A-1. Assumed Resource Production Process**



Extensive Mars Ascent Vehicle (MAV) design studies were performed as part of the Evolvable Mars Campaign analysis [14]. Typically, to maximize the benefit of in-situ produced propellant, the transportation architecture will be biased toward the highest Mars orbit practical for the MAV-to-interplanetary vehicle rendezvous. Such a vehicle concept is depicted in Figure A-2 [15].

The total propellant load required is 38,506 kg at an oxidizer-to-fuel (OF) ratio of 3.4. Given the water-to-product mass ratios from Figure A-1, this will require 19,683 kg (~5,210 gallons) of Martian water (and 24,059 kg of Martian CO<sub>2</sub>). Since the Sabatier/water electrolysis process produces oxygen and methane in a 4:1 ratio, 5,235 kg of excess oxygen will be produced.



Subsystem	Mass (kg)	
	MDM Payload	Mars Liftoff
<b>Crew Cabin</b>	<b>3,427</b>	<b>4,122</b>
Structures	881	881
Power	377	377
Avionics	407	407
Thermal	542	542
ECLS	502	502
Cargo	422	1,117
Non-Prop. Fluids	295	295
<b>1<sup>st</sup> Stage</b>	<b>9,913</b>	<b>31,432</b>
Dry Mass	3,605	3,605
LO <sub>2</sub>	0	21,519
LCH <sub>4</sub>	6,308	6,308
<b>2<sup>nd</sup> Stage</b>	<b>5,006</b>	<b>13,246</b>
Dry Mass	2,566	2,566
LO <sub>2</sub>	0	8,239
LCH <sub>4</sub>	2,440	2,440
<b>TOTALS</b>	<b>18,345</b>	<b>48,799</b>

**Figure A-2. Mars Ascent Vehicle Conceptual Design**

## Life Support

Traditional Mars surface habitation systems assume closed-loop (recyclable) water and oxygen systems for crew life support. Closed loop systems greatly reduce the import mass requirements for these commodities, but they are complex and, as experience on the International Space Station has indicated, prone to frequent repair and maintenance. In addition, the power and mass of these systems limit water usage to rather basic levels (e.g., no showers, laundry, etc.).

With the availability of Martian water, the strategy for life support could change in several ways.

1. It could be advantageous to reduce the water and oxygen recycling levels to increase reliability or reduce system development costs, using in situ Martian water to make up the differences.
2. Systems could “temporarily” rely on Martian water to allow for repair and maintenance of closed-loop systems.
3. Life support could rely completely on Martian water for life support water and oxygen, thereby eliminating both development cost and mass of closed-loop systems.

It should be stressed that open-loop water systems introduce the issue of cleanup or sequestration of waste water before reintroduction into the Martian environment. Sequestration could be possible by storage of waste water containers in used logistics modules, for example. However, if high waste water cleanliness levels are necessary, advantages of open-loop systems may be less apparent. This will need to be addressed as part of the overall human Mars mission in the context of planetary protection.

Water resupply requirements for closed-loop, “restrained” open-loop, and “robust” open-loop scenarios for a four-crew 500-day surface mission are shown in Table A-1 [16]. The relatively low closed-loop water makeup requirements are due to the intrinsic water content in the crew’s food supply, and the closed-loop oxygen makeup is delivered in the form of water which is subsequently electrolyzed for oxygen. The open-loop requirements illustrate one case with the same usage level as the closed-loop and a second case with a substantially higher level due to the addition of a laundry system.

It can be seen that for the “restrained” open-loop case, the 500-day water requirement is 9,519 kg (~2,520 gallons), or about half of that required for propellant production. The addition of the laundry more than doubles that amount. In any case, the life-support water needs are “in kind” with those of the MAV.

Finally, it should be pointed out that the excess oxygen resulting from the propellant production exceeds the crew’s metabolic oxygen requirement, so it is not bookkept in Table A-1.

**Table A-1. Life Support Water Supply Requirement (4 Crew for 500 Days)**

	<b>CLOSED-LOOP H<sub>2</sub>O, O<sub>2</sub></b>	<b>OPEN-LOOP H<sub>2</sub>O, O<sub>2</sub></b>	<b>OPEN-LOOP + LAUNDRY</b>
<b>H<sub>2</sub>O CLOSED-LOOP MAKEUP</b>	970	0	0
<b>O<sub>2</sub> CLOSED-LOOP MAKEUP</b>	2,480	0	0
<b>LAUNDRY</b>	0	0	14,660
<b>EVA</b>	0	3,072	3,072
<b>FOOD REHYDRATION</b>	0	1,070	1,070
<b>MEDICAL</b>	0	107	107
<b>DRINK</b>	0	4,280	4,280
<b>FLUSH</b>	0	134	134
<b>HYGIENE</b>	0	856	856
<b>TOTAL</b>	3,450 kg (~913 gallons)	9,519 kg (~2,520 gallons)	24,379 kg (~6,549 gallons)

## Radiation Protection

Outside of the Earth's magnetosphere, there are generally two types of radiation that can impact crews' health – Solar Particle Events (SPEs) and Galactic Cosmic Radiation (GCR). On the Martian surface, the SPEs are greatly attenuated (approximately an order of magnitude) by the atmosphere. GCR is also somewhat attenuated. However, interaction between GCR ions and the atmospheric molecules result in a pion and electromagnetic cascade (" $\pi$ /EM cascade"). In addition, collision between GCR ions and the Martian soil creates a neutron field ("albedo neutrons"). Both of these GCR effects contribute to the total exposure experienced by a crewmember on the Martian surface. The effectiveness of using Martian water as a shield was investigated.

Models have been developed [18] to account for GCR effects including four- $\pi$  radiation transport methodology ("HZETRN- $\pi$ /EM") through an atmospheric density/ composition model, a regolith model and a shielding material model using the International Commission on Radiological Protection (ICRP) Publication 60 quality factor to compute the GCR dose equivalent. A human phantom model is used to compute dose equivalence at radiosensitive tissue targets and weighted (ICRP 103) to compute effective dose. Shielding effectiveness has been computed for aluminum and polyethylene, and as polyethylene characteristics are nearly identical to water, we use that model here.

Figure A-3 illustrates the effects of various factors in reducing the GCR effective dose on the Martian surface. As can be seen, by far the greatest reductions are due to the planetary blockage of half the sky and atmospheric attenuation (but still taking into account  $\pi$ /EM cascade and albedo neutrons). The additive effect of a water shield, however, is disappointingly small. Even very large quantities of water shielding only reduce effective dose by around 20%. This is caused by GCR-induced neutron production and emission *in the shielding material itself*.

Nevertheless, for study purposes we assumed 20 g/cm<sup>2</sup> of water shielding – equivalent to a 20 cm thick water shell – around a Mars surface habitat. Such a shell would provide about 15% effective dose reduction. Assuming the habitat is a 7 m diameter cylinder that is 6.5 m tall (typical of conceptual habitat designs), this shell would be the equivalent of 43,000 kg (~11,382 gallons) of water.

Such a water shell could be combined with the water quantities previously calculated for a robust open-loop life support scenario. The radiation shield could represent a life-support water "buffer" or storage supply for such an open loop system. If configured correctly, this buffer would provide the additional benefit of (albeit limited) radiation shielding.

## Mobility Power

For extended surface mobility and exploration exceeding the time limits imposed by spacesuits, pressurized, multi-crewmember rovers are often envisioned. Power sources for these concepts are always problematic, however, especially in multi-day traverse scenarios. Battery weights are prohibitive without recharge and solar arrays consistent with recharge power levels are inconsistent with roving vehicles. Alternative concepts involving small nuclear power sources may be technically viable, but have significant cost implications.

Hydrogen-oxygen fuel cells have also been proposed as a power source [17], but the volumetric and cryogenic challenges of liquid hydrogen, along with the regeneration challenges of liquid hydrogen and the regeneration

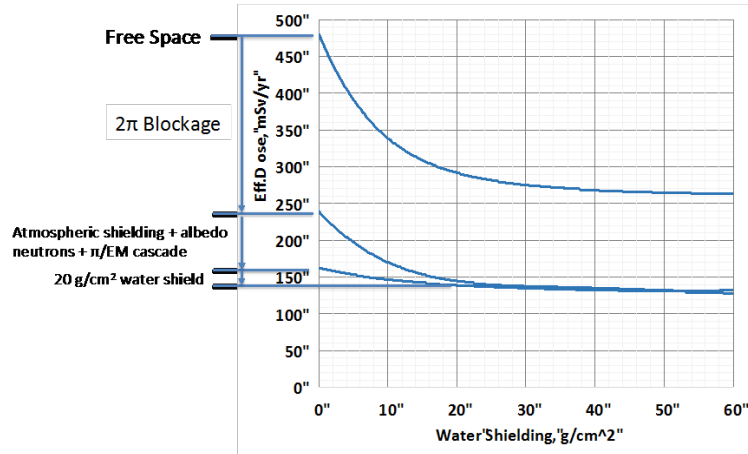


**Figure A-3. GCR Water Shielding Effectiveness**

necessity with no Martian hydrogen source, have made this choice unattractive. However, Martian water combined with methane reformer technology may offer a better answer.

Solid oxide fuel cells can utilize methane and oxygen to produce electrical power for rover drive motors and for life support. The hydrogen-oxygen fuel cell produces water, which is fed into a steam reformer to generate hydrogen from methane (produced, in turn, from Martian water and carbon dioxide), which is fed into the fuel cell. The reaction is illustrated in Figure A-4. Note that the oxygen and methane are consumed in a 3:1 mass ratio, indicating that if the reactants are produced from the Sabatier/electrolysis process, excess oxygen will once again result (just as in MAV propellant production). In addition, water in excess of that required by the steam reformer is produced from the fuel cells, and is available for crew metabolic needs, either as potable water or as oxygen via electrolysis.

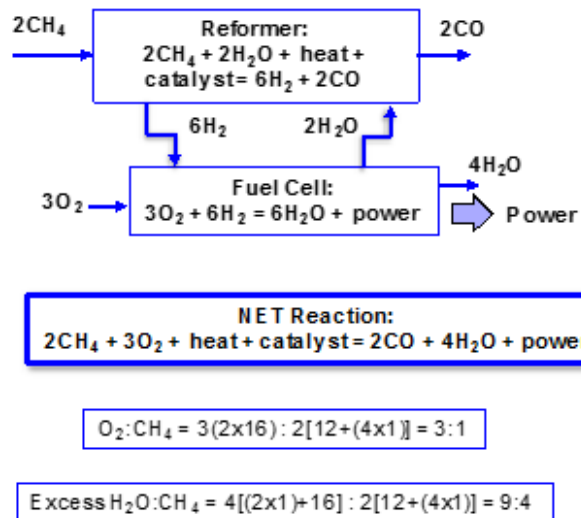


**Figure A-4. Methane Oxygen Fuel Cell Chemistry**

To characterize performance, we postulate rover and surface excursion parameters [19] shown in Table A-2 (1 sol = 1 Martian day, 24.65 hrs). As can be seen, the fuel cells will produce 621 kg (~164 gallons) of water in excess of that required by the methane reformer, more than enough to supply the crew's potable water requirement (estimated at 100 kg for a crew of two). To extrapolate this excursion over the duration of a 500-day surface mission, we assume that for every excursion, two rovers will explore in tandem to maintain mutual rescue capability in case of

malfunction, and that such an excursion is performed every 28 sols, resulting in 18 excursions per mission. This equates to a total requirement of 9,936 kg of methane and 30,276 kg of oxygen. Again, assuming Sabatier/electrolysis methane-oxygen production, this will require 22,396 kg (~5,928 gallons) of Martian water – similar in magnitude to the MAV propellant requirement.

**Table A-2. Surface Excursion Characteristics**

<b>TRIP DURATION</b>	14 sols
<b>NO. OF DAYS DRIVING</b>	9 sols
<b>CREW</b>	2
<b>ROVER DRIVE TIME/SOL</b>	9 hours
<b>TOTAL ENERGY NEEDED</b>	1,564 kW-hrs
<b>TOTAL O<sub>2</sub> NEEDED</b>	841 kg
<b>TOTAL CH<sub>4</sub> NEEDED</b>	276 kg
<b>EXCESS H<sub>2</sub>O PRODUCED</b>	621 kg (~164 gallons)

### Summary of Surface Mission Water Requirements

By totaling the MAV, “robust” open-loop life-support, and mobility requirements, we can estimate total “per mission” water extraction requirements, shown in Table A-3, assuming Martian water (and carbon dioxide) are the sole feedstock for the products. Such a summation can aid in developing water extraction and processing concepts and the associated power requirements. It should be pointed out that little effort has been made in optimizing or integrating these needs.

**Table A-3. Products and Required Feedstock (per Mission)**

	<b>O<sub>2</sub></b>	<b>CH<sub>4</sub></b>	<b>H<sub>2</sub>O</b>	<b>Martian H<sub>2</sub>O Required</b>
<b>MAV</b>	29,758	8748	N/A	19,683
<b>Life Support</b>	N/A	N/A	24,379	24,379
<b>Mobility</b>	30,276	9936	N/A	22,936
<b>Total</b>	<b>60,034 kg</b> <b>(~15,891 gallons)</b>	<b>18,684 kg</b> <b>(~4,946 gallons)</b>	<b>24,379 kg</b> <b>(~6,453 gallons)</b>	<b>66,998 kg</b> <b>(~17,735 gallons)</b>

For example, while surface roving excursions are taking place, habitat consumables requirements will be reduced. It has, however, been pointed out that habitat oxygen needs can be met with excess MAV oxygen production, rover life support consumables can be produced with fuel cell excess water production, and a life support water buffer can produce modest radiation protection.

Assuming a continuing series of human excursions to the Martian surface, the cadence of these missions will dictate the necessary commodity production rates and hence the water extraction rates. The “Evolvable Mars Campaign” was predicated on a Mars surface mission on alternating Earth-Mars synodic periods, implying a mission every 50 months. Combined with the per-mission requirements of Table A-3, this implies production and water extraction rates shown in Table A-4.

**Table A-4. Commodity Production and Martian Water Extraction Rates**

<b>O<sub>2</sub> PRODUCTION</b>	14,141 kg/yr
<b>CH<sub>4</sub> PRODUCTION</b>	4,486 kg/yr
<b>H<sub>2</sub>O PRODUCTION</b>	5,853 kg/yr
<b>MARTIAN H<sub>2</sub>O REQUIRED</b>	<b>16,086 kg/yr</b> <b>(~4,258 gallons/yr)</b>

## APPENDIX B EXPERIMENT EQUIPMENT DETAILS

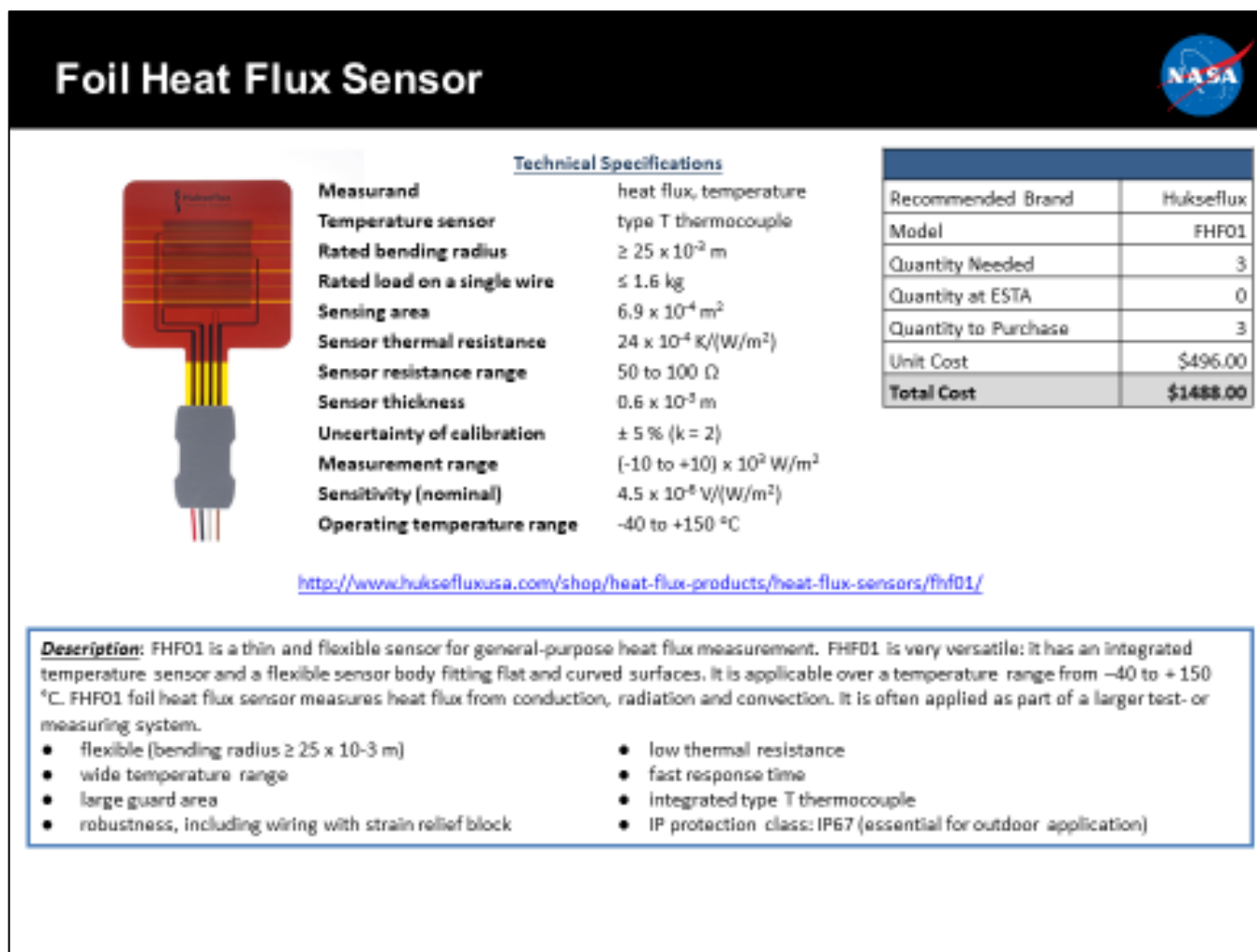
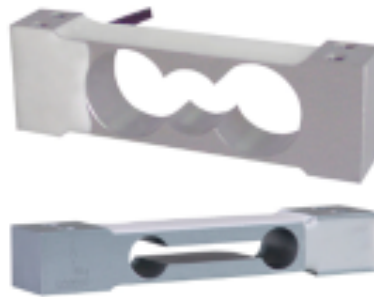


**Figure B.1. Foil Heat Flux Sensor**



# Load Cell



## Technical Specifications

Weight Capacity	3 kgf
Measurement Units	kgf
Force Direction	Compression
Linearity	$\pm 0.028\%$
Electrical Output (nominal)	1mV/V
Height	0.87 in
Width	0.47 in
Length	2.75 in
Connection Type	Cable
Cable Length	1.5 ft
Serial Number	SD002377
Material	Alloy Aluminum
Capacity	3 kg
Excitation	10 VDC Nom. 15 VDC Max.

Recommended Brand	OMEGA
Model	LC615P-3KG
Quantity Needed	1
Quantity at ESTA	0
Quantity to Purchase	1
Unit Cost	\$136.89
<b>Total Cost</b>	<b>\$136.89</b>

## Calibration Data (Serial Number SD002377)

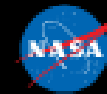
Full Scale Output	0.81 mV/V	Zero Balance	<2.0% of FS
Input Resistance	406 $\pm$ 6 Ohms	Output Resistance	350 $\pm$ 3 Ohms
Temp. Sens. Zero	< 0.02 %FS/10°C	Comp. Temp. Range	-10°C – 40°C
Temp. Sens. Output	< 0.02 %LD/10°C	Combined Error	C3D
Ultimate Overload	150%		

<https://www.omega.com/en-us/sensors-and-sensing-equipment/load-and-force/load-cells/lc60/p/LC615P-3KG>

**Description:** Omega's LC60 Series is a low cost, highly accurate, single point load cell, ideal for OEM applications such as electronic scales and weighing machines. The single point design is highly resistant to eccentric loading, allowing direct mounting to the scale base and weighing platform. The LC60 Series features a moisture-proof sealant and is available in ranges from 600 grams to 200 kilograms.

Figure B-2. Load Cell

## Stir Bar (7 pcs)



### Technical Specifications

Color	White
Item Weight	3.53 ounces
Number of Items	7
Shape	Egg Shaped
Length	Varying Lengths
Material	PTFE

Recommended Brand	Ronyes Lifescience
Part Number	43217-20043
Quantity Needed	1
Quantity at ESTA	0
Quantity to Purchase	1
Unit Cost	\$13.89
<b>Total Cost</b>	<b>\$13.89</b>

[https://www.amazon.com/Magnetic-Stirrers-Mixer-Spinbar-Stirring/dp/B07BF2B39P/ref=asc\\_df\\_B07BF2B39P/?tag=hyprod-20&linkCode=df0&hvadid=312158944530&hvpas=1a8&hvmcbe=g&hvrnd=1345168433113872926&hvpone=&hvptwo=&hvamt=&hvdvc=&hvdvndli=&hvlocint=&hvlocphy=9](https://www.amazon.com/Magnetic-Stirrers-Mixer-Spinbar-Stirring/dp/B07BF2B39P/ref=asc_df_B07BF2B39P/?tag=hyprod-20&linkCode=df0&hvadid=312158944530&hvpas=1a8&hvmcbe=g&hvrnd=1345168433113872926&hvpone=&hvptwo=&hvamt=&hvdvc=&hvdvndli=&hvlocint=&hvlocphy=9)

**Description:** The stir bars are coated in PTFE, which is chemically inert and will not contaminate or chemically react with the liquid. PTFE also one of the lowest coefficients of friction of any solid, which means it could reduce friction while in spinning. Recessed bezel helps to reduce vibration while stirring. Particularly Useful for Environmental Testing and Life Package Includes: Egg Shape Stir Bar 7pcs

Figure B.3. Stir Bar

## Insulated Dewar (3-inch I.D.)

Note: Not purchased with first order



### Technical Specifications

Volume	275 mL
Inside Diameter (ID)	3.0 in / 9.8 cm
Outside Diameter (OD)	5.0 in / 13.0 cm
Height	3.0 in / 7.6 cm
Depth	2.2 in / 5.6 cm

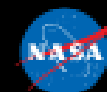
Recommended Brand	Cole-Parmer
Model	EW-03771-21
Quantity Needed	2
Quantity at ESTA	0
Quantity to Purchase	2
Unit Cost	\$303.00
<b>Total Cost</b>	<b>\$606.00</b>

<https://www.coleparmer.com/i/low-form-dewar-flasks-glass-and-aluminum-275-ml/0377121>

**Description:** The protective aluminum base on both sides extends the full height of the Dewars. Protected vacuum tip-off tubulations are off to the side to minimize space between the bottoms and magnetic stirrers.

Figure B.4. Insulated Dewar (3-inch I.D.)

## Insulated Dewar (6-inch I.D.)



### Technical Specifications

Volume	600 mL
Inside Diameter (ID)	5.5 in / 14 cm
Outside Diameter (OD)	6.5 in / 16.5 cm
Height	3.4 in / 8.6 cm
Depth	2.6 in / 6.7 cm

Recommended Brand	Cole-Parmer
Model	AO-03771-23
Quantity Needed	2
Quantity at ESTA	0
Quantity to Purchase	2
Unit Cost	\$170.76
<b>Total Cost</b>	<b>\$341.52</b>

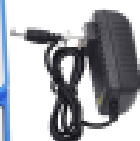
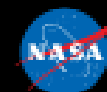
[https://www.amazon.com/Form-Dewar-Flasks-Glass-Aluminum/dp/B003M1S5WY/ref=sr\\_1\\_13?ie=UTF8&qid=1545333765&sr=8-13&keywords=dewar+flask#feature-bullets-btf](https://www.amazon.com/Form-Dewar-Flasks-Glass-Aluminum/dp/B003M1S5WY/ref=sr_1_13?ie=UTF8&qid=1545333765&sr=8-13&keywords=dewar+flask#feature-bullets-btf)

**Description:** These dewar flasks expand the applications of standard cylindrical or spherical dewars. The protective aluminum base on both sides extends the full height of the dewars. Protected vacuum tip-off tabulations are off to the side to minimize space between the bottoms and magnetic stirrers. These dewars permit operations not practical with standard dewars small flasks can be inserted into dewars. Rapid freezing and recovery of tissue/organ specimens. Agitation can be provided with a magnetic stirrer.

Figure B.5. Insulated Dewar (6-inch I.D.)

# Magnetic Induction Stirrer

Note: One received; second copy to be ordered



## Technical Specifications

Input	AC 100-240V ~ 50HZ/60HZ
Mixing Speed	0 ~ 3000 rpm
Max Mixing Volume	3000 mL
Overall Dimensions	180 X 130 X 45 mm (7.1 x 5.1 x 1.8 in)
Working Table Dimensions	130 x 130 mm
Table Material	316 Stainless Steel Plate
Weight	490 g

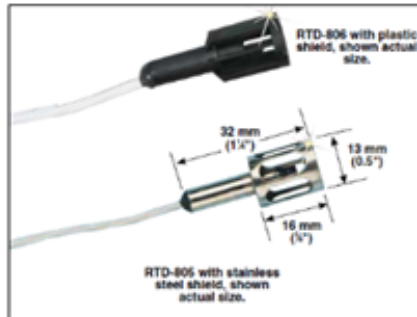
Recommended Brand	INTLLAB
Model	MS-500
Quantity Needed	1
Quantity at ESTA	0
Quantity to Purchase	1
Unit Cost	\$29.80
Total Cost	\$29.80

[https://www.amazon.com/Magnetic-stirrer-magnetic-Stirring-Capacity/dp/B072K24XSP/ref=az\\_q\\_bs\\_318023011\\_1?encoding=UTF8&psc=1&refRID=QZFPDFBJQ9N1ZN0MNTQ4](https://www.amazon.com/Magnetic-stirrer-magnetic-Stirring-Capacity/dp/B072K24XSP/ref=az_q_bs_318023011_1?encoding=UTF8&psc=1&refRID=QZFPDFBJQ9N1ZN0MNTQ4)

**Description:** This magnetic stirrer is ideal for stirring in scientific research, industry, agriculture, health and medicine, homebrew, etc. It comes with one magnetic stir bars (7mm x 30mm). The speed range is 0-3000 rpm. Maximum stirring volume: 3000 ml (0.8 gallons). Not suitable for highly viscous solutions. Glass beakers are not included.

Figure B.6. Magnetic Induction Stirrer

# Submersible Thermistor



## Technical Specifications

Temperature Coefficient (Alpha)	.00385 $\Omega/\Omega/^{\circ}\text{C}$
Resistance ( $\Omega$ ) at 0 $^{\circ}\text{C}$	100.00 $\pm$ 0.12
Maximum Working Temp	230 $^{\circ}\text{C}$ (450 $^{\circ}\text{F}$ )
Temperature Range	-50 to 230 $^{\circ}\text{C}$ (-60 to 445 $^{\circ}\text{F}$ )

Recommended Brand	OMEGA
Model	805-B / 806-B
Quantity Needed	7
Quantity at ESTA	7
Quantity to Purchase	0
Unit Cost	N/A
<b>Total Cost</b>	<b>N/A</b>

<https://www.omega.com/en-us/temperature-measurement/temperature-probes/air-sensor-probes/p/RTD-805-RTD-806>

## Description:

The platinum thin film RTD sensing element is exposed to air flow while being protected from passing debris by a vented housing (available in both plastic and steel). This construction uses a #26 AWG stranded nickel-plated copper, PFA insulated lead wire. This design comes standard with a removable miniature three pin connector. Used for the monitoring of air and gas streams, it mounts in any orientation. Model 805-B has the sensing element installed in a stainless steel housing, 806-B uses a plastic housing. Both are designed for direct contact with air and gas.

Figure B.7 Submersible Thermistor

# Air Circulation Fan



## Technical Specifications

Dimensions	50 x 50 x 20 mm
Connector	2-wire with 2-pin XH2.54-Pin
Rated Voltage	DC:12V
Rated Current	0.16 Amp
Rated Speed	6000 RPM
Air flow	17.5 CFM
Noise	26 dBA
Bearing Type	Sleeve
Life	38000 hours
Cable Length	20cm (7.8 in)
Weight	1.3oz

Recommended Brand	Cooler Master
Model	B0789QL579
Quantity Needed	1
Quantity at ESTA	0
Quantity to Purchase	1
Unit Cost	\$5.99
<b>Total Cost</b>	<b>\$5.99</b>

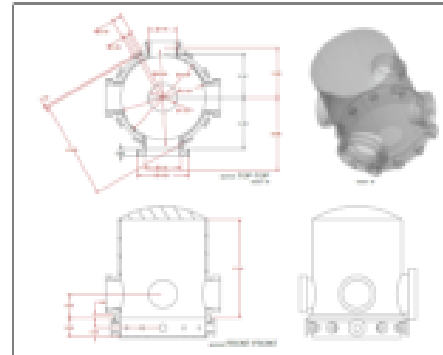
[https://www.amazon.com/Cooler-Master-2-Inch-Brushless-Cooling/dp/B0789QL579/ref=pd\\_gw\\_147\\_5/135-1759429-1167066?encoding=UTF8&pd\\_rd\\_i=B0789QL579&pd\\_rd\\_r=9b1ee84e-35fe-11e9-8361-31a05a5f3960&pd\\_rd\\_w=k3W7q&pd\\_rd\\_wq=NH7Y0&pf\\_rd\\_p=ad07871c-ef46-4161-82c7-5ed0d4c85b07&pf\\_rd\\_r=G35W0G1VZAJ3H2N84HAK&psc=1&refRID=G35W0G1VZAJ3H2N84HAK](https://www.amazon.com/Cooler-Master-2-Inch-Brushless-Cooling/dp/B0789QL579/ref=pd_gw_147_5/135-1759429-1167066?encoding=UTF8&pd_rd_i=B0789QL579&pd_rd_r=9b1ee84e-35fe-11e9-8361-31a05a5f3960&pd_rd_w=k3W7q&pd_rd_wq=NH7Y0&pf_rd_p=ad07871c-ef46-4161-82c7-5ed0d4c85b07&pf_rd_r=G35W0G1VZAJ3H2N84HAK&psc=1&refRID=G35W0G1VZAJ3H2N84HAK)

**Description:** Used for active cooling. Fans are used to draw cooler air into the case from the outside, expel warm air from inside and move air across a heat sink to cool a particular component.

Figure B.8. Air Circulation Fan



## Portable Bell Jar System 996



### Technical Specifications

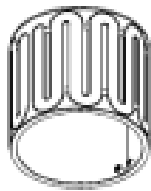
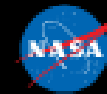
**Height** 27.0 in  
**Diameter** 27.0 in  
**Viewing/Entry Ports** 2 @ 7.75 in Diameter; 2 @ 9.75 in Diameter, centered 6.5 in from the base

Quantity Needed	1
Quantity at ESTA	1
Quantity to Purchase	0
Unit Cost	N/A
<b>Total Cost</b>	<b>N/A</b>

**Description:** This system is used to test small components or procedures that need to be performed or operated in a controlled environment. It can be pumped down to almost complete vacuum or held at a specific pressure and can maintain temperatures down to -40 °C (TBD). There are four viewing/entry ports and other pressure controlled ports for connecting wiring, water, atmospheric gases, etc. This facility is maintained and operated through the Energy Systems Test Area (ESTA) of the Propulsion and Power Division at JSC (EP4).

Figure B.9. Portable Bell Jar System 996

# Temperature Control Shroud



## Technical Specifications

Height	20.0 in
Diameter	22.0 in (OD)
Fittings	1/2 FNPT (2x), located $\pm 7^{\circ}$ from centerline
Water Pressure	$\leq 40$ psig

Quantity Needed	1
Quantity at ESTA	1
Quantity to Purchase	0
Unit Cost	N/A
Total Cost	N/A

**Description:** This shroud is water-controlled and used inside the 27" Portable Bell Jar System to maintain a controlled temperature. This component is maintained and operated through the Energy Systems Test Area (ESTA) of the Propulsion and Power Division at JSC (EP4).

Figure B.10. Temperature Control Shroud

# Laboratory Support Stand



## Technical Specifications

Product Dimensions	21 x 6 x 1 in
Weight	2.5 lbs
Base Length	8 in
Base Width	5 in
Rod Length	20 in
Rod Diameter	3/8 in

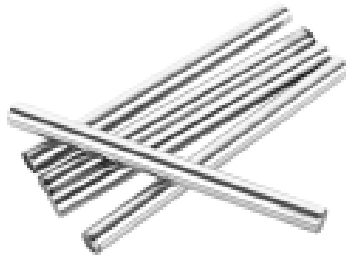
Recommended Brand	American Educational Products
Model	7-G67
Quantity Needed	1
Quantity at ESTA	0
Quantity to Purchase	1
Unit Cost	\$14.26
<b>Total Cost</b>	<b>\$14.26</b>

[https://www.amazon.com/American-Educational-Stamped-Support-Resistant/dp/B00657N7T5/ref=sim\\_328\\_32?encoding=UTF8&pd\\_rd\\_i=B00657N7T5&pd\\_rd\\_r=ad3aa039-0486-11e9-b54d-a3f4d08ced8f8&pd\\_rd\\_w=2G4r3&pd\\_rd\\_wg=1lyO6&pf\\_rd\\_p=18bb0b78-4200-49b9-ac91-f141d61a1780&](https://www.amazon.com/American-Educational-Stamped-Support-Resistant/dp/B00657N7T5/ref=sim_328_32?encoding=UTF8&pd_rd_i=B00657N7T5&pd_rd_r=ad3aa039-0486-11e9-b54d-a3f4d08ced8f8&pd_rd_w=2G4r3&pd_rd_wg=1lyO6&pf_rd_p=18bb0b78-4200-49b9-ac91-f141d61a1780&)

**Description:** Strong and dependable support. Available in stamped steel. Type 15 coated with an acid resistant finish. The rods are nickel plated steel and are threaded to fit the base. Base size: 8 in. length by 5 in. width, rod size: 3/8 in. diameter by 20 in. length.

Figure B.11. Laboratory Support Stand

## Support Stand Steel Rods



### Technical Specifications

Size	8 X 100 mm (0.31 x 4 in), D*L
Material	Steel
Hardness	HRC60
Weight	195 g
Package Content	5 Pcs

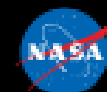
Recommended Brand	Eowpower
Model	02-001-001
Quantity Needed	1
Quantity at ESTA	0
Quantity to Purchase	1
Unit Cost	\$9.49
<b>Total Cost</b>	<b>\$9.49</b>

[https://www.amazon.com/dp/B01NCOMFLT/ref=sspa\\_dk\\_detail\\_1?psc=1&od\\_rd\\_i=B01NCOMFLT#feature-bullets-btf](https://www.amazon.com/dp/B01NCOMFLT/ref=sspa_dk_detail_1?psc=1&od_rd_i=B01NCOMFLT#feature-bullets-btf)

**Description:** Rods are 8 mm X 100 mm in length, chrome plated for corrosion resistance, and are case hardened. Package contains 5 rods.

Figure B.12. Support Stand Steel Rods

# Lab Clamp Holders



## Technical Specifications

Material	Cast Iron
Diameter This Holder Can Hold	0-16mm
Length	150mm
Weight	200 g
Package Content	4 pieces

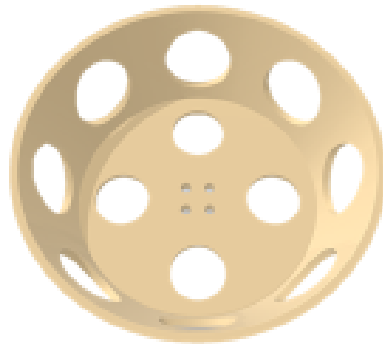
Recommended Brand	MALAB
Model	MALAB816-2-3
Quantity Needed	2 pkg (8 pieces)
Quantity at ESTA	0
Quantity to Purchase	2 pkg (8 pieces)
Unit Cost	\$13.99
<b>Total Cost</b>	<b>\$27.98</b>

[https://www.amazon.com/MALAB-Clamp-Holder-Heads-Retort/dp/B074TWMN43/ref=pd\\_slim\\_328\\_467\\_encoding=UTF8&pd\\_rd\\_i=B074TWMN43&pd\\_rd\\_r=ad3aa039-0486-11e9-b54d-a3f4d08ced8f&pd\\_rd\\_w=2G4zS&pd\\_rd\\_wg=11yO6&pf\\_rd\\_p=18bb0b78-4200-49b9-ac91-f141d61a1780&pf\\_rd\\_r=4VNYCT7](https://www.amazon.com/MALAB-Clamp-Holder-Heads-Retort/dp/B074TWMN43/ref=pd_slim_328_467_encoding=UTF8&pd_rd_i=B074TWMN43&pd_rd_r=ad3aa039-0486-11e9-b54d-a3f4d08ced8f&pd_rd_w=2G4zS&pd_rd_wg=11yO6&pf_rd_p=18bb0b78-4200-49b9-ac91-f141d61a1780&pf_rd_r=4VNYCT7)

**Description:** Use to Hold a Clamp on Retort Stand in Labs. High Quality; Strong; Cast Iron and Iron Screw Thread. Can Hold Diameter 0-16 mm. Blue and Black, Spray Finishing; 4 Pcs Each Set.

Figure B.13. Lab Clamp Holders

## 3D Printed “Bowl”



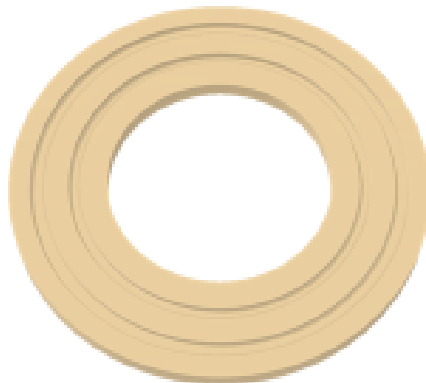
Technical Specifications	
Material	Ultem
Width	7.5 cm
Height	7.499 cm
Depth	2.475 cm

Quantity Needed	1
Quantity at ESTA	0
Quantity Manufactured	1
Unit Cost	N/A
Total Cost	N/A

**Description:** Made of Ultem and printed as a porous object, this “bowl” was designed using CREO 3.0 Computer-Aided Design (CAD) software and converted to .stl format, then printed in-house using a 3D printer. It supported the dewar and provided a neutral space for all the required electronic parts to attach to the dewar without interference with the load cell.

Figure B.14. 3D Printed “Bowl”

## 3D Printed “Support Ring”



### Technical Specifications

Material	Ultem
Width	7.5 cm
Height	7.499 cm
Depth	0.35 cm

Quantity Needed	1
Quantity at ESTA	0
Quantity Manufactured	1
Unit Cost	N/A
Total Cost	N/A

**Description:** Made of Ultem and printed as a porous object, this “support ring” was designed using CREO 3.0 Computer-Aided Design (CAD) software and converted to .stl format, then printed in-house using a 3D printer. It sat on top of the “bowl,” providing a stable support for the dewar.

Figure B.15. 3D Printed “Support Ring”



## 3D Printed “Base”



### Technical Specifications

Material	Ultem
Width	8.832 cm
Height	1.5 cm
Depth	1 cm

Quantity Needed	1
Quantity at ESTA	0
Quantity Manufactured	1
Unit Cost	N/A
Total Cost	N/A

**Description:** Made of Ultem and printed as a porous object, this “base” was designed using CREO 3.0 Computer-Aided Design (CAD) software and converted to .stl format, then printed in-house using a 3D printer. It provided a stable base for the load cell and the “bowl” that held the dewar.

Figure B.16. 3D Printed “Base”

## Resistance Temperature Detectors (RTDs)



Technical Specifications	
Sensor Application	Air Probe
Accuracy	Class A per IEC60751
Nominal Resistance	100 $\Omega$ , Class "A" DIN Platinum Element
Temperature Range	-50 to 230°C (-60 to 445°F)
Number of Wires	3
Sheath Material	304 Stainless Steel
Probe Diameter	0.500 in
Probe Length	1.25 in
Cable Insulation	PFA
Wire Gauge	26 AWG
Cable Length	40 in
Termination	3-Prong Miniature
Connection Type	Connector

Recommended Brand	Omega
Model	RTD-805-B, RTD-806-B
Quantity Needed	4(?)
Quantity at ESTA	4(?)
Quantity to Purchase	0
Unit Cost	N/A
Total Cost	N/A

<https://www.omega.com/en-us/sensors-and-sensing-equipment/temperature/sensors/thermocouple-probes/rtd-805-rtd-806/p/RTD-805>

**Description:** Air Temperature RTD sensors have a platinum thin film RTD sensing element that is exposed to air flow while being protected from passing debris by a vented stainless steel housing (RTD-805-B) or a plastic housing (RTD-806-B). This construction uses a #26 AWG stranded nickel-plated copper, PFA insulated lead wire and comes standard with a removable miniature three pin connector.

Figure B.17. Resistance Temperature Detectors (RTDs)

# Recirculating Chiller



## Technical Specifications

Cooling Capacity	$\leq 1.2$ kW
Heating Capacity	$\leq 3.4$ kW
Voltage	230 V / 50 Hz
Working Temperature Range	-80 °C ... 200 °C
Temperature Stability	$\pm 0.01$ °C ... $\pm 0.05$ °C
Ambient Temperature	+5 °C ... +40 °C
Pump Capacity Flow Rate	15 ... 38 l/min
Pump Capacity Flow Pressure	4.4 ... 18.9 psi

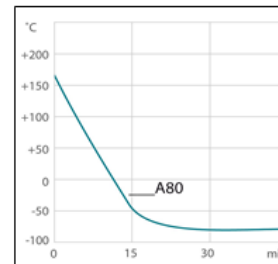
Recommended Brand	Julabo
Model	A80
Quantity Needed	1
Quantity at ESTA	1
Quantity to Purchase	0
Unit Cost	N/A
<b>Total Cost</b>	<b>N/A</b>

<https://www.julabo.com/en-us/products/highly-dynamic-temperature-control-systems/presto-process-systems/presto-a80>

**Description:** The A80 chiller has a two-stage refrigeration system. It offers rapid heating and cooling using one thermal fluid, with a temperature range down to -80 °C. It is electronically adjustable in stages or by setting a pressure value. Additionally, the A80 has the following safety features:

- Fully automated degassing procedure
- Reproducible test results
- Maximum uptime
- Electronically adjustable pumps (in stages or by setting the pressure value)

## Cool-Down Time



## Heat-Up Time

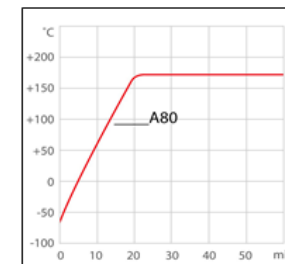


Figure B.18. Recirculating Chiller

## APPENDIX C

### FORTRAN CODE WITH COMMENTS AND DEFINITIONS/EXPLANATIONS OF TERMS

As described in the “Potable Water Supply Feasibility Study for Summit Station, Greenland,” the FORTRAN code shown below was originally written by the Cold Regions Research and Engineering Laboratory (CRREL) for water well design at the Antarctic base and was modified for use at Summit, Greenland [35]. Following the original code, a table is provided that describes the modifications made for simulations of water retrieval from a glacier on the Martian surface.

```
1      program main
2
3      c Original program written for
4      c   Lunardini, V. J. and J. Rand (1995) Thermal Design of an Antarctic Water
5      c   Well, CRREL Special Report 95-10, Cold Regions Research and Engineering
6      c   Laboratory, Hanover, NH.
7      IMPLICIT DOUBLE PRECISION (A-H,K-M,O-Z)
8      character PRNTR*12
9      integer i,j,n
10     integer jj
11     read(*,*) PRNTR
12     OPEN(9,FILE=PRNTR,STATUS='unknown')
13     c
14     c Modified to run for Summit, Greenland
15
16     CCC FORMATION DELT = TZ3
17     read(*,*) TZ3 ! hrs
18     read(*,*) MG0 ! gallons, initialized bulb volume
19     read(*,*) QBC
20     read(*,*) MF !lbm/hr, Boiler mass flow rate
21     CCC PHASE 1 1ST SUMMER DELT = TZ4+24
22     read(*,*) TZ4 !hrs
23     read(*,*) QBC1 ! btu/hr
24     read(*,*) MUG1 ! gal/day, initial withdrawal
25     read(*,*) MF1 ! lbm/hr, boiler mass flow rate
26     TZ3E = 88000.0 ! ten years
27     CCC PHASE 2 1ST SUMMER DELT = TZ5
```

```

28      read(*,*) TZ5 ! hrs
29      MUG2 = MUG1 ! gal/day
30      read(*,*) QBC2
31      read(*,*) MF2
32      CCC PHASE 3 1ST WINTER DELT = TZ6
33      read(*,*) TZ6
34      read(*,*) QBC3
35      CCC 2ND & SUB SUMMERS
36      read(*,*) QBC4
37      CCC 2ND & SUB WINTERS
38      read(*,*) QBC5
39
40      AL = 0.30 ! Firn loss parameter
41      ALPHAI = .0446 ! ft2/hr
42      BO = 1.1
43      CPA = .24 ! BTU /lb-F, Cp air
44      CPI = .5 ! Cp ice
45      CPW = 1.0 ! Cp water
46      read(*,*) DEPTH ! ft, initial depth to top of water
47      DT = 8.333001E-03 ! hrs (30 secs)
48      EIT = 0.0
49      E = 0.0
50      FI = 0.90
51      GAM = 1.0
52      H = 10.0
53      HA = 1.0
54      HB = 60.0
55      HI = 1.0
56      HS = 32.5 ! BTU/hr-ft2-F
57      HBN = 24.0
58      HSN = 32.5
59      HSO = 32.5
60      J = 1
61      KI = 1.28 !BTU/hr-ft-F, ice/firn conductivity
62      MU = 0.0
63      MUD = 7549.5
64      MWG = 0.0 ! gallons, bulb water volume in gallons

```

```

65      read(*,*) MFS ! summer boiler flow rate. lbm/hr
66      read(*,*) MFW ! winter flow rate
67      read(*,*) MUGS ! summer withdrawal, gal/day
68      read(*,*) MUGW ! winter withdrawal, gal/day
69      MGW = 1106533.0 !
70      N = 1
71      OMEGA = 5.399
72      PI = 3.141593
73      PL = 0.0
74      PM = 0.0
75      PLT = 0.0
76      PMT = 0.0
77      PRWT = 0.0
78      QS = 0.0
79      QT = 0.0
80      QTT = 0.0
81      QIT = 0.0
82      RA = 1.5 !ft, drill radius
83      RHOIS = 45.0 !lbm/ft3, start close-off density of firn
84      RHOIM = 57.54 !lbm/ft3, max firn density
85      RHOW = 62.6 ! lbm/ft3, water density
86      RO = RA ! ft
87      CCC TIME PARAMETERS
88      TAUP = 0.0
89      TI = 0.0
90      TIS = 0.0
91      TP = 24.0
92      TPI = 24.0
93      TPIW = 24.0
94      TZ1 = 8760.0 ! 8760 days is one year
95      TZ2 = 8760.0
96      TZS = TZ1 - TZ6 ! Summer duration (days)
97      CCC TEMPERATURES
98      TF = 32.0
99      read(*,*) TICE ! F, Firn Temperature
100     read(*,*) TWB ! F, Boiler water temperature
101     TA = TICE

```

```

102     TS = TICE  TW = TWB
103     ccc
104     ! depth at which shut-off starts in firn.
105     ZS = ((RHOIS - 20.18)/2.4996)**(1/0.45) ! Greenland data
106
107     D = 2.82843*RO !ft, diameter of bulb
108     MFA = MF
109     MW = PI * RA * RA * H * RHOW !lbm, water mass
110     MWO = MW
111     HWB = DEPTH + H !ft, depth to well bottom
112     MWGA = MW / (.134 * RHOW) ! gallons, convert bulb water mass to volume in gallons
113     LE = 144.0 + CPI * (TF - TICE) * OMEGA
114     AB = PI * D**2./4.0 ! ft2, air-water interface area
115     HW = H ! ft, water depth
116     AS = 2.0*PI*D*H/3.0 ! ft2, water-ice contact area
117     VW = PI*D**2.*H/8.0 ! ft3, water volume in bulb
118     AI = 2.0 * PI * RA * DEPTH ! ft2, air-ice contact area
119     VA = PI * RA * RA * DEPTH ! ft3, air volume
120
121     130  Write(9,3000)
122     3000 format(1x,'ANTARCTIC PARABOLIC ICE RESEVOIR FORMATION ')
123     140  Write(9,3001) TWB
124     3001 format(1x,' BOILER WATER TEMP DEG F = ',F9.2)
125     150  Write(9,3002) MF
126     3002 format(1x,' BOILER WATER FLOW RATE lbm/hr = ',F9.2)
127     160  Write(9,3003) HS
128     3003 format(1x,' CONVECTIVE COEFFICIENT BTU/HR-FT2-F = ',F9.2)
129         Write(9,3013) RA
130     3013 format(1x,' INITIAL DRILL RADIUS FT = ',F9.2)
131         Write(9,3014) DEPTH
132     3014 format(1x,' DEPTH TO TOP OF WATER AT START FT = ',F9.2)
133     180  Write(9,3005) D
134     3005 format(1x,' INITIAL PARABOLIC WATER DIAMETER D FT = ',F9.2)
135     191  Write(9,3007) HW
136     3007 format(1x,' INITIAL PARABOLIC WATER HEIGHT HW FT = ',F9.2)
137     200  Write(9,3008) TW

```



```

138      3008 format(1x,'INITIAL WATER TEMP TW DEG F = ',F9.2)
139      201  Write(9,3009) TA
140      3009 format(1x,' INITIAL AIR TEMP TA DEG F = ',F9.2)
141      202  Write(9,3010) TS
142      3010 format(1x,' INITIAL ICE SURFACE TEMP TS DEG F = ',F9.2)
143      210  Write(9,3011) TICE
144      3011 format(1x,'AMBIENT ICE TEMP DEG F = ',F9.2)
145      220  Write(9,3012) LE
146      3012 format(1x,'EFFECTIVE LATENT HEAT BTU/LB = ',F9.2)
147      221  Write(9,*) 'TIME IN HRS, WATER VOL MW GALLONS, ICE AREA AI FT2,
148      &  AIR VOL VA FT3 '
149      222  Write(9,*)
150      252  Write(9,*) TIME      TW      TA      TS      MW      D      HW      HWB
151      &  AI .....VA'
152      253  Write(9,2001) TI, TW, TA, TS, MWGA, D, HW, HWB, AI, VA
153      3030 format(1x,F8.2, 3F7.2,F9.2,2F6.2,F7.2,2F7.2)
154
155      260  DO I=1,112500000
156      IF (MWG .GT. MGO) GOTO 1220 ! bulb water volume .gt. initilaize volume
157
158      IF (TI .GT. TZ3) GOTO 1220 ! time .gt. formation period
159      IF (J .EQ. 1) GOTO 280 ! not sure why we branch here, bulb formation?
160
161      400  IF (TI .LT. TAUP) then ! not sure what taup is
162      MF = 0.0
163      MUG = MUGA MU = MUD
164      else
165      MF = MFA MUG = 0.0
166      MU = 0.0
167      end if
168
169      ! determine firn density
170      280  ZP = HWB-H/2.0 ! ft, average bulb depth
171      ! This is for Greenland data at Summit
172      RHOI = 20.18 + 2.4996 * ZP**0.45 ! shallow: ZP .le. 394 ft
173      IF(ZP .GT. 394) then
174      RHOI = RHOIM

```

```

175     end if
176
177     ! compute the change in water depth, h (eq. 7)
178     291 DELH = 16.0*H*(HS*(TW-TF)-QS)*DT/(RHOI*LE*3.0*(2.0*GAM*H+D)) HP =
179     H+DELH
180     DP = D+GAM*DELH HWBP = HWB+DELH
181     ! assumes full shut-off of water leakage into firn at ZS.
182     ZPS = HWB-ZS
183     ASP = 2.0*PI*D*H/3.0 ! all of surface area in fully porous firn
184
185     IF(ZPS .GT. H) then ! bulb below firn shut-off
186     ASP = 0.0 ! none of bulb surface area in fully porous firn shut-off
187     else IF(HWB .GT. ZS) then ! well bottom is deeper than firn shut-off
188     ZPP = (ZS+HWB-H)/2.0 ! average depth of portion of bulb in porous firn
189
190     ASP = 2.0*PI*D*H*(1.0-(ZPS/H)**1.5)/3.0 ! portion of bulb in porous firn
191     RHOI = 20.18 + 2.4996 * ZPP**0.45 ! firn density endif
192     283 MUL = AL*ASP*(RHOIS - RHOI) ! water mass lost to firn
193
194     IF(MF .EQ. 0.0) GOTO 284
195     TWB = QBC/(CPW*MF) + TW
196     284 TWP = TW+(MF*(TWB-TW)-HS*AS*(TW-TF)*(1.0/CPW+(TW-TF)/LE-QS/
197     & (LE*HS))-HA*AB*(TW-TA)/CPW)*DT/MW
198     MWP = MW+(((TW-TF)*HS-QS)*AS/LE-MU-MUL)*DT
199     MWG = MWP / (.134 * RHOW)
200     VWP = MWP / RHOW
201     HF = SQRT(8.0*VWP*HP/PI)/DP
202     DF = DP*SQRT(HF/HP)
203     HW = HF
204     EP = CPW * (TWB - TWP) * MF * DT
205     E = E + EP
206     PMP = MU*DT PM = PM + PMP
207     PLP = MUL*DT PL = PL + PLP
208     AIP = AI+PI*(DP**2-D**2)/4.0 + PI*DP*(HP-HF)
209     VAP = VA + PI*(DP**2*HP-DF**2*HF)/8.0
210     H = HF D = DF
211     TI = DT + TI

```

```

212      Q = HI * (TA - TS)
213      QI = Q * DT * AI
214      QT = QT + Q * DT
215      QIT = QIT + QI
216      QB = QT / TI
217      TAU = ALPHAI * TI / (RO ** 2)
218
219      RHOA = 39.685 / (TA + 460.0)
220      TAP = TA + (HA * AB * (TW - TA) + HI * AI * (TS - TA)) * DT / (RHOA * VA * CPA)
221
222      418  FB = 5.0 * BO ** 3.0 / 36.0 - BO / 4.0 + 1.0 / 9.0 + (1.0 / 3.0 - BO / 2.0) * LOG(BO) -
223      &    TAU * (BO - 1.0 + LOG(BO))
224      FBP = 5.0 * (BO ** 2) / 12.0 - .25 * LOG(BO) / 2.0 + (1.0 / 3.0 - BO / 2.0) / BO -
225      &    TAU * (1.0 + 1.0 / BO)
226
227      BP = BO - FB / FBP
228      BZ = ABS(BP - BO)
229      IF(BZ .lt. .0001) GOTO 425
230      BO = BP
231      GOTO 418
232      425  B = BP
233      BO = BP + .1
234      TS = TICE + QB * RO * (B - 1.0) * LOG(B) / (KI * (B - 1.0 + LOG(B)))
235      IF(J .EQ. 1) GOTO 1031
236      IF(TI .gt. TPW) GOTO 1130
237      1028 IF(TI .gt. TP) GOTO 1131
238      GOTO 560
239      1031 IF(TI .gt. TP) GOTO 1128
240      560  continue
241      HWB = HWBP
242      TW = TWP
243      TA = TAP
244      MW = MWP
245      AS = 2.0 * PI * D * H / 3.0
246      AB = PI * D ** 2 / 4.0
247      AI = AIP
248      VA = VAP

```

```

249      IF (D .GT. 60.0) GOTO 1010
250      HS = HSO
251      GOTO 1040
252      1010 HS = HSN
253      1040 IF(TW .LT. 32.0001) GOTO 1075
254      1041 IF(TI .GT. TZ2) GOTO 1220
255      IF(TI .GT. TZ1) GOTO 1220
256
257      1070 end do
258      GOTO 1760
259      1075 TW = 32.0
260      GOTO 1041
261      1128 Write(9,2001) TI, TWP, TAP, TS, MWG, D, HW, HWBP, AIP, VAP TP = TP + TPI
262      TPW = TP
263      GOTO 560
264      1130 Write(9,2001) TI, TWP, TAP, TS, MWG, D, HW, HWBP, AIP, VAP
265      2001 format(1x, F8.1, 3F7.2, F9.1, 2F6.2, F7.2, 2F11.2) TPW = TPW + TPIW
266      GOTO 1028
267      1131 TP = TP + TPI
268      TAUP = TP+MUGA*.134*RHOW/MUD-TPI
269      GOTO 560
270      1220 Write(9,2001) TI, TWP, TAP, TS, MWG, D, HW, HWBP, AIP, VAP
271      2000 format(1X,6F9.2)
272      1280 Write(9,*)
273      EI = E - EIT
274      ESR = EI/(TI-TIS) EIT = E
275
276      PRW = MW-MWO + PM
277      PRWT = PRWT+PRW
278      PLT = PLT+PL
279      PMT = PMT+PM
280      EKT = PRWT*19500.0/E
281      EK = PRW * 19500.0 / EI
282      PMG = PM/(.134*RHOW)
283      PM = 0.0
284      PLG = PL/(.134*RHOW)
285      PL = 0.0

```

```

286      MWO = MW
287      EF = E / 140000.0
288      EFI = EI / 140000.0
289      QITI = QIT - QTT
290      QTT = QIT
291      1340 Write(9,3040) E
292      3040 format(1x, '.....TOTAL ENERGY INPUT BTU =
293      ',E15.6)
294      Write(9,3041) EI
295      3041 format(1x, '..... SEASONAL ENERGY INPUT BTU =
296      ',E15.6)
297
298      Write(9,3051) EFI
299      3051 format(1x, '.....SEASONAL ENERGY INPUT GAL FUEL =
300      ',F15.2)
301      Write(9,3042) ESR
302      3042 format(1x, '..... SEASONAL ENERGY RATE BTU/HR =
303      ',F15.2)
304      1370 Write(9,3050) EF
305      3050 format(1x, '.....TOTAL ENERGY INPUT GAL FUEL =
306      ',F15.2)
307      Write(9,3063) EKT
308      3063 format(1x, '..... AVERAGE LB. WATER PER LB. FUEL =
309      ',F15.2)
310      1400 Write(9,3060) EK
311      3060 format(1x, '..... SEASONAL LB. WATER PER LB. FUEL =
312      ',F15.2)
313      1401 Write(9,3070) QIT
314      3070 format(1x, '.....ENERGY FROM AIR TO ICE BTU =
315      ',E15.6)
316      Write(9,3071) QITI
317      3071 format(1x, '.....SEASONAL ENERGY LOSS, AIR TO ICE BTU = ',E15.6)
318      Write(9,3064) PMT/(.134*RHOW)
319      3064 format(1x, '.....TOTAL WATER WITHDRAWN GAL =
320      ',F15.2)
321      Write(9,3061) PMG
322      3061 format(1x, '..... SEASONAL WATER WITHDRAWN GAL =
323      ',F15.2)
324      Write(9,3065) PLT/(.134*RHOW)
325      3065 format(1x, '..... TOTAL WATER LOSS GAL =
326      ',F15.2)

```

```

327      Write(9,3062) PLG
328      3062 format(1x, '.....SEASONAL WATER LOSS GAL =
329      ',F15.2)
330      1430 Write(9,*)
331
332      CCC **** END OF YEAR 1 ****
333      IF(N .EQ. 4) GOTO 1520
334      IF(N .EQ. 5) GOTO 1500
335      CCC **** END OF YEAR 2 ****
336      IF(N .EQ. 6) GOTO 1520
337      IF(N .EQ. 7) GOTO 1500
338      CCC **** END OF YEAR 3 ****
339      IF(N .EQ. 8) GOTO 1520
340      IF(N .EQ. 9) GOTO 1500
341      CCC **** END OF YEAR 4 ****
342      IF(N .EQ. 10) GOTO 1520
343      IF(N .EQ. 11) GOTO 1500
344      CCC **** END OF YEAR 5 ****
345      IF(N .EQ. 12) GOTO 1520
346      IF(N .EQ. 13) GOTO 1500
347      CCC **** END OF YEAR 6 ****
348      IF(N .EQ. 14) GOTO 1520
349      IF(N .EQ. 15) GOTO 1500
350      CCC **** END OF YEAR 7 ****
351      IF(N .EQ. 16) GOTO 1520
352      IF(N .EQ. 17) GOTO 1500
353      CCC **** END OF YEAR 8 ****
354      IF(N .EQ. 18) GOTO 1520
355      IF(N .EQ. 19) GOTO 1500
356      CCC **** END OF YEAR 9 ****
357      IF(N .EQ. 20) GOTO 1520
358      IF(N .EQ. 21) GOTO 1500
359      CCC **** END OF YEAR 10 ****
360      IF(N .EQ. 22) GOTO 1760
361      1490 MGO = MGW
362      MF = MF1
363      MUGA = MUG1

```

```

364      N = N + 1
365      J = J + 1
366      JJ = 1 ! year
367      MFA = MF
368      TIS = TI
369      TP = INT(TI/24.0)*24.0+TPI
370      TZ1 = TP+TZ4
371      TZ2 = TZ1+TZ5
372      TZ3 = TZ3E
373      QBC = QBC1
374      GOTO 1210
375      1500
376      MGO = MGW
377      MUGA = MUGW
378      MFA = MFS
379      N = N+1
380      MU = MUD
381      TZ2 = TZ1+TZS
382      TIS = TI
383      QBC = QBC5
384      GOTO 1553
385      1520
386      MGO = MGW
387      MUGA = MUGS
388      MFA = MFS
389      N = N+1
390      MU = MUD
391      JJ = JJ+1
392      TIS = TI
393      TZ1 = TZ2+TZ6
394      QBC = QBC4
395      GOTO 1551
396      1540MGO = MGW
397      MUGA = MUGW
398      MFA = MFS

```



```

399      N = N+1
400      JJ = 1
401      MU = MUD
402      TIS = TI
403      QBC = QBC3
404      TZ2 = TZ1+TZS
405      GOTO 1550
406      1204MGO = MGW
407      MF = MF2
408      MUGA = MUG2
409      N = N+1
410      JJ = 1
411      MFA = MF
412      MU = MUD
413      TIS = TI
414      TZ1 = TZ2+TZ6
415      QBC = QBC2
416      GOTO 1550
417      1210MU = MUD
418      TAUP = TP+MUGA*.134*RHOW/MUD-TPI
419      TPIW = 168.0
420      1550
421      8000 Write(9,8000) JJ
422      format(1x,' YEAR ',I3)
423      Write(9,6000)
424      6000 format(1x,'STANDBY OR WATER WITHDRAWAL ')
425      GOTO 1555
426      1551 Write(9,8000) JJ
427      Write(9,6001)
428      6001 format(1x,'SUMMER WATER WITHDRAWAL ')
429      GOTO 1555
430      1553 Write(9,8000) JJ
431      Write(9,6002)
432      6002 format(1x,' WINTER WATER WITHDRAWAL ')
433      1555 Write(9,*)
434      1580 Write(9,4010) MFA

```

```

435      4010 format(1x,'BOILER WATER FLOW RATE lbm/hr = ',F9.2)
436      Write(9,4011) TWB
437      4011 format(1x,'BOILER WATER TEMPERATURE DEG F = ',F9.2)
438      1610 Write(9,4020) MUGA
439      4020 format(1x,'WATER WITHDRAWAL GAL/DAY = ',F9.2)
440      Write(9,4021) MUD/(8.04*RHOW)
441      4021 format(1x,'WITHDRAWAL FLOW RATE GAL/MIN = ',F9.2)
442      1640 Write(9,4030) HS
443      4030 format(1x,'CONVECTIVE COEFF AFTER R=30 FT BTU/HR-FT2-F = ',F9.2)
444      1672 Write(9,5050) TI
445      5050 FORMAT(1X,'START WITHDRAWAL AT HOUR) = ',F9.2)
446      Write(9,*)
447      GOTO 400
448      1760 Write(9,*)
449      1790 Write(9,4050) E
450      4050 format(1x,'TOTAL ENERGY INPUT BTU = ', E15.6)
451      1820 Write(9,4060) E / 140000
452      4060 format(1x,'TOTAL ENERGY INPUT GAL FUEL = ',E15.2)
453      1821 Write(9,4070) QIT
454      4070 format(1x,'TOTAL ENERGY LOSS AIR TO ICE BTU = ', E15.6)
455      1850 END

```

Input Variables:	
TZ3	Bulb Initialization Duration (hrs)
MG0	Initial Bulb Water Volume (gallons)
QBC	Boiler Flow Rate (btu/hr)
MF	Initial Boiler Mass Flow Rate (lbm/hr)
TZ4	Initial Water Withdrawal Duration (hrs)
QBC1	Boiler Flow Rate (btu/hr)
MUG1	Initial Withdrawal Rate (gal/day)
MF1	Boiler Mass Flow Rate during Bulb Formation (lbm/hr)
TZ5	“Second Season” Duration (hrs)
QBC2	Boiler Flow Rate (btu/hr)
MF2	Initial Withdrawal Boiler Mass Flow Rate (lbm/hr)
TZ6	“Winter Season” Duration (hrs)
QBC3	Boiler Flow Rate (btu/hr)
QBC4	Boiler Flow Rate (btu/hr)
QBC5	Boiler Flow Rate (btu/hr)
DEPTH	Depth to Top of Water at Start (ft)
MFS	“Summer” Boiler Mass Flow Rate (lbm/hr)
MFW	“Winter” Boiler Mass Flow Rate (lbm/hr)
MUGS	Summer Withdrawal Rate (gal/day)
MUGW	Winter Withdrawal Rate (gal/day)
TICE	Ambient Ice Temperature (deg F)
TWB	Boiler Water Temperature (deg F)

Other Variables used in the code:	
TZ1, TZ2, TZS, TAUP	Year / "Season" duration parameters (hrs)
MUG2, MU, MUD, MUGA	Water Withdrawal Rates (MUG2 in gallons/day; MU, MUD, MUGA in gallons/minute)
AL	Firn Loss Parameter
ALPHAI	Thermal Diffusivity (ft <sup>2</sup> /hr)
BO	Temperature Disturbance Coefficient
CPA, CPI, CPW	C <sub>p</sub> Air, Ice and Water (BTU/lb-f)
DT	Delta Time (hrs)
EIT, E, EI, EFI, EF	Energy Inputs (BTU)
ESR	Seasonal Energy Rate (BTU/hr)
EK, EKT	Water Produced per Fuel Consumption
GAM	Rate of Change of Reservoir Diameter with Respect to Height
H	Initial Depth of Hole (ft)
HA, HI, HS, HSN, HSO	Convective Heat Transfer Coefficients for water/air, air/ice, water/ice (BTU/hr-ft <sup>2</sup> -F)
J, JJ	Year/Season Counters
KI	Ice-Firn Conductivity
MU, MUD, MUGA	Water Withdrawal Rates (gallons/minute)
MWG, MWGA, VW, MGW	Bulb Water Volume (MWG, MWGA in gallons; VW in ft <sup>3</sup> )
N	Counter (for program loops)
OMEGA	Penetration parameter

Other Variables (continued):	
PI	Pi (3.14159)
PL, PLT, PLG	Water Loss (gallons)
PM, PMT, PMG	Water Withdrawn (gallons)
PRW, PRWT	?
QS, QT, QTT, QIT, QITI	Energy Loss parameters (BTU)
RA	Drill Radius (ft)
RHOIS, RHOIM, RHOW	Firn Density Parameters (lbm/ft <sup>3</sup> )
RO	Hole Radius (ft)
TF, TA, TS, TW	Water, Air, and Ice Temperature parameters (deg F)
TI, TIS, TP, TPI, TPIW	Water Withdrawal duration parameters (hrs)
ZS	Depth at which Shut-Off Starts in Firn (ft)
D	Initial Parabolic Water Diameter (ft)
MFA	Actual Boiler Flow Rate (lbm/hr)
MW, MWO	Water Mass parameters (lbm)
HWB	Depth to Well Bottom (ft)
LE	Effective Latent Heat (BTU/lb)
AB	Air-Water Interface Area (ft <sup>2</sup> )
HW	Initial Parabolic Water Height (ft)
AS	Water-Ice Contact Area (ft <sup>2</sup> )
AI	Air-Ice Contact Area (ft <sup>2</sup> )
VA	Air Volume (ft <sup>3</sup> )
ZP	Firn Density

The following modifications were made to the code for it to be used for various design simulations of a glacial water well on the Martian surface:

Line Number	Modified Code	Reason for Modification
<b>8,11,12</b>	Character PRNTR * 20 PRNTR = "Output_Mars.dat" OPEN (unit = 10,FILE = PRNTR,STATUS = "NEW") OPEN (unit = 9,FILE = '\\f\\york\\data', STATUS = 'old')	Modified to output to a file named 'Output_Mars.dat' designated as Unit 10 and to read inputs from a file named 'data' stored in the 'c:\\f\\york' subdirectory and designated as Unit 9
<b>26</b>	TZ3 = 17500.0 <i>or</i> TZ3 = 2400.0 <i>etc.</i>	Denotes simulation end time; varied depending on length of time steps used in simulation
<b>43</b>	CPA = 0.199 ! BTU /lb-F,	Cp air of 0.24 BTU/lb-F changed to Mars value
<b>53</b>	HA = 0.458	Convective heat transfer coefficient for water/air modified for Mars atmosphere
<b>55</b>	HI = 0.725	Convective heat transfer coefficient for air/ice modified for Mars atmosphere
<b>63</b>	MUD = 0	Withdrawal rate in gallons/minute; varied per simulation (set to values equivalent to 0, 2, 5, 7.5, 10, 15, 20,25, 50, 100 gallons/day)
<b>218</b>	RHOA = 0.4758 / (TA + 460.0)	Original value of 39.685 was changed to 0.4758 to account for CO <sub>2</sub> atmosphere at low density
<b>91</b>	TP = 8.0 <i>or</i> TP = 12.0	Length of time step in hours; varied per simulation (8.0, 12.0, 24.0)
<b>92</b>	TPI = 8.0 <i>or</i> TPI = 12.0	
<b>93</b>	TPIW = 8.0 <i>or</i> TPIW = 12.0	

Line Number	Modified Code	Reason for Modification
105	ZS = H	Depth at which shut-off starts in firn; set equal to initial depth of hole
172 - 175	IF(ZP .GT. 520.0) GOTO 289 IF(ZP .GT. 320.0) GOTO 288 RHOI = 21.79 + 0.144 * ZP - .00017894 * ZP**2 GOTO 291 288 RHOI = .04 * ZP + 36.74 GOTO 291 289 RHOI = RHOM	Greenland firn density calculations replaced with those from Antarctic code
221 - 224	FB = 0 FBP = 0	Set to 0 in some runs to gauge FB and FBP significance in boiler flow rate calculations
345 - 347	IF (N .EQ. 22) GOTO 1520 IF (N .EQ. 23) GOTO 1500 IF (N .EQ. 24) GOTO 1520 IF (N .EQ. 25) GOTO 1500 <i>etc.</i>	More cycles through the calculations were added when time steps were reduced from 24 to 8 or 12 hours
356	TP = INT(TI / 8.0)*8.0 + TPI <i>or</i> TP = INT(TI / 12.0)*12.0 + TPI	Time calculations modified to match time steps used in simulation
368	TZ2 = TZ1 + 120.0	
380	TZ1 = TZ2 + 120.0	
391	TZ2 = TZ1 + 120.0	
406	TPIW = 24.0	

**APPENDIX D**  
**RAW OR PROCESSED DATA FROM BELL JAR EXPERIMENTS**

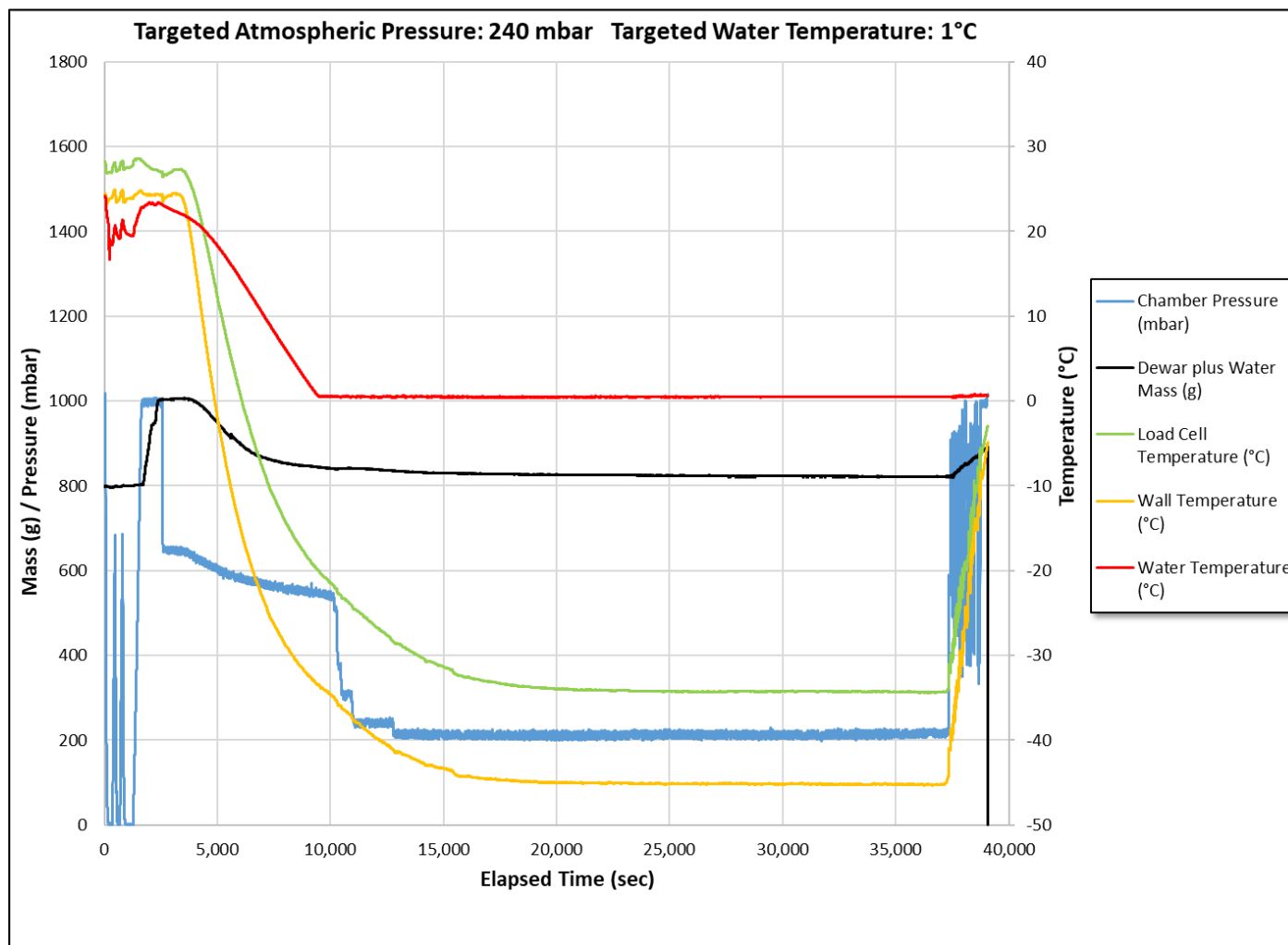


**Figure D.1. Test 5 – 9/30/2019**



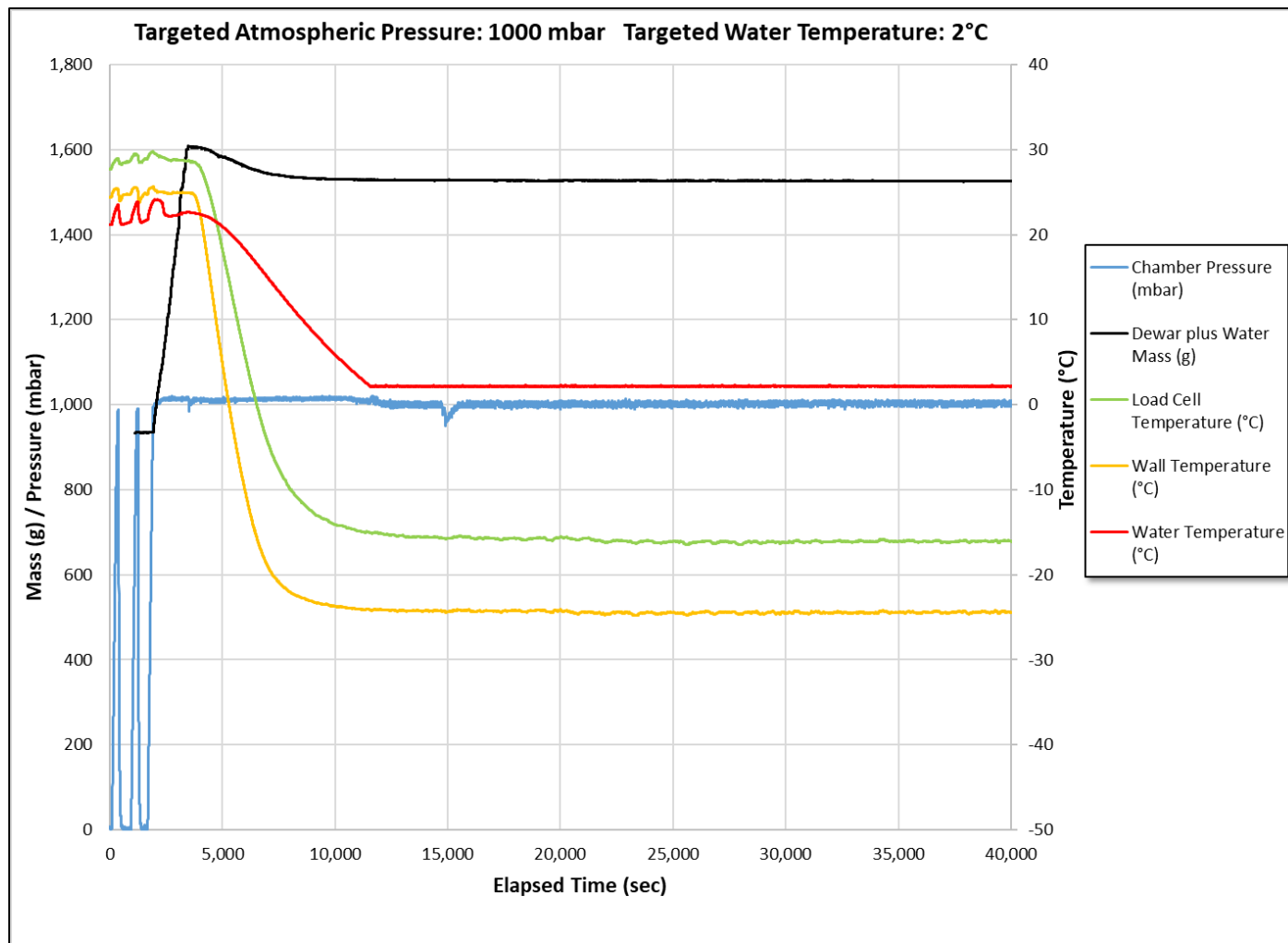


Figure D.2. Test 7 – 10/16/2019

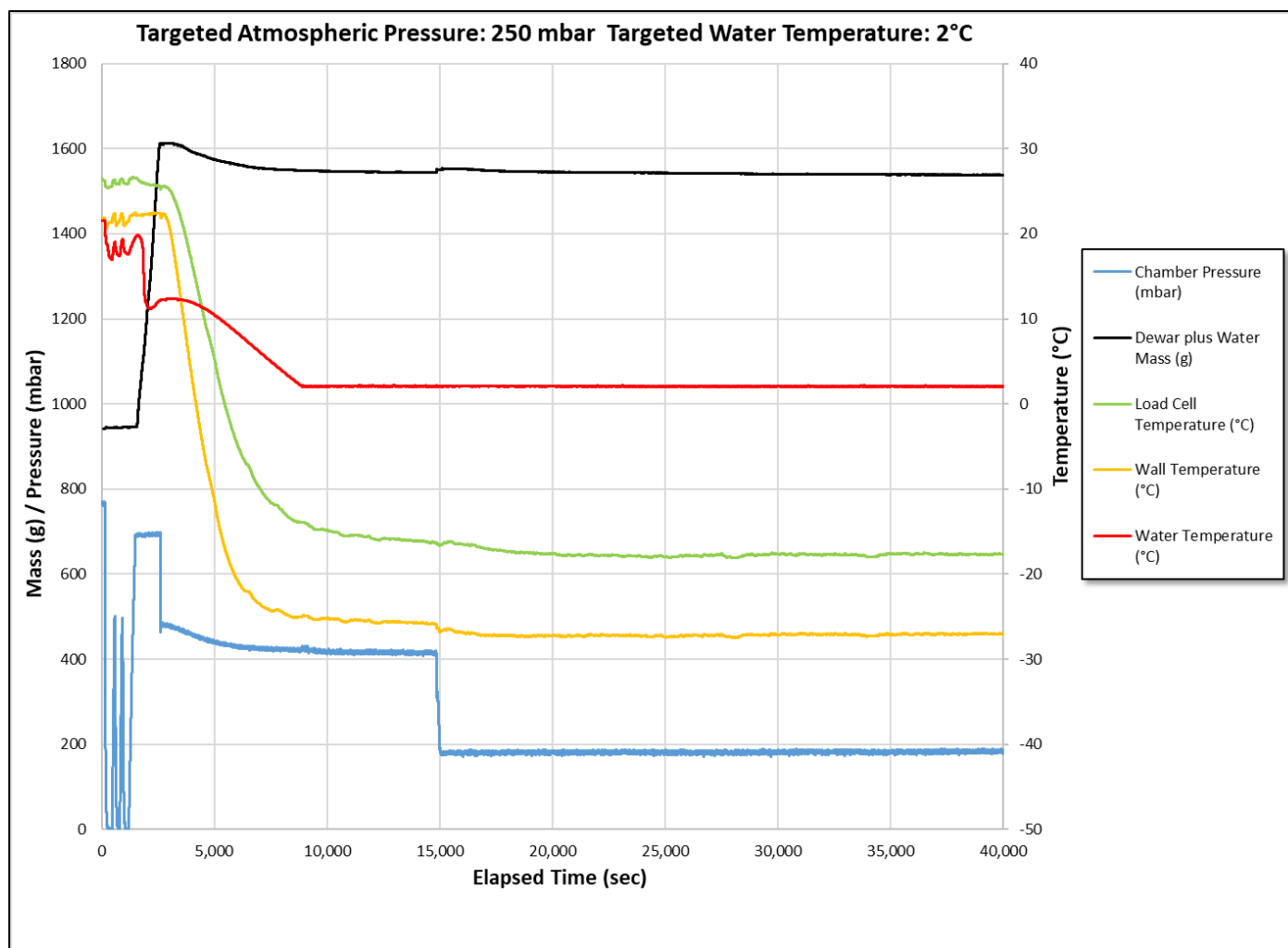


Figure D.3. Test 8 – 10/23/2019

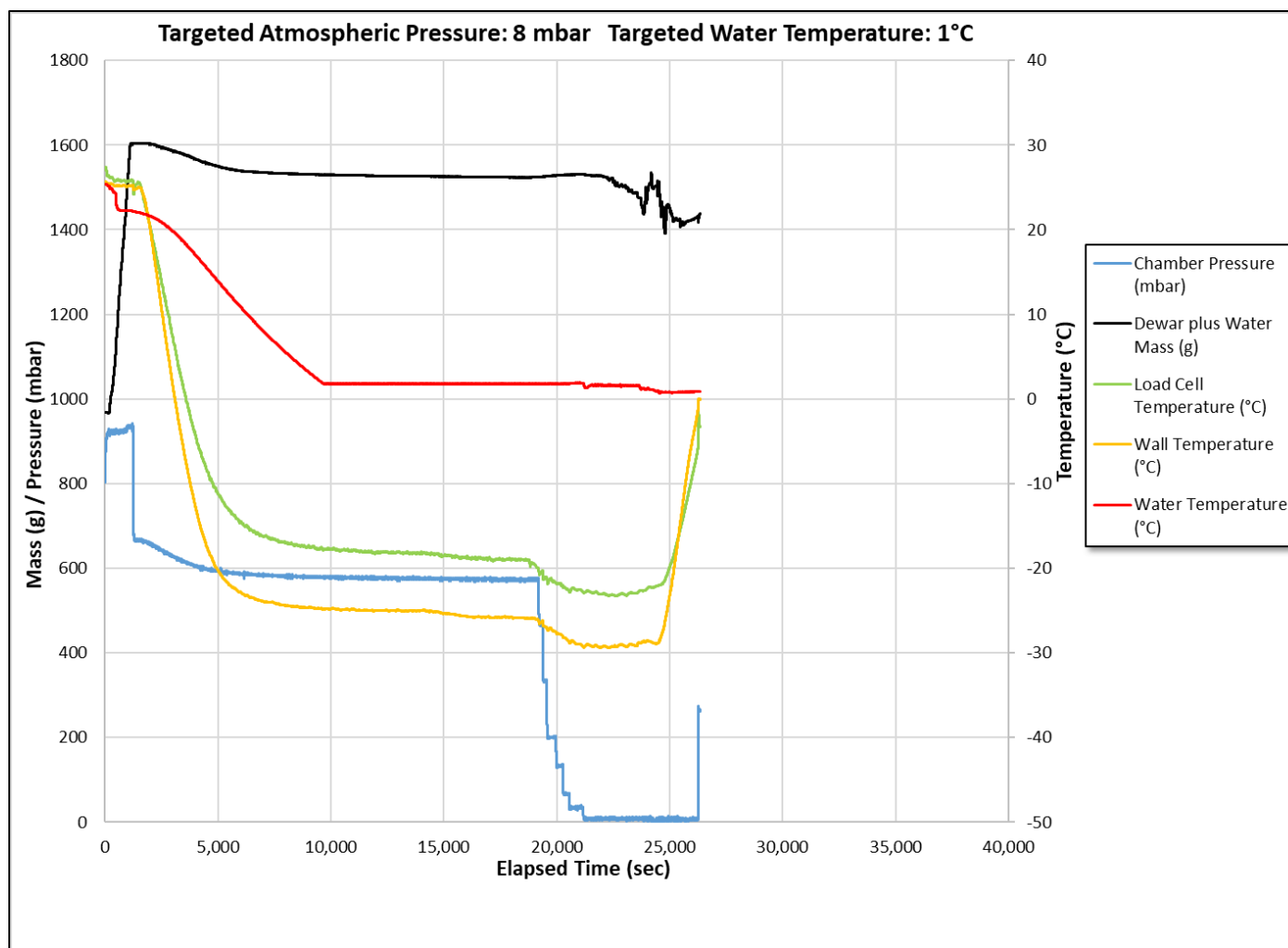


Figure D.4. Test 9 – 9/30/2019

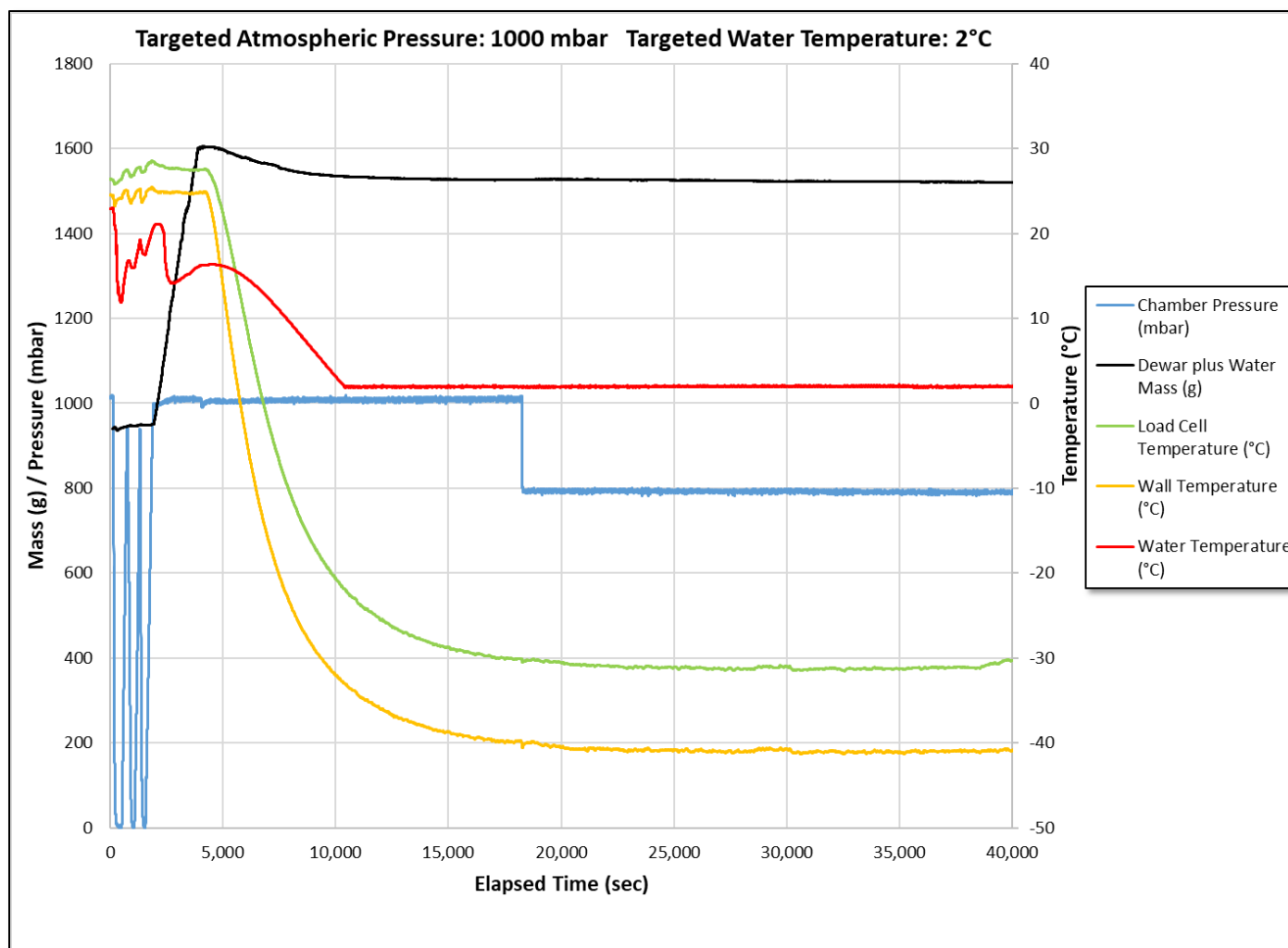


Figure D.5. Test 10 – 10/07/2019

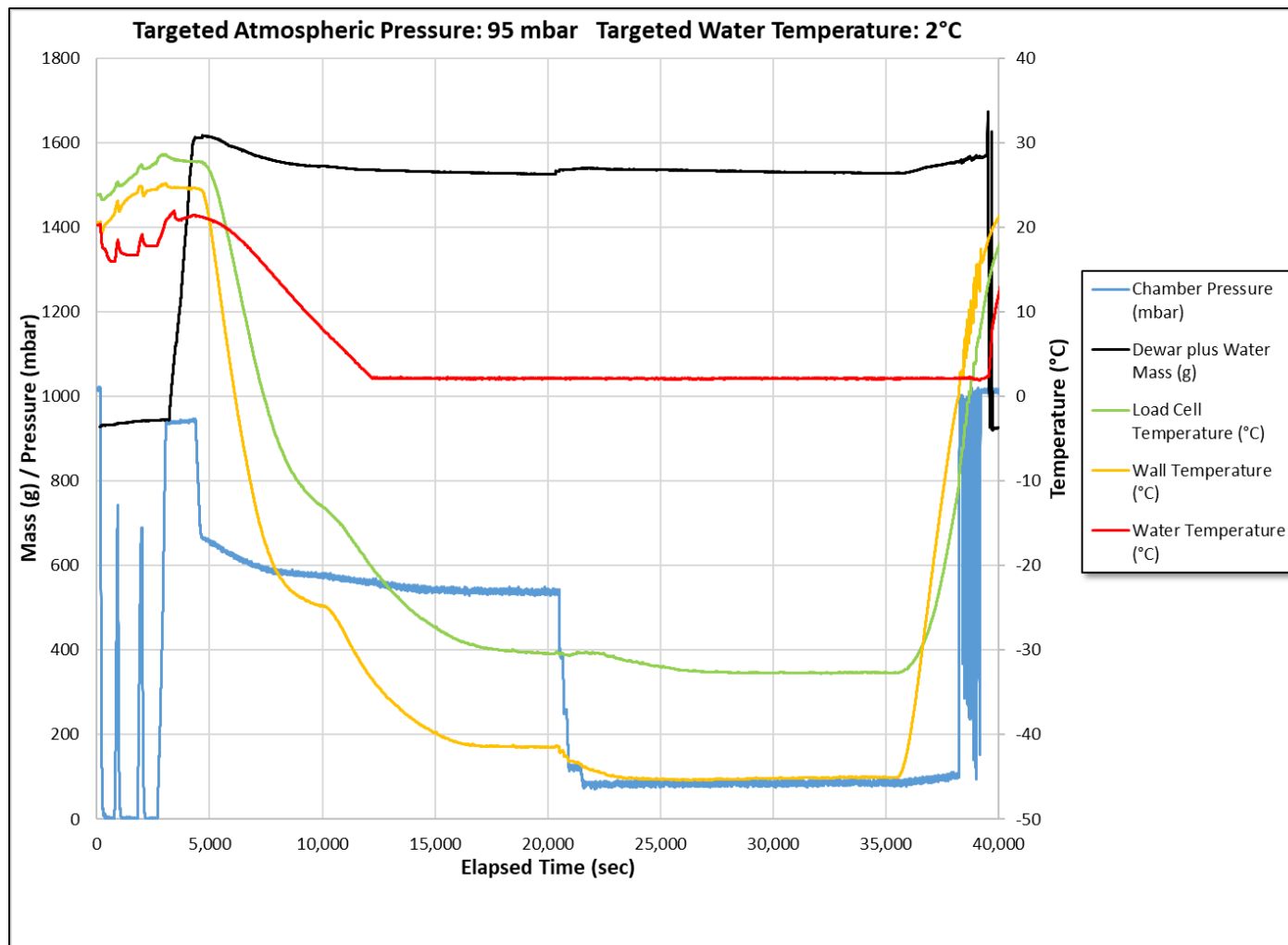


Figure D.6. Test 11 – 10/16/2019

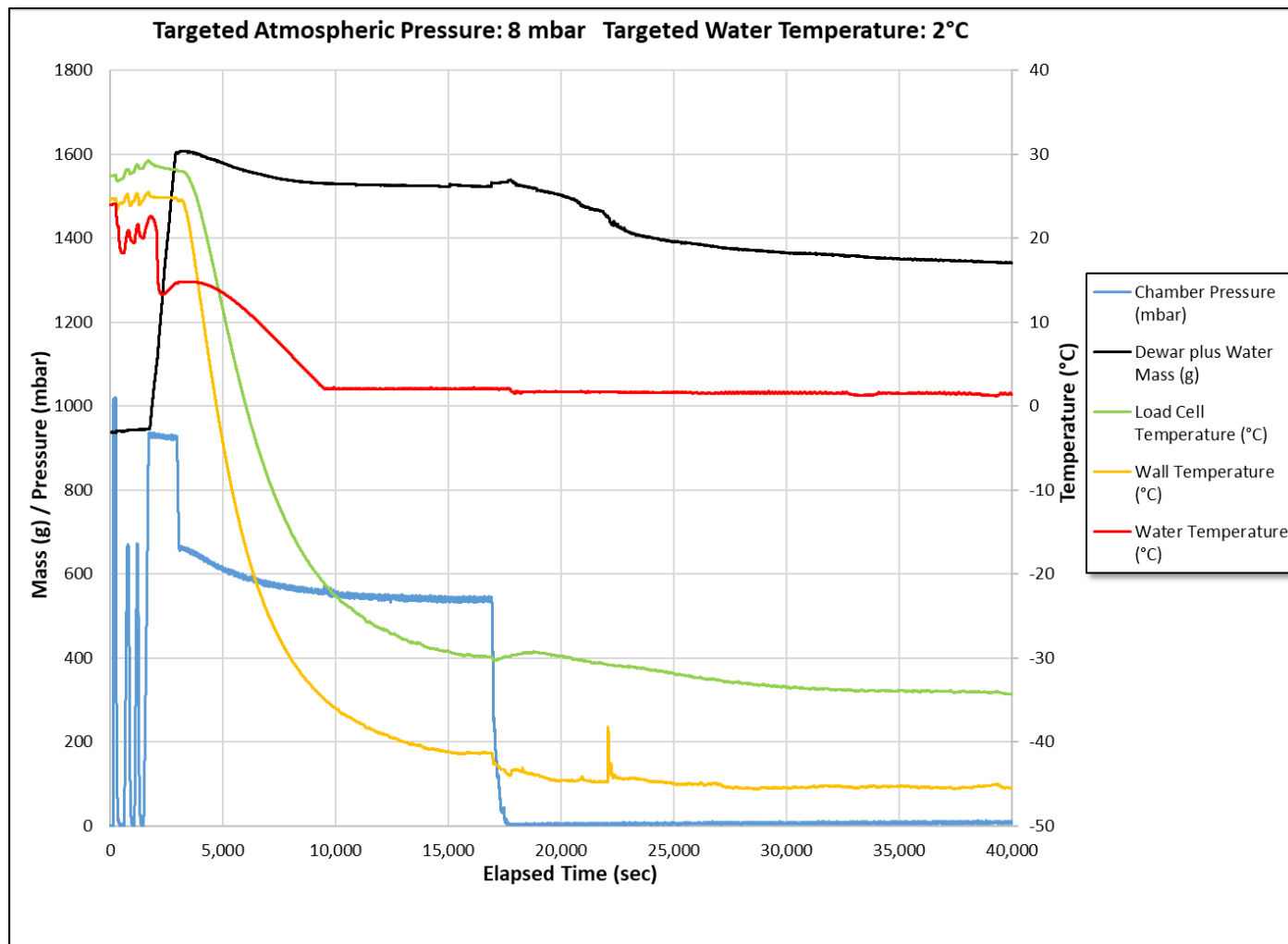


Figure D.7. Test 12 – 10/24/2019